Progress towards an ultracold atomic Sagnac gyroscope

by

Stephen Richard Segal

B.S., Pennsylvania State University, 2003

A thesis submitted to the
Faculty of the Graduate School of the
University of Colorado in partial fulfillment
of the requirements for the degree of
Doctor of Philosophy
Department of Physics
2010

This thesis entitled:
Progress towards an ultracold atomic Sagnac gyroscope
written by Stephen Richard Segal
has been approved for the Department of Physics

Dana Z. Anderson

Eric A. Cornell

Date

The final copy of this thesis has been examined by the signatories, and we find that both the content and the form meet acceptable presentation standards of scholarly work in the above mentioned discipline.

Segal, Stephen Richard (Ph.D., Physics)

Progress towards an ultracold atomic Sagnac gyroscope

Thesis directed by Professor Dana Z. Anderson

Precise, accurate inertial navigation relies upon the rotation rate measurements of a sensitive gyroscope. State of the art fiber optic gyroscopes measure rotation via the Sagnac effect, which causes a phase shift proportional to the angular velocity of a rotating interferometer whose beam path encloses an area. Gyroscopes using interfering atoms have a much greater Sagnac phase shift for the same enclosed area than optical gyroscopes, and therefore promise much greater sensitivity. However, an atom Sagnac gyroscope has not yet been demonstrated in a compact device.

This dissertation describes work towards the demonstration of a compact Sagnac gyroscope using interfering ultracold atoms, which can be guided around suitably large areas using magnetic potentials generated by micro-scale "atom chips". We first present the results of a sequence of preliminary Bose-Einstein condensate (BEC) Michelson interferometry experiments. In these experiments, BECs confined to a waveguide interfere, but the path does not enclose area. We present the application of statistical image analysis techniques to data from our experiments. We analyze the lessons learned about both apparatus design and the physics of BEC interferometry. We describe the design of a new atom chip that should allow us to translate the waveguide during the interferometry experiment, thus turning Michelson into Sagnac interferometry. Finally, we explain the design of a new compact BEC apparatus that incorporates the gyroscope chip. The apparatus is built on a rotary table so that we may truly test the gyroscope when it is complete. We report on experimental progress towards the achievement of BEC in this apparatus.

To Milton and Eleanor Segal

Acknowledgements

I owe a deep debt to the teachers and mentors who guided my development. Dana Anderson has been my advisor and boss for almost seven years. Besides supervising my education, he has taught me the value of clear communication skills and helped to show me how extremely hard work can result in progress (even if it is not obvious progress). I am thankful for his patience with me in my long maturation process. Two other mentors, Eric Cornell and Alex Zozulya (of Worcester Polytechnic Institute), also contributed much to my education and to the work presented here. In particular, I would have been lost without Alex's notes and guidance during the chip design process. I am honored to have worked with both of them. I also appreciate the input and advice of Deborah Jin and Carl Wieman during the early years of my time at JILA.

This work was accomplished with the help of many fellow students and staff. I learned much of what I know about experimental physics during long hours spent with my former lab partners Quentin Diot and Ying-Ju Wang, as well as with fellow group members Daniel Farkas, Kai Hudek, Evan Salim, and Matthew Squires. Their contributions to this work are too many to mention individually. Scott Papp deserves a special mention for teaching me many tricks of the experimental trade. Leslie Czaia's assistance and advice was essential at many times during my career. Seth Caliga has been my undergraduate assistant during the final portion of my PhD, and is set to inherit this project from me. He has been a pleasure to mentor, and I look forward to seeing how far he will take the gyro during his own graduate career. Farhad Madjetemouri wrote the LabVIEW control program for the new apparatus. Undergraduates Andrew Holmgren,

William Holmgren, Marika Meertens, and Jonathan Pfeiffer also contributed their efforts. In addition, the JILA computing team and the staffs of the electronics and instrument shops supported this work with their expertise and patience on various occasions.

This research also relied on contributions from our group's partners. The atom chips used in the early Michelson interferometry experiments were fabricated by R. A. Saravanan from the group of Victor Bright, using the facilities of the group of Zoya Popovic. Later chips were fabricated by Robert Mihailovich's team at Teledyne Scientific (formerly Rockwell Scientific).

This project was primarily funded by the guided Bose-Einstein condensate interferometry program of the Defense Advanced Research Projects Agency's Defense Sciences Office.

Contents

Chapter

Appendix

Tables

Table

Figures

Figure

Chapter 1

Introduction

1.1 Motivation

Atomic physicists interested in basic research have devoted considerable effort to probing the fundamental properties of ultracold dilute gases in the last 15 years. Studies of these gases (specifically, Bose-Einstein condensates and degenerate Fermi gases) have examined superfluidity, coherent control of quantum systems, and various other subjects of interest. In more recent years, some researchers have become interested in developing practical applications for the interesting properties of ultracold systems. Ultracold atoms as sensitive probes of magnetic fields, ultracold atoms trapped in optical lattice potentials as simulators of novel quantum materials, and ultracold atoms as inertial sensors are all applications being actively pursued. Just as important as these proof-of-concept experiments are efforts to advance apparatus technology. Without a replacement for the custom-built, finicky, bulky machines that are used by most researchers, even a "killer" application for the ultracold will never emerge from the laboratory into popular use. We focus in this work on both the problems of technology and application development, with the eventual goal of testing advanced inertial sensors for navigation.

1.1.1 Navigation and gyroscopes

Precise and accurate navigation is essential to the successful operation of aircraft, naval vessels, spacecraft, and other vehicles. The global positioning system (GPS) allows modern navigators to "fix" the instantaneous location of a vehicle at a level of performance that would have been the envy of the celestial navigators of old. However, reliable navigation with GPS alone requires constant communication with the system's satellite network. Such communication is impractical for submarines, useless for space probes, and impossible for all vehicles when the GPS signal experiences interference (possibly due to hostile jamming).

A navigator may still calculate a vehicle's position when GPS is unavailable, using a time-tested method known as dead reckoning. Dead reckoning is a simple concept: the navigator calculates the vehicle's current position using its last known position and time-indexed measurements of its speed and heading [1]. In the modern practice of inertial navigation, these measurements are made by integrating the outputs of accelerometers and gyroscopes. The calculated displacement from the position of the last GPS update accumulates error due to the imperfections of the sensors used, so an accurate inertial navigation system must periodically correct itself with an updated GPS fix. With improved sensors, the time between GPS updates can be increased without reducing the accuracy of the position calculation. The development of gyroscopes with reduced errors is thus of significant practical interest.

1.1.2 Optical Sagnac effect gyroscopes

Modern navigational gyroscopes do not necessarily resemble the spinning wheel of the traditional mechanical device. The type of gyroscope addressed in this work, the Sagnac gyroscope, in fact has no moving parts. It is simply an interferometer in which the path taken by the interfering waves encloses an area. A schematic of an example using optical interference is shown in Fig. 1.1. Rotation of this device at angular velocity $\mathbf{\Omega}$ results in a phase shift between the counter-propagating waves, and therefore a shift in the fringe pattern detected at the output.

This phase shift $\Delta\phi$ is caused by the slight change of the length of the wave's path around the interferometer due to the rotation [3]. To calculate $\Delta\phi$, consider a waveguide of arbitrary shape, rotating around an arbitrary axis (see Fig. 1.2). Light is coupled into the waveguide at a beamsplitter (not shown); the light runs around the waveguide in both directions before reuniting at the beamsplitter. The time required for the light to traverse the infinitesimal

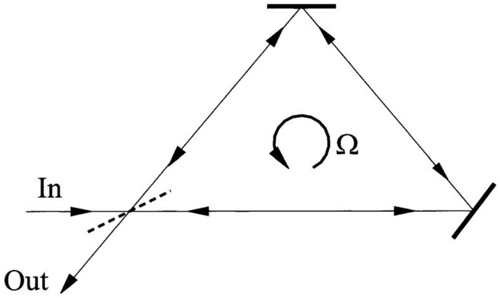

Figure 1.1: A schematic of a simple, optical Sagnac interferometer. Rotation of the device at angular velocity Ω causes a phase shift between the two arms [2].

distance dl is dl/c. The waveguide is moving due to the rotation; the component of the velocity due to rotation along the waveguide axis is given by

$$(\mathbf{\Omega} \times \mathbf{r}) \cdot \hat{\mathbf{l}}. \tag{1.1}$$

Here, $\mathbf{r}$ is the position of a location on the waveguide and $\hat{\mathbf{l}}$ is a unit vector pointing along the waveguide axis. If the rotation speed Ω is zero, then the optical path length around the guide is the same in both directions, and $\Delta\phi = 0$. If $\Omega \neq 0$, the path length for the light traveling in one direction is altered by

$$\Delta P = \frac{1}{c} \oint_{\text{ring}} (\mathbf{\Omega} \times \mathbf{r}) \cdot d\mathbf{l}, \tag{1.2}$$

where $\hat{\mathbf{l}}\ dl = d\mathbf{l}$. Applying Stokes's theorem, we have

$$\Delta P = \frac{1}{c} \int_{\text{ring}} \nabla \times (\mathbf{\Omega} \times \mathbf{r}) \cdot d\mathbf{A}. \tag{1.3}$$

To evaluate Eq. (1.3), we will apply the identity

$$\nabla \times (\mathbf{\Omega} \times \mathbf{r}) = \mathbf{\Omega}(\nabla \cdot \mathbf{r}) - \mathbf{r}(\nabla \cdot \mathbf{\Omega}) + (\mathbf{r} \cdot \nabla)\mathbf{\Omega} - (\mathbf{\Omega} \cdot \nabla)\mathbf{r}. \tag{1.4}$$

The identity $\nabla \cdot \mathbf{r} = 3$ reduces the first term in Eq. (1.4) to $3\mathbf{\Omega}$. The second and third terms vanish, since $\mathbf{\Omega}$ has no spatial dependence. The fourth term evaluates to

$$\begin{aligned} (\mathbf{\Omega} \cdot \nabla)\mathbf{r} &= (\Omega_x \partial_x + \Omega_y \partial_y + \Omega_z \partial_z)(x\hat{x} + y\hat{y} + z\hat{z}) \\ &= (\Omega_x \hat{x} + \Omega_y \hat{y} + \Omega_z \hat{z}) = \mathbf{\Omega}. \end{aligned} \tag{1.5}$$

We can now simplify Eq. (1.3) to

$$\Delta P = \frac{2}{c}\int_{\text{ring}} \mathbf{\Omega}\cdot d\mathbf{A} = \frac{2\mathbf{\Omega}\cdot\mathbf{A}}{c}. \tag{1.6}$$

The light propagating along with the rotation will have its path length increased by ΔP, while the light propagating against the direction of rotation will have its path length decreased by the same amount. The overall phase shift is given by

$$\Delta\phi = 2k\Delta P = \frac{8\pi\mathbf{\Omega}\cdot\mathbf{A}}{\lambda c}, \tag{1.7}$$

where $\mathbf{k}$ is the wavevector and λ is the wavelength of the light.

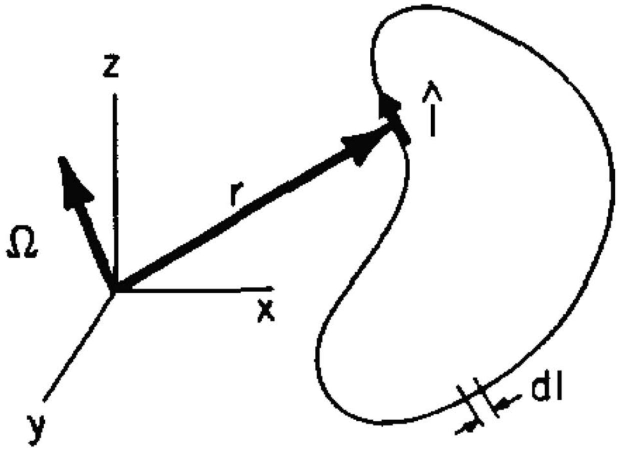

Figure 1.2: Interferometry waveguide of arbitrary shape, rotating at angular velocity $\mathbf{\Omega}$ [3].

To see if such a device would be practically useful, consider the case of a jet airliner traveling at a cruising velocity of about 1000 km/h. Its gyroscope must be sensitive to slow rotations at the scale of 15°/h (coincidentally, this is the Earth's rotation rate), or else the position calculated by the inertial navigation system will be off by kilometers after just a minute of flying. For a reasonably-sized circular interferometer of radius 5 cm, the path length shift at Earth rate is only 3.8×10^{-15} m. Using a light source operating at $\lambda = 850$ nm, (a typical telecommunications wavelength) the phase shift is 5.6×10^{-8} rad. This phase shift is too small to be easily measured interferometrically. At first glance, then, the sensitivity of an optical Sagnac gyroscope seems too small to be of practical use.

One method that has been successfully used to increase the sensitivity is to increase the enclosed area by replacing the single-pass waveguide with a long optical fiber wound around a spool. A 1 km fiber wound around the 5 cm radius we just considered would have a phase shift of about 180 μrad at Earth's rotation rate, well within the realm of reasonable interferometric detection (it becomes difficult to measure interferometric phase shifts when $\Delta\phi$ is smaller than 1 μrad [4]). Interferometric fiber optic gyroscopes (IFOGs) of this scale are currently used in the inertial navigation systems of a variety of vehicles, including the latest Airbus and Boeing airliners [4, 5] and the F-16 fighter (see Fig. 1.3).

Figure 1.3: (Color). Northrup Grumman LN-260 inertial navigation system with GPS. This unit is used in upgraded F-16 fighter aircraft. The two cylinders visible in the front of the unit each contain an IFOG [C. Volk, J. Lincoln, and D. Tazartes, Northrop Grumman's Family of Fiber-Optic Based Inertial Navigation Systems, (`http://www.es.northropgrumman.com/by_division/navigationsystems/whitepapers/assets/FOGINS_Paper_Final.pdf`)].

A reliable gyroscope design combines high sensitivity with low measurement errors. Phase shifts caused by anything other than rotation lead to a bias in the measured rotation rate, such that heading calculated by the navigation system eventually drifts from the true heading. For example, temperature variations cause phase shifts by mechanically straining or directly varying the refractive index of the fiber. Accelerations can distort the shape of the fiber coil. Stray magnetic fields can affect the polarization state of the propagating light. The sensitivity of the IFOG to these and other environmental bias sources is greatly reduced by the reciprocal beam path of the device. The IFOG's remaining sensitivity to environmental bias can be measured and calibrated out of the measurement, so the true figure of merit for an IFOG's noise performance is the stability of the bias (rather than its magnitude). Bias stability of less than 0.0003°/h has been measured in high-grade IFOGs [1].

Unfortunately, IFOG technology has not led to inertial navigation systems that are completely independent of GPS updates. Using the 1 μrad detection limit just introduced, the minimum measurable rotation rate of the 1 km fiber gyroscope we have considered is about 0.1°/hr or 0.5 μrad/s. The position error after one hour of flight of an airliner using this device will already be a few kilometers [6]. Practically, the minimum measurable rotation rate must drop by 3 orders of magnitude for the position error after one hour to be less than a few meters. The sensitivity can be increased by using a longer fiber or a larger radius [7], but eventually the device would become too large to be practical [4].

1.1.3 Matter-wave Sagnac gyroscopes

The IFOG reaches its sensitivity by effectively increasing the numerator of Eq. (1.7); another way to reach high sensitivity would be to decrease its denominator. One way to do this is to replace optical with matter-wave interference. In this case, Eq. (1.7) would become

$$\begin{aligned}\Delta\phi_{\mathrm{matter}} &= \frac{8\pi\mathbf{\Omega}\cdot\mathbf{A}}{\lambda_{\mathrm{dB}}\, v} \\ &= \frac{4M\mathbf{\Omega}\cdot\mathbf{A}}{\hbar},\end{aligned} \tag{1.8}$$

where M is the mass of the interfering particles. We have replaced the wavelength and speed of light with the deBroglie wavelength λ_{dB} and propagation speed v of the particles. Note that $\Delta\phi$ does not actually depend on v. We can compare the sensitivity of a matter-wave gyroscope to a given rotation to that of an optical gyroscope enclosing the same area by taking the ratio of Eq. (1.7) to Eq. (1.8):

$$\frac{\Delta\phi_{\mathrm{matter}}}{\Delta\phi_{\mathrm{photon}}} = \frac{\lambda M c}{h}. \tag{1.9}$$

If the optical gyroscope operates at $\lambda = 850$ nm and the matter-wave gyroscope uses ^{87}Rb atoms (a convenient atom for laser and evaporative cooling, $M = 1.44 \times 10^{-25}$ kg), Eq. (1.9) gives

$$\frac{\Delta\phi_{\text{matter}}}{\Delta\phi_{\text{photon}}} = 5 \times 10^{10}. \tag{1.10}$$

This enormous increase in phase shift makes a matter-wave gyroscope a candidate for use in GPS-denied navigation. Consider a gyroscope that records a phase shift $\Delta\phi = \pi$ rad when spinning on-axis at Earth's rotation rate. Using the practical sensitivity limit of $\Delta\phi = 1$ μrad discussed previously (though this limit is quite ambitious for atomic detection methods), the minimum measurable rotation rate for such a device would be

$$\begin{aligned} \Omega_{\min} &= \frac{\Omega_{\text{Earth}}}{\pi} \times 10^{-6} \\ &= 23 \text{ prad/s} = 4.8\ \mu\text{deg/h}. \end{aligned} \tag{1.11}$$

Such a gyroscope would enable an INS to keep position errors due to the coarseness of the gyroscope small over long periods of time. The enclosed area required for this sensitivity may be calculated using Eq. (1.8). Again considering ^{87}Rb, we find $A = 7.9$ mm^2. A single-pass, circular path of this area would have a radius of only 1.6 mm. This device would be both smaller and more sensitive than the IFOG considered in the previous section.

1.1.4 Shot noise in Sagnac gyroscopes

Shot noise places a fundamental limit on the precision of a Sagnac gyroscope's rotation rate measurement. This limit is not important in IFOGs, where the high flux of photons from a bright light source pushes the shot noise limit below the minimum set by other practical limits of the system. In the case of the low-flux sources available for matter-wave gyroscope, shot noise must be considered.

We estimate the shot noise limit on the uncertainty of a Sagnac interferometer by considering the recombination of the interfering waves at the output beamsplitter [2]. We will here consider the optical case for simplicity, but the mathematics and the resulting estimate of the shot noise limit is also correct for matter waves. Assume that the incoming uniform light beams have acquired a phase shift of $\Delta\phi$ during their travel through the interferometer. A pair of ideal detectors counts the number of photons at the outputs of the beamsplitter (see Fig. 1.4), recording

$$\begin{aligned} N_1 &= N_T \sin^2(\Delta\phi) \\ N_2 &= N_T \cos^2(\Delta\phi). \end{aligned} \tag{1.12}$$

Here, $N_T = N_1 + N_2$ is the total number of photons detected. We ignore any additional beamsplitter-related phase shifts. We combine these two equations to obtain

$$\tan^2(\Delta\phi) = \frac{N_1}{N_2}. \tag{1.13}$$

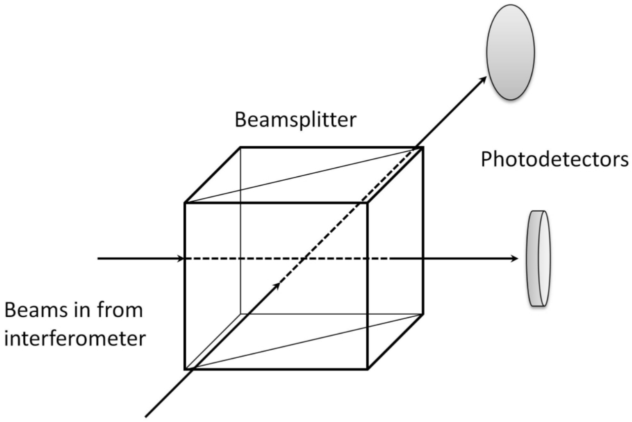

Figure 1.4: The two output beams of an optical interferometer are recombined at a beamsplitter. Ideal photodetectors count the photons at the beamsplitter's outputs. Inspired by [2].

The shot noise uncertainty of the photodetector measurements,

$$\begin{aligned} \delta N_1 &= \sqrt{N_1} \\ \delta N_2 &= \sqrt{N_2}, \end{aligned} \tag{1.14}$$

results in an uncertainty in $\Delta\phi$. The total differential of Eq. (1.13) shows how the two are related:

$$\frac{2\tan(\Delta\phi)}{\cos^2(\Delta\phi)}\, d(\Delta\phi) = \frac{N_2\ dN_1 - N_1\ dN_2}{N_2^2}. \tag{1.15}$$

The two terms on the right side of Eq. (1.15) contribute independently to the uncertainty $\delta(\Delta\phi)$. Therefore, $\delta(\Delta\phi)$ results from their sum in quadrature:

$$\frac{2\tan(\Delta\phi)}{\cos^2(\Delta\phi)}\delta(\Delta\phi) = \frac{\sqrt{(N_2\ \delta N_1)^2 + (N_1\ \delta N_2)^2}}{N_2^2}. \tag{1.16}$$

Using Eqs. (1.12) and (1.14), Eq. (1.16) simplifies to

$$\delta(\Delta\phi) = \frac{1}{2\sqrt{N_T}}. \tag{1.17}$$

Assuming that Eq. (1.17)'s estimate of $\delta(\Delta\phi)$ is the dominant source of uncertainty in our Sagnac experiment, we insert it into Eq. (1.7) to find the uncertainty in Ω:

$$\begin{aligned} \delta\Omega &= \frac{\lambda c}{8\pi A}\delta(\Delta\phi) \\ &= \frac{\lambda c}{16\pi A\sqrt{N_T}}. \end{aligned} \tag{1.18}$$

This equation is correct for an interferometer aligned with its rotation axis. To find $\delta\Omega$ for a matter wave gyroscope, we simply replace λ and c with their matter equivalents. The result is

$$\delta\Omega_{\text{matter}} = \frac{\hbar}{8MA\sqrt{N_T}}. \tag{1.19}$$

If, as above, we use ^{87}Rb atoms and set $A = 7.9$ mm^2, the uncertainty is

$$\delta\Omega = \frac{11.6}{\sqrt{N_T}}\ \mu\text{rad/s} = \frac{2.4}{\sqrt{N_T}}\ \text{deg/h}. \tag{1.20}$$

We see that if our atom gyroscope operates with a packet of 60000 atoms, it beats the minimum measurable rotation rate of the IFOG described in Sec. 1.1.2 by an order of magnitude. Further performance gains would be realized with a larger flux of atoms.

1.1.5 Thermal beam atom gyroscope experiments

The predicted excellent performance of matter wave gyroscopes has been realized in the laboratory, with one experiment achieving a rotational sensitivity of 6×10^{-10} rad/(s/$\sqrt{\text{Hz}}$) [8, 9]. Figure 1.5 shows a schematic of the experiment. The high sensitivity and low noise are the result of the large enclosed area of the beam path (22 mm^2) and the high flux of the thermal beam atom source (10^{11} atoms/s).

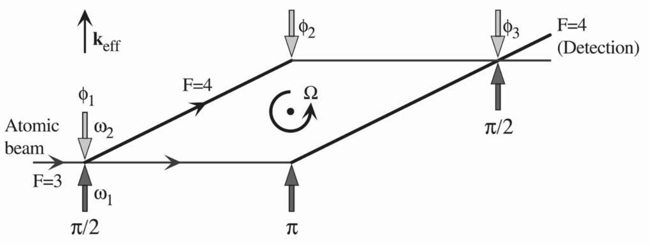

Figure 1.5: Thermal beam atom gyroscope from [9]. The transverse momentum of the beam is controlled by optical Raman transitions. These transitions also transfer the atoms between two hyperfine ground states (labeled as $F = 3$ and $F = 4$).

The source is an oven containing a high-pressure vapor of Cs atoms. The oven is connected to an otherwise sealed vacuum tube through a small hole. Escaping atoms travel down the tube in a high-flux beam, moving at the speed determined by the vapor's thermal energy (290 m/s). Note that the path of the atoms is not reciprocal, making this experiment sensitive to environmental bias. An upgraded version of this experiment [10] contains two gyroscopes, using two counter-propagating beams as the atom sources. This version has a measured bias stability of < 70 μdeg/h.

Laser beams control the beam's path through the tube. At the entrance to the tube, the beam is optically pumped into the $F = 3$ hyperfine ground state. A pair of counterpropagating laser beams, aligned transverse to the beam, is then applied. These beams are tuned to transfer the atoms into a coherent superposition of the two ground states, via a $\pi/2$ two-photon stimulated Raman transition [11]. The process of absorption from one beam and stimulated emission into the other gives the atoms transferred into the $F = 4$ ground state a transverse velocity kick of $2\hbar k/M = 7$ mm/s. (This language is approximate. No atoms are actually "transferred" between states in the creation of the superposition). The $\pi/2$ Raman transition thereby splits the beam into two paths. A π Raman transition, applied at the halfway point of the tube, acts as a mirror. It "flips" atoms from one transverse momentum and hyperfine state to the other. By arranging pairs of Raman beams as shown in Fig. 1.5, the single atomic beam is converted into an area-enclosing Sagnac interferometer.

While impressive, this gyroscope is not portable. The great mismatch between the forward and transverse velocities of the beam (a ratio of 4×10^4) requires an elongated path to enclose the desired area. In [9], the path is just under 2 m long. A design of practical size must be able to achieve a similar enclosed area in a much smaller package.

1.1.6 Advantages of using ultracold, guided atoms in gyroscopes

An alternative approach to the problem is to guide the interfering atoms around a more circular path, instead of allowing them to freely propagate. One candidate for guiding atoms is the magnetic microtrap [12], generated by current run through wires patterned onto a microchip (called an "atom chip"). The wire magnetic field, plus a transverse bias field, produces a magnetic waveguide or trap for atoms in weak field seeking states. Almost any shape of waveguide can be generated by properly designing the wire pattern, including the reciprocal beam paths that are desired for reducing measurement bias. Microtraps are suitable for use in portable devices, due to their small size and power needs.

A thermal beam is an inappropriate source of atoms for a microchip waveguide, however. The depth of the waveguide potential is set by the magnitude of the bias field and the magnetic moment of the atomic state to be used. For the doubly polarized ground state of the alkali metals, the depth is $\mu_{\mathrm{B}} B_0$. We see that even a high bias field of $B_0 = 100$ G would create a trap that could barely hold a gas at 7 mK, let alone the oven-heated atoms in a thermal beam.

On the other hand, microchip waveguides are perfectly appropriate for confining ultracold gases, such as Bose-Einstein condensates (BECs). Since a BEC is a coherent, macroscopic sample of atoms, its interference pattern should have high contrast. This fringe visibility enhancement is analogous to that found when comparing laser to white light interferometers. Moreover, BECs are well-suited for use with the laser beamsplitters and mirrors used in atom optics, in which the efficiency is often sensitive to the thermal velocity distribution of the atoms. A BEC's delta-function velocity distribution allows for near-perfect efficiencies in momentum state manipulation.

1.2 Outline of dissertation

With these motivations in mind, the construction and testing of a compact Sagnac gyroscope using guided, Bose-condensed atoms is a worthy goal. The work presented in this dissertation consists of some of the preliminary work needed to reach that mark. The research was carried out over the course of two projects. The first project, which was already underway before the period covered by this dissertation, focused on the demonstration and investigation of guided BEC Michelson interferometry in a microchip waveguide. This project concluded with the demonstration of high-contrast interference patterns obtained after BEC propagation of approximately 250 ms. Its results have been detailed in other dissertations, and will therefore be presented only in summary here. The lessons learned from this first project have been applied in the opening stages of the second project, whose goal is the demonstration of a guided BEC Sagnac gyroscope. The portion of this project covered by this dissertation focused on the design and construction of a new, compact apparatus.

This dissertation contains my contributions to these two projects. Chapter 2 reviews the principles of the two primary atom-optical elements used in the experiments: microtrap waveguides and light gratings for atomic diffraction. Chapter 3 explains the final Michelson interferometry experiments, and includes a short description of the apparatus used. Chapter 4 presents the application of the statistical methods of principal and independent component analysis to data from the Michelson experiments. Chapter 5 discusses the results and the lessons learned from these experiments. Chapter 6 explains the design of an atom chip for Sagnac measurements. Chapter 7 describes the design, construction, and initial testing of a compact, rotating BEC apparatus that incorporates the new chip design.

Chapter 2

Atom optics: Waveguides and diffraction grating beamsplitters

The IFOG relies relies on familiar optical elements to control the path of its interfering light; an atom gyroscope must have equivalent "atom-optical" elements. Our proposed gyroscope will use magnetic waveguide potentials to control the path of the atoms and diffraction from standing waves of light to split and recombine the matter wave. This chapter reviews these two techniques.

2.1 Magnetic microtraps and waveguides for atoms

In our experiments, guiding potentials for neutral atoms are generated with magnetic fields. Consider an atom with total angular momentum **F** interacting with a magnetic field **B**. The energy of the atom is

$$U = g_F m_F \mu_{\mathrm{B}} B. \tag{2.1}$$

In this equation, g_F is the Landé g factor of the total angular momentum state, m_F is the quantum number of the projection of **F** along **B**, and μ_{B} is the Bohr magneton. We see that a local magnetic field minimum is a potential well for an atom in any state in which $g_F m_F > 0$. A potential well of this type extending in two dimensions is called a magnetic waveguide, while a well confining in all three dimensions is called a magnetic trap.

The microtrap is a compact, low-power device that can generate such magnetic traps and waveguides for cold, neutral atoms. To lowest order, the steepness of a magnetic potential is characterized by the gradient of the field. The fields are typically generated by electric currents traveling through single wires or coils, or else by permanent magnets. The gradient of a current-generated field scales as

$$B' \propto \frac{I}{r^2}, \tag{2.2}$$

where r is the distance between the current-carrying coil or wire and the trap position and I is the current. It is therefore possible to construct steep traps using either (a) powerful permanent magnets, (b) coils carrying hundreds of amperes of current placed a few centimeters from the trap center, or (c) single wires carrying a few amperes placed a few hundred micrometers from the trap center. It is approach (c) that has inspired the development of the microtrap, which can practically attain significantly tighter traps than the other alternatives. Since atoms confined more tightly collide at an increased rate, evaporative cooling can proceed significantly faster in microtraps without any loss of efficiency. The benefits in speed, size, and power have made microtraps attractive for the development of portable, high-bandwidth atom interferometers. In this section, we will describe the theory of the microtrap elements used in our experiments and give a short description of fabrication techniques. Further details on the development and use of the microtrap are outlined in [12] and [13].

2.1.1 Side guide

The building block of the microtrap is a simple linear, quadrupole waveguide (the "side guide"). It is generated by a straight current-carrying wire and a uniform bias field, oriented perpendicular to the wire (see Fig. 2.1). The wire current (flowing along the z-axis) generates the familiar circular magnetic field, so the total field can be written as

$$\mathbf{B} = (B_{0,x},\ 0,\ 0) + \frac{\mu_0 I_z}{2\pi(x^2+y^2)}(-y,\ x,\ 0). \tag{2.3}$$

Here, $B_{0,x}$ is the magnitude of the transverse bias field and I_z is the current in the wire. The form of Eq. (2.3) assumes the wire is infinitely thin and long, but is approximately correct for real wires at distances that are further from the wire than its width but much shorter than the

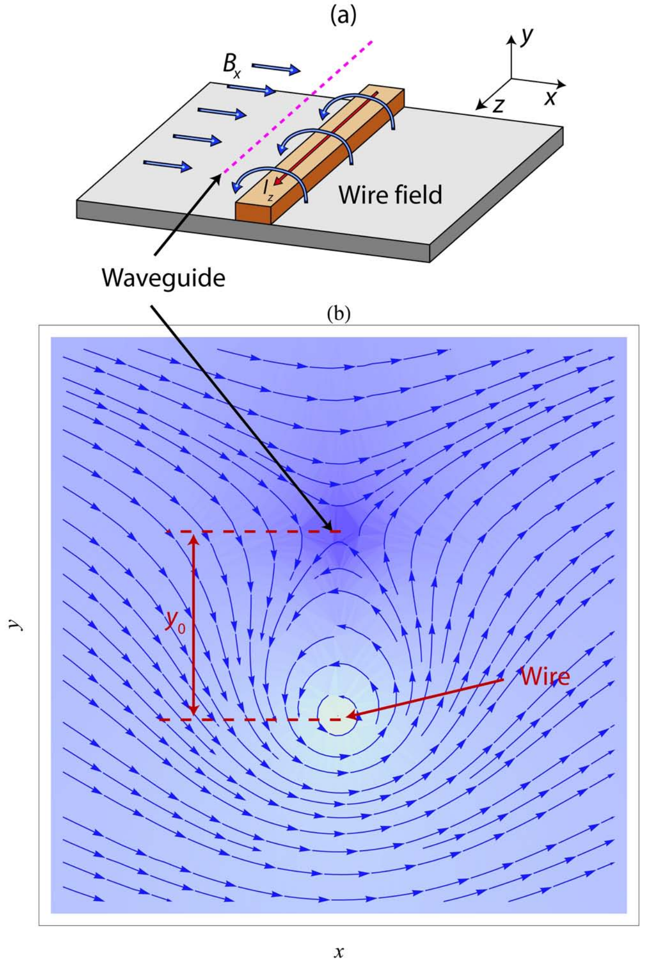

Figure 2.1: (Color). (a) A schematic of a simple side guide. Here, the straight current-carrying conductor (current I_z) is a wire on the surface of an insulating substrate. The wire field and bias B_x cancel along the magenta dotted line, forming a waveguide for atoms in weak magnetic field seeking states. (b) Plot of side guide's quadrupole magnetic field. Streamlines indicate field direction. Color indicates field magnitude, with darker colors corresponding to lower field.

wire's length. The two contributions cancel along the line parallel to the wire defined by

$$\begin{aligned}\mathbf{x}_0 &= \left(0,\ \frac{\mu_0 I_z}{2\pi B_{0,x}},\ z\right)\\ &= (0,\ y_0,\ z).\end{aligned} \tag{2.4}$$

We may Taylor expand the field magnitude B around x_0 to obtain

$$B \approx \frac{B_{0,x}}{y_0}\rho, \tag{2.5}$$

where

$$\rho = \sqrt{x^2 + (y - y_0)^2}. \tag{2.6}$$

We see that the side guide potential is a linear/quadrupole waveguide for weak-field seeking atoms.

The side guide is not by itself capable of confining ultracold atoms. Since the field magnitude goes to zero at the center, Majorana transitions will cause atoms to fall out of the guide. The simplest way to prevent these losses is to add a second uniform bias field oriented along the waveguide axis. The total field is now

$$\mathbf{B} = (B_{0,x},\ 0,\ B_{0,z}) + \frac{\mu_0 I_z}{2\pi(x^2 + y^2)}(-y,\ x,\ 0), \tag{2.7}$$

for axial bias $B_{0,z}$. The field magnitude near the guide center is approximately

$$B \approx B_{0,z} + \frac{B_{0,x}^2}{2y_0^2 B_{0,z}}\rho^2. \tag{2.8}$$

We see that the guide is harmonic in the biased case, with a trapping frequency

$$\begin{aligned}\omega_\rho &= \sqrt{\frac{g_F m_F \mu_\mathrm{B}}{M}\frac{d^2 B}{d\rho^2}}\\ &\approx \sqrt{\frac{g_F m_F \mu_\mathrm{B}}{M B_{0,z}}}\frac{2\pi B_{0,x}^2}{\mu_0 I_z}.\end{aligned} \tag{2.9}$$

2.1.2 Crossed wire trap

A simple three-dimensional trap can be made by crossing two wires at right angles. Once again using the limit of infinitely thin and long wires, the field contribution of the additional wire at the waveguide is

$$\mathbf{B}_{\rm c} = \frac{\mu_0 I_x}{2\pi(y_0^2 + z^2)}(0,\ z,\ -y_0) \tag{2.10}$$

for a crossing wire carrying current $-I_x$ along the x axis and intersecting the main wire at (0,0,0) [see Fig. 2.2(a)]. In general, the second wire could be displaced along the y axis by a distance d. In either case, the new wire's field has no x component, and therefore the field minimum will still be at $y = y_0$. By Taylor expanding around $z = 0$ [14], we find

$$\begin{aligned} B_{{\rm c},y} &= \frac{\mu_0 I_x z}{2\pi[(d+y_0)^2 + z^2]} \\ &\approx \frac{\mu_0 I_x}{2\pi(d+y_0)^2} z \\ B_{{\rm c},z} &= -\frac{\mu_0 I_x (d+y_0)}{2\pi[(y_0+d)^2 + z^2]} \\ &\approx -\frac{\mu_0 I_x}{2\pi(d+y_0)} + \frac{\mu_0 I_x}{2\pi(d+y_0)^3} z^2 - \frac{\mu_0 I_x}{2\pi(d+y_0)^5} z^4. \end{aligned} \tag{2.11}$$

For the case in which $I_x \ll I_z$, the field at the minimum $(0, y_0, 0)$ is to lowest order

$$B \approx B_{0,{\rm c}} + \frac{B_{0,{\rm c}}^2}{2y_0 B_{0,z}}\rho^2 + \frac{\mu_0 I_x}{2\pi(d+y_0)^3} z^2. \tag{2.12}$$

The trap frequencies are

$$\begin{aligned} \omega_\rho &= \sqrt{\frac{g_F m_F \mu_{\rm B}}{M B_{0,{\rm c}}} \frac{2\pi B_{0,x}^2}{\mu_0 I_z}} \\ \omega_z &= \sqrt{\frac{g_F m_F \mu_{\rm B}}{M} \frac{\mu_0 I_x}{2\pi(d+y_0)^3}}, \end{aligned} \tag{2.13}$$

where

$$B_{0,{\rm c}} = B_{0,z} - \frac{\mu_0 I_x}{2\pi(d+y_0)}. \tag{2.14}$$

The combined potential consists of the radial waveguide along with a superimposed axial "dimple" in the space just over the crossing wire, where its field partially cancels $B_{0,z}$. The axial potential is only harmonic in a fairly small region around $|z| = 0$, due to the fourth-order term in Eq. (2.11). To see the effect of this term [15], consider a potential

$$U = b_2 z^2 + b_4 z^4. \tag{2.15}$$

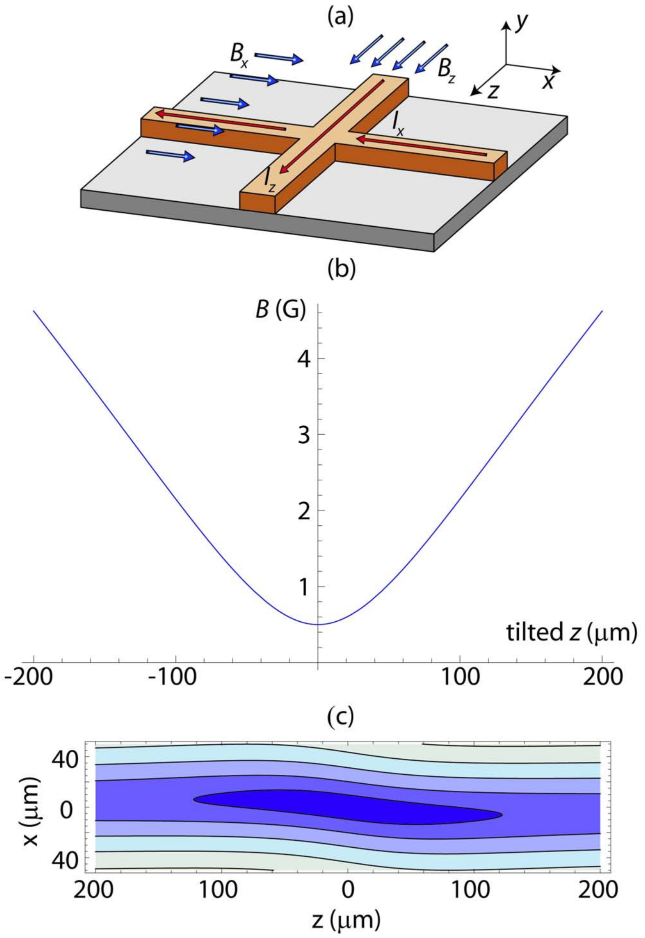

Figure 2.2: (Color). (a) Schematic of crossed wire ("dimple") trap on a chip. In this example $d = 0$; the wires actually cross. (b) Plot of magnetic field magnitude along tilted weak trap axis for $I_z = 1$ A, $I_x = 125$ mA, $B_{0,x} = 20$ G, $B_{0,z} = 3$ G, $y = y_0 = 100$ μm. The field magnitude is only parabolic in shape near the trap center. (c) Contour plot of same configuration. Dark color indicates lower field.

The harmonic trap frequency of this potential is

$$\begin{aligned}\frac{1}{2}M\omega_z^2 z^2 &= \frac{1}{2}z^2\frac{\partial^2 U}{\partial z^2}\\ &= \frac{1}{2}z^2(2b_2 + 12b_4 z^2)\\ \omega_z^2 &= \frac{2b_2}{M}\left(1+\frac{6b_4 z^2}{b_2}\right).\end{aligned} \tag{2.16}$$

The frequency stays at the value expected for $b_4 = 0$ as long as

$$\left|\frac{6b_4 z^2}{b_2}\right| \ll 1. \tag{2.17}$$

For the dimple potential, the harmonic region of the axial potential is therefore

$$z^2 \ll \frac{(d+y_0)^2}{6}. \tag{2.18}$$

Figure 2.2(b) shows the axial potential for typical parameters at $y = y_0 = 100$ μm and $d = 0$. The potential is clearly only a parabola near $|z| = 0$.

Another consequence of the addition of the crossing wire is that the y component of the total field no longer vanishes at $x = 0$. We have instead

$$B_y = \frac{\mu_0}{2\pi}\left(\frac{I_z x}{x^2 + y_0^2} + \frac{I_x z}{(d+y_0)^2 + z^2}\right). \tag{2.19}$$

This component vanishes along a line given to first order by

$$x \approx -\frac{I_x y_0^2}{I_z (d+y_0)^2} z. \tag{2.20}$$

The weak axis of the trap is therefore tilted away from the x axis by

$$\tan\theta \approx -\frac{I_x y_0^2}{I_z (d+y_0)^2}. \tag{2.21}$$

This tilt is apparent in Fig. 2.2(c).

A variant of the crossed wire trap is the T trap [16], in which the crossing wire only exists on one side of the main wire (see Fig. 2.3). The most obvious difference between the T trap and the cross trap is that the z component of the magnetic field is cut in half: $B_{\mathrm{T},z} = B_{\mathrm{c},z}/2$. The trap frequency ω_z is therefore smaller by $1/\sqrt{2}$ for the same current, and the dimple potential is half as deep. The other difference is that the current flowing in the T wire must flow along with the main wire's current on one side of the wire pattern. As a result, the waveguide will be slightly further away from the main wire on that side.

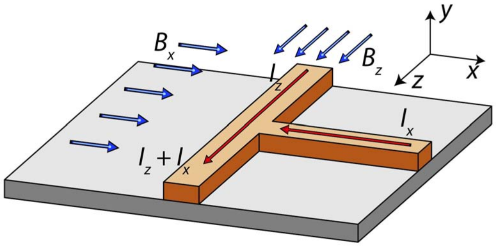

Figure 2.3: (Color). Schematic of a T trap.

2.1.3 H trap

Instead of using a single wire to generate axial confinement in the waveguide, we could instead use a pair of wires. An H-shaped pattern could be formed by two wires crossing the main wire, separated by a distance L_{H} (see Fig. 2.4). The "leg" wires can also be displaced by d from the main wire along the y axis. The field of these wires at the waveguide is

$$\begin{aligned}
B_{\mathrm{H},y} &= -\frac{\mu_0 I_{\mathrm{H}}}{2\pi}\left(\frac{z+L_{\mathrm{H}}/2}{(d+y_0)^2+(z+L_{\mathrm{H}}/2)^2}+\frac{z-L_{\mathrm{H}}/2}{(d+y_0)^2+(z-L_{\mathrm{H}}/2)^2}\right)\\
&\approx -\frac{4\mu_0 I_{\mathrm{H}}[4(d+y_0)^2-L_{\mathrm{H}}^2]}{\pi[4(d+y_0)^2+L_{\mathrm{H}}^2]^2}z\\
B_{\mathrm{H},z} &= \frac{\mu_0 I_{\mathrm{H}}}{2\pi}\left(\frac{d+y_0}{(d+y_0)^2+(z+L_{\mathrm{H}}/2)^2}+\frac{d+y_0}{(d+y_0)^2+(z-L_{\mathrm{H}}/2)^2}\right)\\
&\approx \frac{4\mu_0 I_{\mathrm{H}}(d+y_0)}{\pi[4(d+y_0)^2+L_{\mathrm{H}}^2]}-\frac{16\mu_0 I_{\mathrm{H}}(d+y_0)[4(d+y_0)^2-3L_{\mathrm{H}}^2]}{\pi[4(d+y_0)^2+L_{\mathrm{H}}^2]^3}z^2\\
&\quad+\frac{64\mu_0 I_{\mathrm{H}}(d+y_0)\{16(d+y_0)^4+5L_{\mathrm{H}}^2[L_{\mathrm{H}}^2-8(d+y_0)^2]\}}{\pi[4(d+y_0)^2+L_{\mathrm{H}}^2]^5}z^4.
\end{aligned} \tag{2.22}$$

The field magnitude at the minimum $(0, y_0, 0)$ is approximately

$$B \approx B_{0,\mathrm{H}}+\frac{B_{0,x}^2}{2y_0^2 B_{0,H}}\rho^2+\frac{16\mu_0 I_{\mathrm{H}}(d+y_0)[3L_{\mathrm{H}}^2-4(d+y_0)^2]}{\pi[4(d+y_0)^2+L_{\mathrm{H}}^2]^3}z^2. \tag{2.23}$$

The trap frequencies are

$$\begin{aligned}\omega_\rho &= \sqrt{\frac{g_F m_F \mu_\mathrm{B}}{M B_{0,\mathrm{H}}}\frac{2\pi B_{0,x}^2}{\mu_0 I_z}}\\ \omega_z &= \sqrt{\frac{g_F m_F \mu_\mathrm{B}}{M}\frac{32\mu_0 I_\mathrm{H}(d+y_0)[3L_\mathrm{H}^2-4(d+y_0)^2]}{\pi[4(d+y_0)^2+L_\mathrm{H}^2]^3}},\end{aligned} \tag{2.24}$$

where

$$B_{0,\mathrm{H}} = B_{0,z} + \frac{4\mu_0 I_\mathrm{H}(d+y_0)}{\pi[4(d+y_0)^2+L_\mathrm{H}^2]}. \tag{2.25}$$

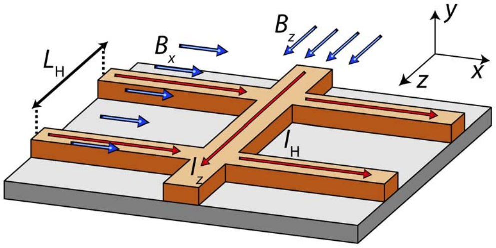

Figure 2.4: (Color). Schematic of H wire trap, with H wires separated by distance L_H.

An advantage of the H-wire configuration over the single crossing wire is that the anharmonic, fourth-order term in the axial confinement vanishes if

$$0 = 16(d+y_0)^4 + 5L_\mathrm{H}^2[L_\mathrm{H}^2 - 8(d+y_0)^2]. \tag{2.26}$$

By carefully choosing d and L for a given y_0, the anharmonicity parameter

$$\left|\frac{6b_4 z^2}{b_2}\right| = \left|\frac{24\{16(d+y_0)^4 + 5L_\mathrm{H}^2[L_\mathrm{H}^2-8(d+y_0)^2]\}}{[4(d+y_0)^2+L_\mathrm{H}^2]^2}\right| z^2 \tag{2.27}$$

can be kept quite small even at large distances from the trap center. Similarly, the tilt of the weak trap axis due to the y component of the H wire field can designed to be quite small. The axis lies along the line

$$x \approx \frac{8I_\mathrm{H}[4(d+y_0)^2 - L_\mathrm{H}^2]y_0^2}{I_z[4(d+y_0)^2+L_\mathrm{H}^2]^2}z, \tag{2.28}$$

tilting away from the x axis by the angle

$$\tan\theta \approx \frac{8I_\mathrm{H}[4(d+y_0)^2 - L_\mathrm{H}^2]y_0^2}{I_z[4(d+y_0)^2+L_\mathrm{H}^2]^2}. \tag{2.29}$$

The angle θ vanishes if the numerator is zero.

A useful variant of the H trap is known as a Z trap. Recall that the T trap is a variant of the crossed wire trap with the axial trapping wire cut back on one side; the Z trap similarly removes the $+x$ side of one of the H's crossing wires and the $-x$ side of the other. The similar result is a reduction in ω_z by a factor of $1/\sqrt{2}$. A finite-length Z wire can be created by bending a straight wire at both ends; this configuration is driven by a single current supply.

2.1.4 Fabrication of microtraps

The method of fabrication of wire structures for microtraps varies according to the desired distance between the wire and the trap center. Wires that are not terribly close to the trap center ($d + y_0 > 1$ mm) are easily fabricated by attaching thin copper wires to a suitable surface or support structure. The wires that are closest to the atoms ($d = 0$), however, are fabricated on a chip substrate by lithography. A variety of wire metals, substrates, and fabrication techniques have been used to create these "atom chips"; see [12] for a review.

The substrate used in our work is Si coated with an oxide insulating layer. Silicon is by far the most commonly used substrate material in microfabrication, where it is used in semiconductors, integrated circuits, computer chips, and microelectromechanical systems. These applications have driven decades of effort into developing reliable Si fabrication techniques. By using Si substrates, we take advantage of this work. Additionally, Si's good thermal conductivity (relative to other crystalline substrate materials) allows Si atom chips to dissipate more electrical power without heating [17]. The chips used in the early stages of this work used a ceramic substrate material that has a higher thermal conductivity: AlN. However, the relatively poor surface quality of wires patterned on AlN precluded its use in further work.

The wires on our atom chips are fabricated by photolithographic patterning, followed by electroplating the patterned wires to a thickness of about 10 μm. Our group has found Cu to be a good choice for the wire metal. Gold, which is more commonly used in microfabrication, is generally unsuitable for use in vacuum systems containing Rb (our preferred atomic species). Gold wires tend to absorb residual Rb vapor from the vacuum chamber, as the two metals readily form an alloy. This absorbed Rb is released when the wires are heated by the flow of current, bombarding the nearby trapped atoms and thereby lowering trap lifetimes [18].

2.2 Diffraction grating beamsplitters for atoms

Our Sagnac gyroscope experiment needs, in addition to the waveguide potentials discussed in the previous section, a method for splitting and recombining the interfering matter wave. In our work, the role of the beamsplitter is taken by coherent diffraction from gratings of light into a pattern of transverse momentum states. This section discusses the particular type of atomic diffraction used in our work; historical details and a review of other types of atomic beamsplitters may be found in [11].

A diffraction grating, in the broadest sense, is a periodic obstruction or potential that causes a wave interacting with it to scatter into a specific pattern of momentum states. In the familiar case of light passing interacting with a physical grating, the diffracted orders are separated in transverse momentum by

$$\Delta p = \frac{h}{D_g}, \tag{2.30}$$

where D_g is the period of the grating. In our experiments, a cloud of atoms interacts with an off-resonant standing wave of light, splitting the atoms into states of momentum along the axis of the standing wave that are separated by

$$\Delta p = 2h/\lambda = 2\hbar k. \tag{2.31}$$

The standing wave acts as a periodic potential for the atoms, playing a role analogous to that of a physical grating for beams of light.

A trapped condensate can be briefly exposed to a light grating by applying a pulse of the optical standing wave. A single, brief interaction populates many momentum states, with the distribution given by the theory of Kapitza-Dirac scattering. This is not quite the beamsplitter that we want for our interferometry experiments. We want a true 50/50 beamsplitter: the atoms exit it in a superposition of only two momentum states. One way to solve this problem is to use multiple weak gratings to control the diffraction pattern. This technique was first demonstrated and explained in [19, 20] and is reviewed in this section.

2.2.1 First order beamsplitter

Consider an atom exposed to a standing wave of light, where the wavenumber of the laser used is k_0. The AC Stark shift potential that the atom experiences may be written as

$$\begin{aligned} U(z,t) &= \frac{\hbar\Omega_{\mathrm{R}}^2(t)}{2\delta(t)}\cos 2k_0 z \\ &= \hbar\Omega_{\mathrm{E}}(t)\cos 2k_0 z, \end{aligned} \tag{2.32}$$

where Ω_{R} is the Rabi frequency, δ is the detuning from resonance, and Ω_{E} is the effective two-photon Rabi frequency. The effective Rabi frequency (and therefore the power and/or detuning of the laser) is time-dependent. This potential is correct in the limit of large detuning with respect to the Rabi and excited electronic state decay frequencies. The atomic state evolves according to

$$i\dot{\psi}(z,t) = \left(-\frac{\hbar}{2M}\frac{d^2}{dz^2} + \Omega_{\mathrm{E}}(t)\cos 2k_0 z\right)\psi(z,t). \tag{2.33}$$

By expanding the wavefunction in a Fourier series/integral

$$\psi(z,t) = \int d\mathbf{k}\sum_n C_{2n}(\mathbf{k},t)e^{i(2nk_0+k)z}, \tag{2.34}$$

Eq. 2.33 is transformed (via Fourier's trick) into

$$iC_{2n}(k,t) = \frac{\hbar}{2M}(2nk_0+k)^2 C_{2n}(k,t) + \frac{\Omega_{\mathrm{E}}(t)}{2}[C_{2n+2}(k,t) + C_{2n-2}(k,t)]. \tag{2.35}$$

Consider a system that is initially stationary, such that $k \ll k_0$ and only the $n = 0$ state is populated. If the grating is very weak, such that

$$\frac{\Omega_{\mathrm{E}}(t)}{2} \ll \frac{(2N_p)^2\hbar k_0^2}{2M} = (2N_p)^2\omega_r, \tag{2.36}$$

then momentum states $|2N_p|$ and higher will never be significantly populated (ω_r is the recoil frequency of the light). If we set $\Omega_{\mathrm{E}}(t) \ll 32\omega_r$, then the infinite set of equations may be truncated to only include $n = -1, 0, 1$. Making the unitary transformation

$$C_{2n}(k,t) \to \exp\left[-i\left(\frac{k}{k_0}\right)^2 \omega_r t\right] C_{2n}(k,t), \tag{2.37}$$

we can describe the system evolution by

$$\begin{aligned} i\dot{C}_0 &= \frac{\Omega_{\mathrm{E}}(t)}{2}[C_{-2}(k,t) + C_2] \\ i\dot{C}_2 &= 4\omega_r\left(1 + \frac{k}{k_0}\right) C_2 + \frac{\Omega_{\mathrm{E}}(t)}{2} C_0 \\ i\dot{C}_{-2} &= 4\omega_r\left(1 - \frac{k}{k_0}\right) C_{-2} + \frac{\Omega_{\mathrm{E}}(t)}{2} C_0. \end{aligned} \tag{2.38}$$

We define superposition states

$$\begin{aligned} C_+ &= \frac{1}{\sqrt{2}}(C_2 + C_{-2}) \\ C_- &= \frac{1}{\sqrt{2}}(C_2 - C_{-2}) \end{aligned} \tag{2.39}$$

and apply the approximation $k \ll k_0$, obtaining

$$\begin{aligned} i\dot{C}_0(k,t) &= \frac{\Omega_{\mathrm{E}}(t)}{\sqrt{2}} C_+ \\ i\dot{C}_+(k,t) &= 4\omega_r C_+ + \frac{\Omega_{\mathrm{E}}(t)}{\sqrt{2}} C_0 \\ i\dot{C}_-(k,t) &= 4\omega_r C_-. \end{aligned} \tag{2.40}$$

The "$-$" state is dark and will never be populated. Making one more unitary transformation

$$C \to e^{2i\omega_r t} C, \tag{2.41}$$

we find that we now have a simple two-state system

$$\begin{aligned} i\dot{C}_0 &= -2\omega_r C_0 + \frac{\Omega_{\mathrm{E}}(t)}{\sqrt{2}} C_+ \\ i\dot{C}_+ &= 2\omega_r C_+ + \frac{\Omega_{\mathrm{E}}(t)}{\sqrt{2}} C_0. \end{aligned} \tag{2.42}$$

This system is best visualized on a Bloch sphere. If we set $C_0 = e^{i\phi}\sin\theta/2$, $C_+ = \cos\theta/2$, $\mathbf{r}_s = (\sin\theta\cos\phi, \sin\theta\sin\phi, \cos\theta)$, and define the Rabi vector $\mathbf{\Omega}_{\mathrm{R}} = (\sqrt{2}\Omega_{\mathrm{E}}(t), 0, 4\omega_r)$, then Eq. (2.43) is transformed to

$$\frac{d\mathbf{r_s}}{dt} = \mathbf{\Omega}_{\mathrm{R}} \times \mathbf{r_s}. \tag{2.43}$$

A sequence of two square pulses of light can be used to place an initially stationary ensemble of atoms into the C_+ state (see Fig. 2.5). In the first pulse, the effective Rabi frequency is set to $\Omega_{\mathrm{E}} = 2\sqrt{2}\omega_r$. The Rabi vector for this pulse is $\boldsymbol{\Omega}_{\mathrm{R}} = 4\omega_r(1, 0, 1)$, with magnitude $\Omega_{\mathrm{R}} = 4\sqrt{2}\omega_r$. After half of a precession period, $\tau_1 = \pi/(4\sqrt{2}\omega_r)$, the state vector has rotated up to the xy plane of the Bloch sphere, pointing along the $-x$ axis. At this time, the light is shut off. The Rabi vector is now $\boldsymbol{\Omega}_{\mathrm{R}} = 4\omega_r(0, 0, 1)$, with magnitude $\Omega_{\mathrm{R}} = 4\omega_r$. After half of the dark precession period, $\tau_2 = \pi/(4\omega_r)$, the state vector has precessed around to the $+x$ direction. The light is turned on for a second pulse, with effective Rabi frequency and duration equal to that of the first. After this pulse, the state vector points along the z axis of the Bloch sphere, meaning the system is now in a superposition of the $2\hbar k_0$ and $-2\hbar k_0$ momentum states along the axis of the grating.

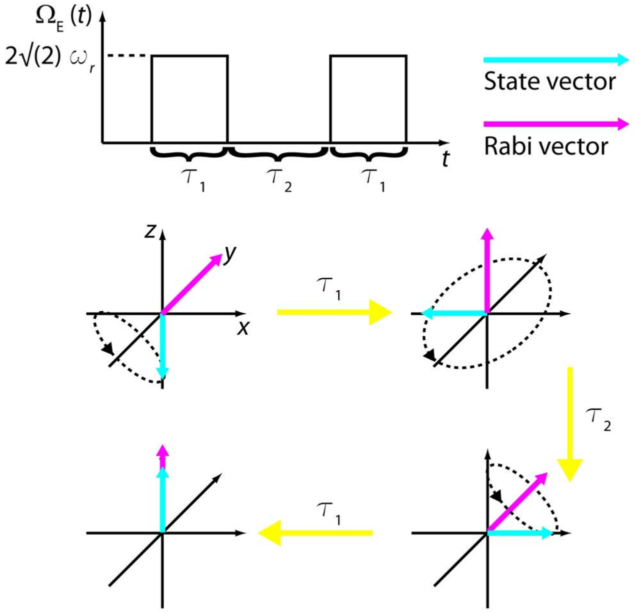

Figure 2.5: (Color). First order double-pulse optical beamsplitter. The upper plot shows the effective Rabi frequency as a function of time. The pictures at the bottom show the state of the system on the Bloch sphere at the beginning and end of each of the pulses. The yellow arrows indicate the progression from one state to the next. Adapted from [20].

2.2.2 Higher order beamsplitters

It is possible to extend the first order double-pulse concept to higher orders of diffraction, so that the momentum transferred to the cloud is $2n\hbar k_0$. By numerically integrating Eq. (2.35), optimized effective Rabi frequencies and pulse durations can be found for up to $n = 6$ with transfer efficiency above 85% [20]. Pulses up to $n = 3$ were experimentally demonstrated in [21]. Non-square pulses could also be used to increase the efficiency of higher-order diffraction pulses [22]. Even larger amounts of momentum have been transferred by Bragg diffraction [23], in which the pulse durations are longer than those used in the double-pulse scheme presented here.

Chapter 3

Michelson interferometry experiments with BECs

In this chapter, we present a guided Michelson-type interferometer using Bose-Einstein condensates. The two atom-optical elements presented in the previous chapter, magnetic microtraps and optical beamsplitters, are the key techniques that enabled these experiments. This work and the experimental apparatus used have been presented in previous dissertations [16, 24, 25] and publications [19, 26, 27]. This chapter will discuss only the final iteration of these experiments.

3.1 On-chip, free-return interferometry with BEC

The BEC interferometry experiment begins at $t = 0$ with a stationary condensate of ^{87}Rb atoms in the $|F = 1, m_F = -1\rangle$ ground state. The microtrap potential holding the condensate consists of an on-chip side guide at $\omega_\rho = 2\pi \times 80$ Hz, combined with a crossed wire trap adjustable between $\omega_z = 2\pi\times$ 4–6 Hz, centered 3.24 mm below the surface of the chip. A pair of mirror-coated prisms are epoxied onto the chip, perpendicular to both its surface and the guide axis. These mirrors are used to create the optical standing wave for the double pulse beamsplitter. The configuration is shown in Fig. 3.1. In the actual apparatus, the chip is mounted with the prisms pointing down so that clouds of atoms released from the trap will fall away from the chip instead of crashing into it.

At time $t = 0$, the first order double pulse beamsplitter is applied to the stationary BEC (see Fig. 3.2 for a schematic of interferometry sequence). Our implementation of the

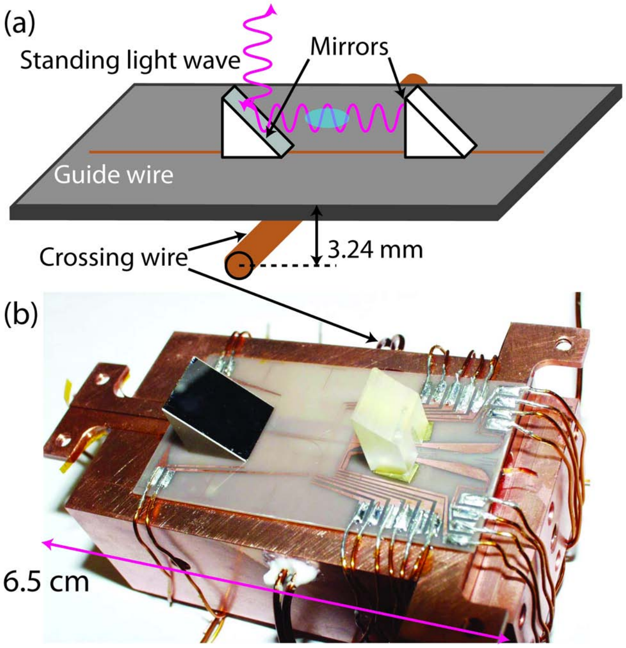

Figure 3.1: (Color). Michelson interferometry microtrap assembly, consisting of a side guide wire on a chip, a copper heat sink, a crossed wire trap displaced below the chip, and integrated mirrors for the optical grating. Schematic (a) and photograph of actual device (b) are shown. Other wires on the microchip visible in (b) are used for initial capture and cooling of atoms.

double pulse uses light at $k_0 = 2\pi/780$ nm, detuned 6.8 GHz to the red of atomic resonance. The condensate splits into two BECs, one traveling down the waveguide axis at initial velocity $v_0 = p_0/M = 2\hbar k_0/M = 11.8$ mm/s and the other in the opposite direction at -11.8 mm/s. (Rigorously speaking, the BEC is actually in a quantum superposition of both momentum states. The classical language is only a convenient shorthand). The moving BECs slow down as they climb the axial potential, stopping at the classical turning point at $t = \pi/(2\omega_z)$. For the lowest typical trap frequency used in our experiments, $\omega_z = 2\pi \times 4.2$ Hz, the BECs are separated by 890 μm at this point. The BECs are allowed to continue oscillating in the axial potential for a total of $t = N_{\tau/2} \times \pi/\omega_z$, where $N_{\tau/2} = 1$, 2, or 3. After $N_{\tau/2}$ half-periods, when the condensates are overlapped at the center of the potential, the beamsplitter pulse is applied again.

The second beamsplitter pulse's efficiency in transferring the moving BECs back to the stationary state depends on any relative phase shift $\Delta\phi$ that they acquired during propagation through the trap. The momentum distribution after the second pulse obeys

$$R_c = \frac{|C_0|^2}{|C_0|^2 + |C_+|^2} = \cos^2 \frac{\Delta\phi}{2}, \tag{3.1}$$

where R_c is the fraction of atoms stopped by the pulse. This quantity is considered to be the output of the interferometer. To measure the momentum distribution, we shut the trap off just after the second pulse. The system is allowed to freely evolve for 15 ms, after which atoms in the + momentum state will have physically moved away from the center of the trap [see Fig. 3.2(f)]. An absorption image (directed perpendicular to the guide axis) taken after this free evolution time can clearly distinguish three peaks in the distribution, corresponding to the $p = 0$, $2\hbar k_0$, and $-2\hbar k_0$ states. See Fig. 3.3 for representative results.

A differential phase shift $\Delta\phi$ between the propagating condensates can be intentionally applied by adding a magnetic field gradient $B'(t)$ along the waveguide axis once they are spatially separated. This shift obeys

$$\Delta\phi = \int_0^{N_{\tau/2}\pi/\omega_z} \frac{g_F m_F \mu_{\mathrm{B}} B'(t) \Delta z(t)}{\hbar}\, dt, \tag{3.2}$$

where Δz is the distance between the BECs. This phase shift can be quite large for even small

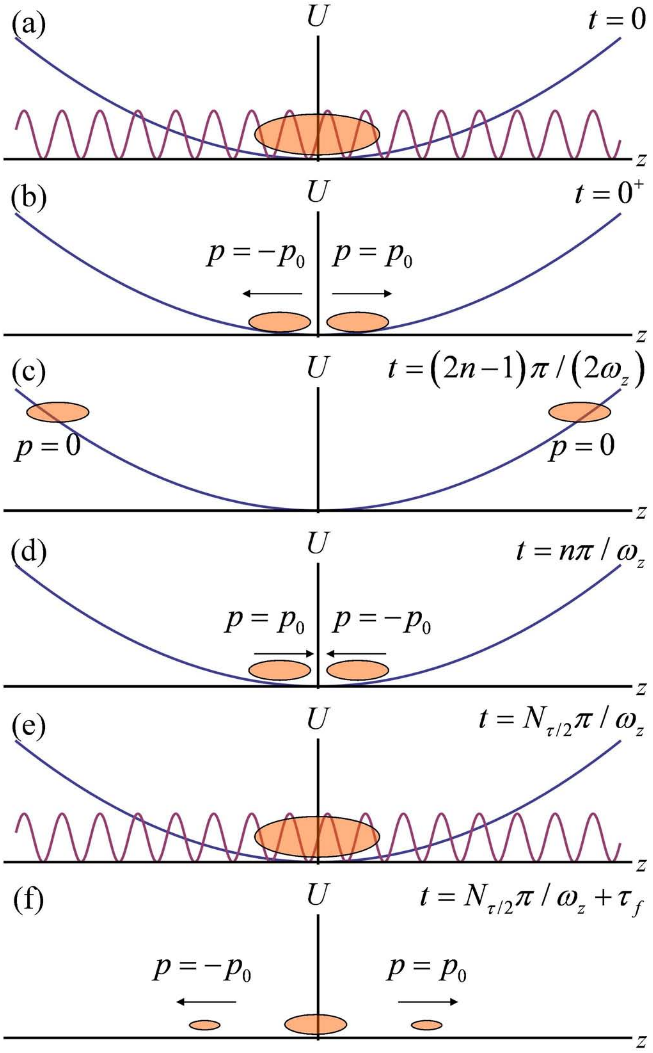

Figure 3.2: (Color). Schematic of Michelson interferometer sequence. (a) Optical grating is applied to stationary condensate in weak axial trap along z (radial potential not shown). (b) BEC splits into momentum states of opposite sign along axis. (c) BECs stop at classical turning points. (d) BECs overlap again at the center after $t = \pi/\omega_z$. (c) and (d) repeat until (e), when the optical grating is applied again, uniting the condensates. (f) The interference pattern is observed by shutting off the trap, allowing the momentum states to move away from each other for time τ_f, and finally recording an absorption image of the atomic density.

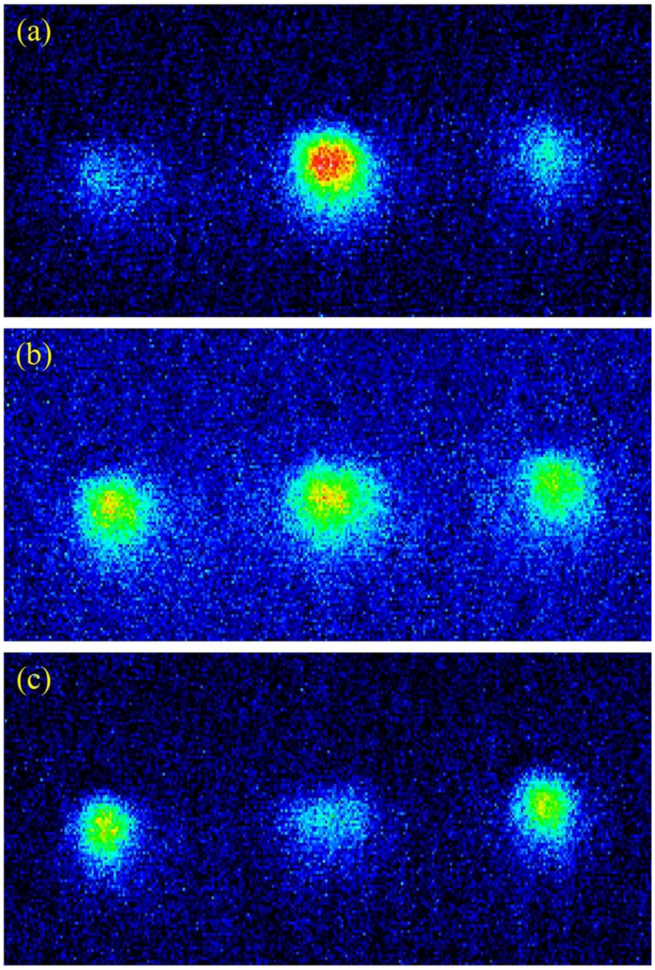

Figure 3.3: (Color). Representative interference patterns from the Michelson experiment. These are false-color absorption images of the atomic density, recorded for various $\Delta\phi$. The central cloud is centered at $p = 0$, the right at $p = 2\hbar k_0$, and the left at $p = -2\hbar k_0$. (a) $\Delta\phi \approx 2\pi m$, (b) $\Delta\phi \approx (2m+1)\pi/2$, (c) $\Delta\phi \approx 2\pi(2m+1)$ for some integer m.

B' when the BECs are at their classical turning points, so the magnetic field gradient must be carefully controlled.

Our BEC interferometer is analogous in configuration to an optical Michelson interferometer, in which a single beamsplitter splits and reunites the optical wave at a static location. There is no static beamsplitter in our interferometer, but the reuniting pulse is applied when the BECs have returned to the their initial positions.

3.2 Apparatus

The microtrap assembly shown in Fig. 3.1 is only 6.5 cm long and 500 mg in mass, but it was just a fraction of the size and weight of the vacuum and optical system needed to support its operation. This section briefly reviews the production of BECs in the apparatus. The goal here is to point out those characteristics that would cause gyroscope experiments to be difficult in this apparatus. For further details, see [16, 25].

The cold atoms used by the Michelson microtrap were prepared away from the chip in a "macrotrap" system (i.e., a system using large coils and permanent magnets to generate magnetic traps). The idea was to use off-the-shelf vacuum hardware and well-understood experimental techniques (see [28, 29]) to prepare the atoms, leaving the experimental uncertainty to the (at the time) novel microtrap. The result was a 1.5 m long, stainless steel vacuum system divided into three chambers (see Fig. 3.4). The chambers could be vented independently, allowing replacement of the microtrap assembly without disturbing the rest of the apparatus.

Condensate production began with the capture of ^{87}Rb atoms in a large pyramid magneto-optical trap (MOT). The single beam was 5 cm in diameter. The quadrupole magnetic field coils were each made from 48 turns of copper tubing, through which water was passed for cooling. After 4–8 s of MOT loading, the MOT was compressed and pumped to the $F = 1$ ground state. The atoms were then loaded into a quadrupole magnetic trap generated by the coils, using a current of 250 A.

Since the MOT chamber's background pressure of untrapped Rb was high enough to

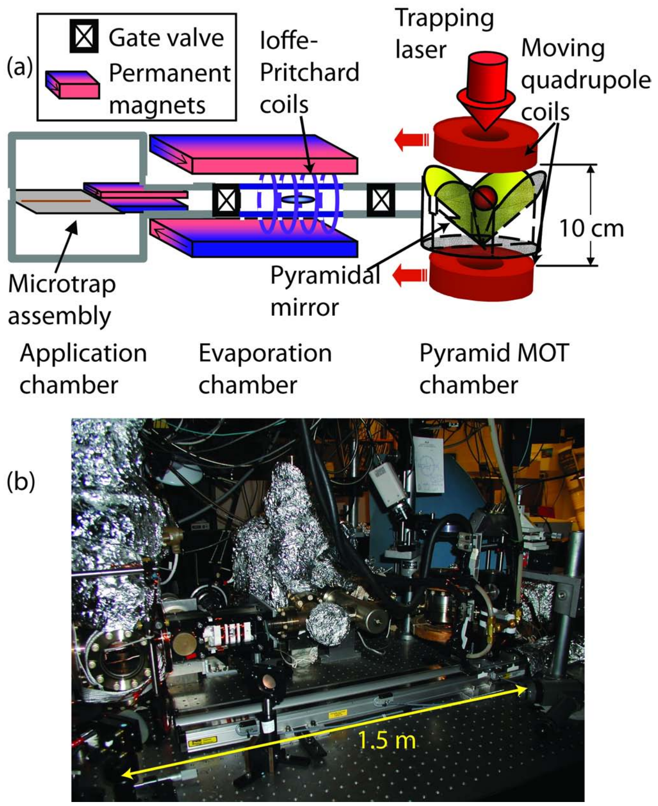

Figure 3.4: (Color). Michelson BEC apparatus (a) schematic [16] and (b) photograph.

inhibit evaporative cooling, the trapped atoms were transported out of the chamber by moving the coils on a servo-controlled track. The coils moved the atoms down a 60 cm long tube in 2 s to a glass cell containing ultrahigh vacuum. The atoms were transferred at this point into a hybrid Ioffe-Pritchard trap generated by a pair of permanent magnetics and a set of coils. This harmonic potential had trap frequencies of $170 \times 170 \times 7$ Hz. The atoms were further cooled by radio-frequency (RF) driven evaporation over the course of approximately 80 s to 1 μK.

The atoms were finally transferred via a hybrid magnetic waveguide from the evaporation cell to the microtrap, which was located in a third vacuum chamber. After further RF evaporation in a tight chip trap, a condensate of 5000-70000 atoms was created. The trap was carefully loosened into the waveguide described above before beginning the interferometry sequence. The entire cycle was about 90 s in duration.

Chapter 4

Data analysis of Michelson interferometry experiments

In the previous chapter, the output of the Michelson interferometer was described as R_c, the fraction of atoms in the momentum state $p = 0$ after the second beamsplitter pulse. The momentum distribution was recorded by taking an absorption image of the atomic density a short time after the pulse. We have not yet detailed how the fraction of atoms was extracted from these images. Our data analysis methods are the topic of this chapter.

4.1 Model-based vs. model-free inference

Fits of images to theory models have typically played the central role in the extraction of measurements from ultracold gas experiments. From one image (or sometimes many images), one typically wishes to extract just a few parameters of interest from the thousands to millions of pixel values. In most experiments, this parameter extraction task is accomplished by fitting the imaged atomic distribution to a model. This model usually is derived from a priori knowledge of the trapping potential and atomic state. The model usually takes into account a period of free expansion of the cloud from the trap that occurs just before the picture is snapped [30]. The experimenter then uses the fit parameters to calculate the results of interest (temperature is calculated from the Gaussian width of a gas in free expansion, for example).

This "fitting" approach to data analysis is an example of model-based inference. It is an appropriate and meaningful approach when the model takes into account the physics at play. The experimenter's a priori knowledge must be reasonably complete and accurate, and the experimental noise must not overwhelm the signal. The utility of model-based inference can rapidly disintegrate if these conditions are not met, since it can fail to extract the proper parameters of interest from data showing an unexpected effect.

The complement of a model-based approach is model-free inference. Model-free analyses use statistical concepts such as maximum likelihood, entropy extremization, and independence to extract the significant features buried in a collection of data. Powerful techniques have emerged over the past three decades and have flourished in fields where analytical models are frequently hard to develop, such as biology, economics, and the social sciences. These techniques are less familiar in physics. For experiments in which a complete model is difficult to develop, model-free inference would allow the data to speak for themselves, free of the interpretive bias of a wrong model.

This chapter presents the application of a closely related pair of model-free analysis techniques to our Michelson data. These two statistical techniques, called principal component analysis (PCA) and independent component analysis (ICA), have been used in image- and signal-processing applications as diverse as human face recognition, brain signal analysis, economic prediction, and astronomical data processing [31, 32, 33, 34]. While our specific focus is on interferometry, a secondary purpose here is to use this experiment to demonstrate the utility and application of these techniques to information extraction from complex ultracold matter images in general. For example, these methods could be of use in the study of complex structures seen in gases containing vortices and gases trapped in optical lattices. We demonstrate here the use of these methods to calibrate our interferometer, to identify and mitigate unforeseen sources of noise, and to uncover signal data that are partially buried in noise. Our statistical methods are able to complete these tasks in a fraction of the time needed for fitting routines to run. This chapter expands on a previous treatment of our use of PCA and ICA [27]; an alternative description is given in [25].

4.2 Model-based image analysis

Before presenting PCA and ICA, we describe the application of traditional fitting methods to extract R_c. In this method, the three peaks in the momentum distribution are fit to Gaussian or Thomas-Fermi distributions [35]. The fraction of atoms in the $p = 0$ peak is calculated from the fit parameters.

This approach has an inherent weakness: There is no simple a priori model for the shape of the momentum distribution of the atoms after the interferometry cycle. The atoms begin the experiment in a pure, stationary BEC with a simple Thomas-Fermi distribution. During the experiment, the propagating BECs move through each other multiple times. With each pass, a fraction of the atoms undergo collisions and are scattered out of the ballistically propagating condensate packets. Some of these ejected atoms remain in the trap for the duration of the experiment and are recorded in the absorption images. These ejected atoms are no longer coherent with the condensate packets, but a three-peak fit is unable to distinguish the “noise” atoms from the coherent atoms. This is just an example of one possible decoherence mechanism that causes an apparent decrease in the interferometry signal’s visibility. Furthermore, our routines have trouble fitting three independent shapes to the image when the space between the peaks contains a significant number of scattered atoms.

Of additional concern, the fitting of three independent two-dimensional shapes to each image in a data set that contains upward of 100 images is computationally intensive. Our fitting implementation takes up to an hour to completely fit such a set of images. The slow speed prevents adjustment of experimental parameters in real time, a shortcoming that would become a serious problem in an apparatus with the rapid BEC production rate needed to take high-bandwidth measurements.

Finally, the peaks themselves are often clearly not well described by the simple Thomas-Fermi distribution (see Fig. 4.1 for an example). As noted in [36], $\Delta\phi$ is expected to be spatially inhomogeneous in experiments of this type because of dephasing effects. Such inhomogeneity causes the three peaks in the momentum distribution to acquire spatial structure. If one attempts to fit a Thomas-Fermi distribution to the results of an experiment in which the interferometer suffers from dephasing, the fit will integrate over the spatial information and suppress the interferometer's contrast. The signal would still be present in the images, but the use of the incorrect model would bury it. Other unidentified symptoms of noise or unexpected physical processes could similarly escape detection if the data were fit by an incomplete model.

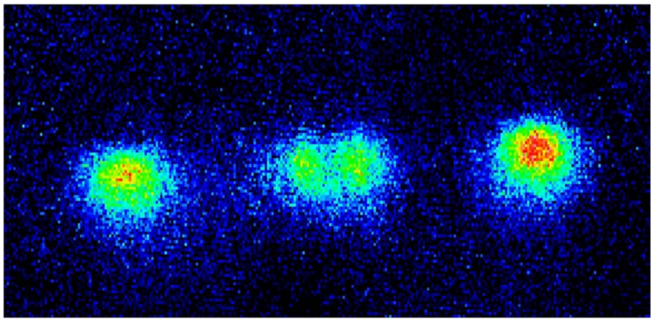

Figure 4.1: (Color). A false-color interferometer result in which spatial dephasing has occurred.

4.3 Statistical image analysis

In place of fitting the images to a model, a statistical method might be used to extract and analyze the significant features. In statistical image analysis, it is useful to represent each pixelated, gray-scale image i as a $\hat{p}$-dimensional vector $\mathbf{X}_i$, where $\hat{p}$ is the number of pixels. The vector's projection along dimension j is equal to the value of pixel j of the image. For a very coarse camera that records only two pixels, a set of (totally independent) images could be plotted as in Fig. 4.2(a). An analysis of a set of images is then carried out by using the statistics of the corresponding set of vectors to find a more useful set of basis vectors $\mathbf{u}_j$ in which to represent the data, such that $\mathbf{X}_i = \mathbf{M} + Y_{1i}\mathbf{u}_1 + Y_{2i}\mathbf{u}_2 + \cdots + Y_{\hat{p}i}\mathbf{u}_{\hat{p}}$; here, $\mathbf{M}$ is the mean image of the set.

To illustrate the inconvenience of the original pixel basis, consider the case of a set of images from our interferometry experiments. Each image contains three spatially localized

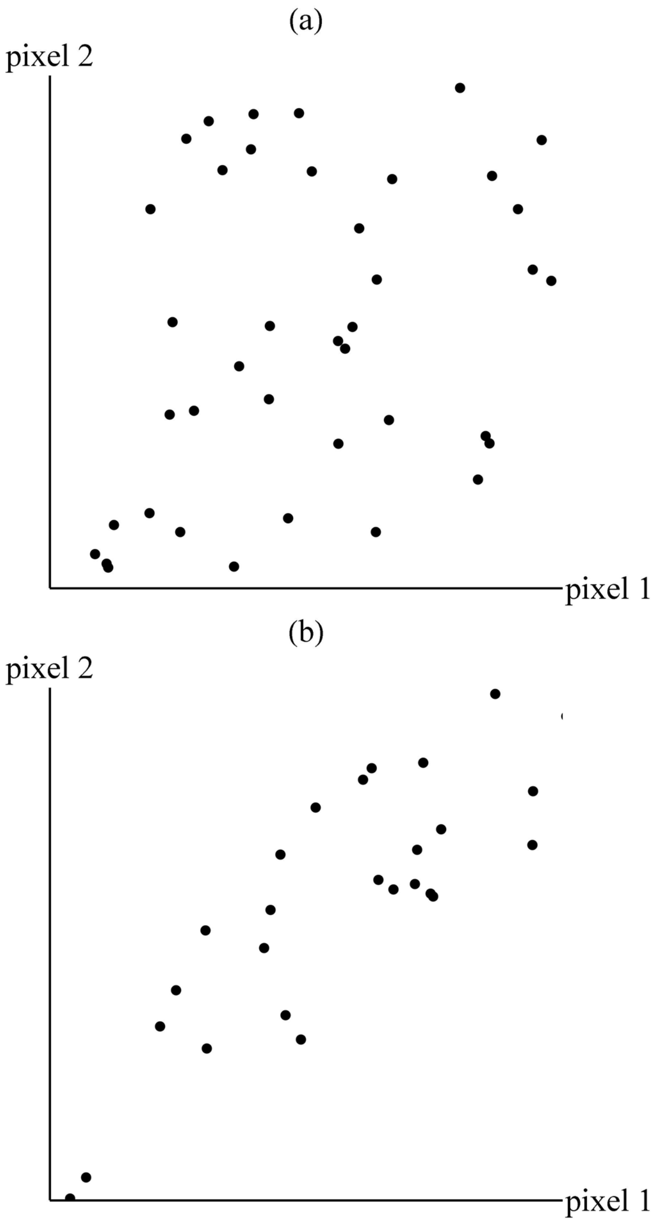

Figure 4.2: Representation of coarse two-pixel images in vector form. (a) A set of independent, unrelated images. (b) A set of images in which the variation of the two pixels is not independent; this could be a set of similar images in which some detail is varied from shot to shot.

features: the peaks in the momentum distribution. Each peak is recorded in the frame by the values of a localized subset of pixels. We know that the relative prominence of the central peak changes as $\Delta\phi$ is varied; this variation is recorded by a change in the value of all of the pixels in the center of the frame. In the vector representation, the components corresponding to those central pixels do not vary independently of each other. A plot of the vector representation of a two-pixel image of just the center of the central peak would look something like Fig. 4.2(b). It is clear that the pixel basis in which we have represented the image vectors is not linearly independent.

The image vectors could instead be represented in a different basis. A natural choice requires each basis vector to consist of a linear combination of pixels that vary independently from any other grouping of pixels, portraying a single image characteristic that varies independently of all other characteristics. The characteristic (which the experimenter can conveniently examine by representing the basis vector itself as an image) is connected to the variation of a parameter of the experiment. In a well-controlled experiment, most of the differences between the images would be quantified by the coefficient of the single basis vector corresponding to the experimentally controlled parameter. The variation of the other coefficients would represent unwanted noise processes. The important information in a data set will be represented by the variation of only the small number of basis vectors corresponding to the experimental signal and the most significant noise sources.

PCA and ICA are both algorithms that try to find this statistically independent basis. The difference between the two, to be detailed in the next section, is that ICA uses a higher order test of independence to find the new basis than PCA uses. An example of a subset of the basis images found by these algorithms for a given data set is shown in Fig. 4.3. (The basis images computed from another data set would appear slightly different). The data image i is equal to the sum of the data set's mean image (the last image in the sum) and a linear combination of the basis images. This example illustrates how straightforward it usually is to assign a physical process to a given basis image by simple visual inspection. We emphasize that this process does involve using a sort of "interpretive" model to assign meaning to the images. To begin, we must find the basis image corresponding to the primary experimental signal, a change in the fraction of atoms found in the central momentum peak. The third basis image in Fig. 4.3 represents precisely that change. An image in which all of the atoms were in the center would have a large, positive value of Y_{3i}, for example. An examination of the other two basis images shows the experimenter the two dominant noise processes recorded in the data: The first corresponds to an overall fluctuation in the number of atoms in the experiment, and the second to a fluctuation in the vertical position of the atoms at the moment of the photograph. The experimenter may use this information to debug and reduce the experimental noise. The complete basis contains another $N_{\mathrm{I}} - 3$ basis images (where N_{I} is the number of images in the set). In this example, their coefficients varied only slightly from image to image. These images represent detection noise which can be ignored. Details on the selection of which basis images convey important information may be found in Sec. 4.4.2.

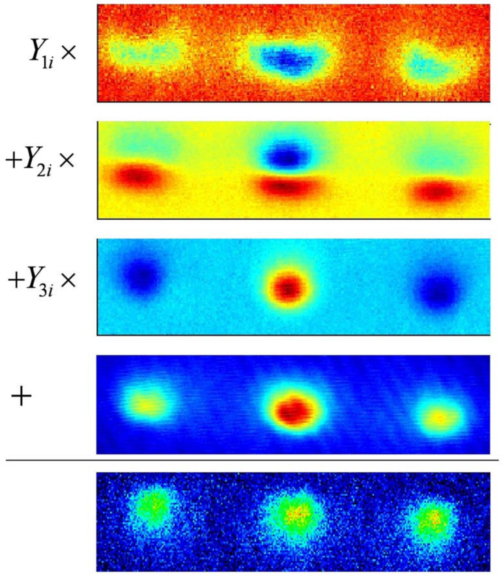

Figure 4.3: (Color). An example showing how an image i from the interferometry experiment may be represented as a linear combination of independent basis images, each representing a single physical parameter in the experiment, plus the mean image of the set. False color is used to represent pixel value in all images. Varying Y_{1i} changes the overall number of atoms; varying Y_{2i} changes the overall vertical position of the three peaks; varying Y_{3i} changes R_c).

The process of recovering the signal is now straightforward. The coefficient Y_{3i} is proportional to the fractional population that was previously extracted by fitting the images:

$$Y_{3i} = A\cos\Delta\phi = A(2R_c - 1) \tag{4.1}$$

The coefficient Y_{3i} now constitutes the primary measurement of the state of the interferometer in any given attempt. The phase $\Delta\phi$ (modulo 2π), amplitude A, and estimates of the visibility of the fringes may be extracted by fitting a set of Y_{3i} values to $Y_{3i} = A\cos\Delta\phi$ or to the expected statistical distribution based on that equation. This procedure does require fits to a model, but the fits are applied to the output of the image analysis process rather than to the raw images themselves. The distinction is analogous to the difference between using a model to explain the dependence of experimental parameters on an independent variable and using Gaussian fits in the first place to extract those parameters from a set of raw images. Parameter extraction of this type will be detailed in Sec. 4.5.

Figure 4.4 shows the result of carrying out PCA on a typical data set of over 100 images, while Fig. 4.5 shows the result of ICA carried out on the same images. We observe that the higher order test used in ICA does a better job of isolating R_c than the lower order test of PCA does; the second principal component in Fig. 4.5 looks most like it describes the signal, but it is clear that varying the third principal component will slightly change R_c as well. On the other hand, the third independent component in Fig. 4.5 is the only one of the three that encodes the variation of R_c that we seek.

4.4 Details of algorithms

In this section we will detail the PCA and ICA algorithms. We begin by discussing the distinction between the two. Recall that the goal is to represent an image $\mathbf{X}_i$ as a linear combination of a set of basis images: $\mathbf{X}_i = \mathbf{M} + Y_{1i}\mathbf{u}_1 + Y_{2i}\mathbf{u}_2 + \cdots + Y_{pi}\mathbf{u}_{\hat{p}}$. The basis images calculated by PCA are an orthonormal set. For a set of N_{I} image vectors represented in this principal component (PC) basis, the set of coefficients of any one basis image j is required to

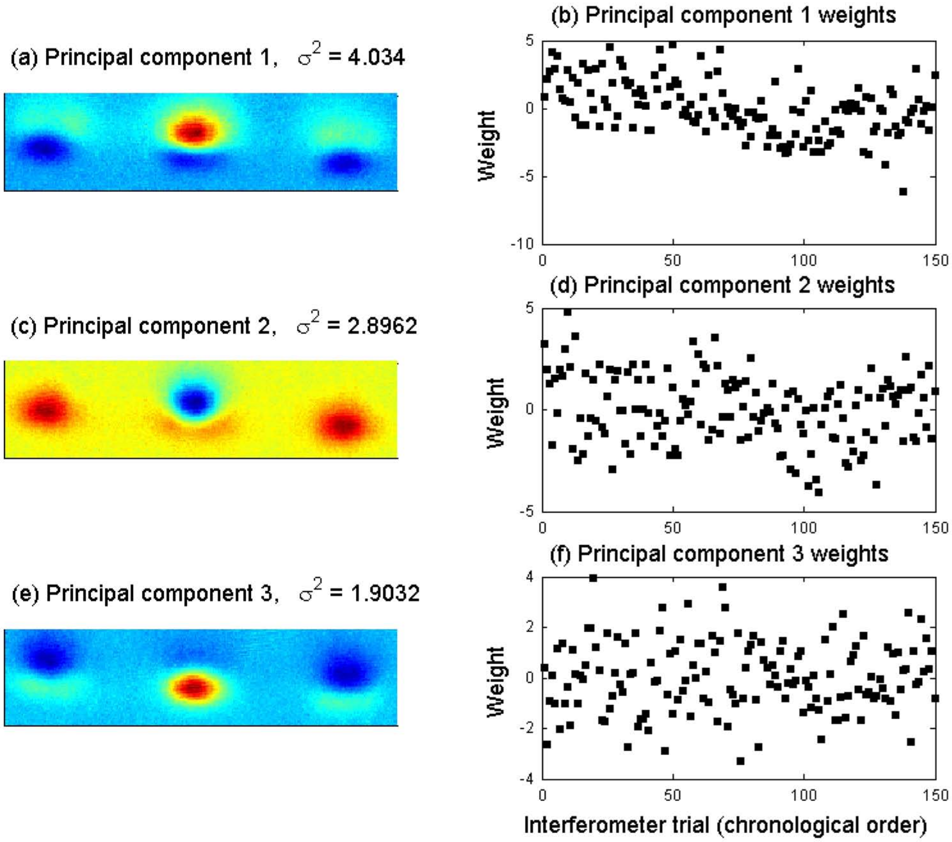

Figure 4.4: (Color). Results of PCA of a typical interferometry data set. The three principal component basis images (PCs) shown in false color account for most of the total pixel variance (σ^2) in the data set. The experimental signal $R_c = \cos^2(\Delta\phi/2)$ can be related to PC 2, but it is clear that some of it is mixed into PC 3.

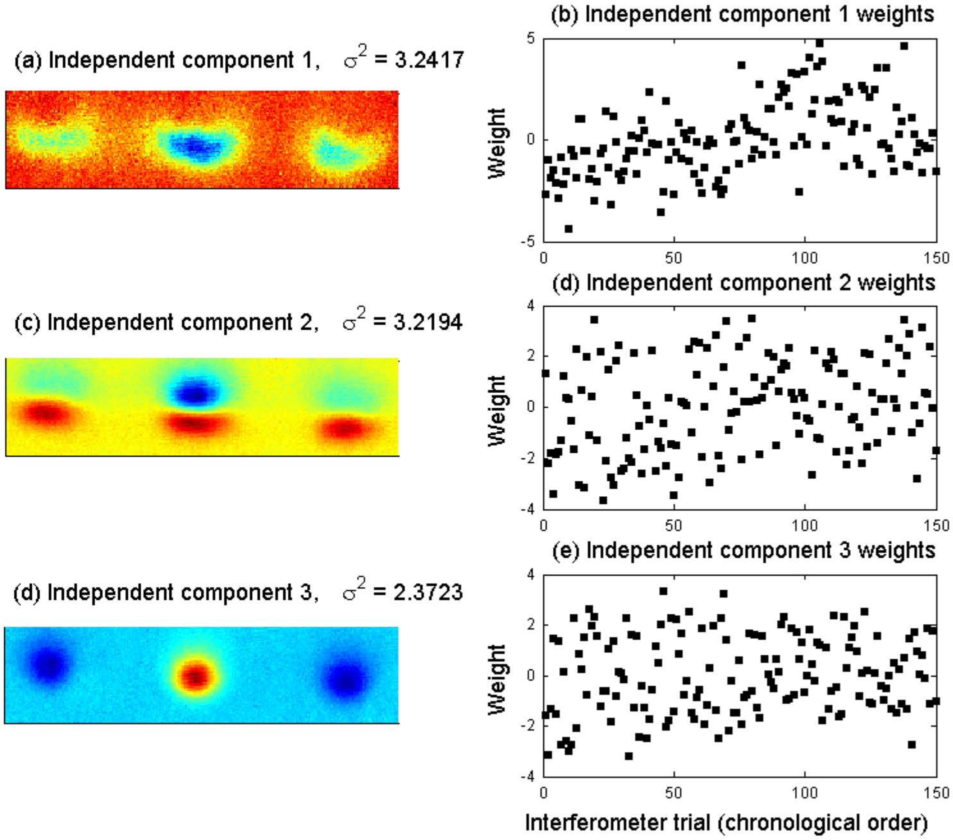

Figure 4.5: (Color). False-color results of ICA of the same data set used in Fig. 4.4. Independent component basis image IC 3 is clearly the experimental signal; it is not mixed into the other two ICs.

be statistically uncorrelated with the set of coefficients of any other basis image k:

$$\sigma_{jk}^2 = \frac{1}{N_{\mathrm{I}} - 1} \sum_{i=1}^{N_{\mathrm{I}}} Y_{ji}^{(P)} Y_{ki}^{(P)} = 0. \tag{4.2}$$

In this equation, $Y_{ji}^{(P)}$ is the coefficient of the PC basis image j in the representation of image i. In contrast, ICA applies a considerably stronger test to the statistics of the coefficients; the basis it calculates is, however, not necessarily orthogonal. The coefficients of the independent component (IC) basis are statistically independent, obeying

$$\frac{1}{N_{\mathrm{I}}} \sum_{i=1}^{N_{\mathrm{I}}} g\left(Y_{ji}^{(I)}\right) h\left(Y_{ki}^{(I)}\right) - \frac{1}{N_{\mathrm{I}}^2} \left(\sum_{i=1}^{N_{\mathrm{I}}} g\left(Y_{ji}^{(I)}\right)\right) \left(\sum_{i=1}^{N_{\mathrm{I}}} h\left(Y_{ki}^{(I)}\right)\right) = 0. \tag{4.3}$$

Here, $Y_{ji}^{(I)}$ is the coefficient of the IC basis image j in the representation of image i, and g and h are any integrable functions. Two coefficients that are independent are necessarily also uncorrelated, since the definition of decorrelation can be recovered by setting $g(x) = h(x) = x$ (as long as the mean value of each coefficient is zero). Independence can therefore be thought of as a higher order decorrelation.

One might conclude from the preceding paragraph that ICA, with its use of higher order statistics, is always the more useful technique. It is indeed more reliable at the task of extracting the experimental signal. There exists a class of tasks, however, for which PCA remains the method of choice. Recall that for any set of vectors represented in two different orthonormal bases, the sum of the variances of the coefficients in basis 1 must be equal to the sum of the variances of the coefficients in basis 2. This rule applies to the image analysis problem as well, such that all of the image-to-image variation is preserved intact in the PC basis. Since the overall variance is conserved, the variance of a given PC coefficient can be used to rank how much of the overall variation in the data is accounted for by that PC. This ranking is essential in the calibration of the experiment, described in the next chapter. In contrast, the IC basis is not orthogonal. The total variance of the coefficients of the IC basis images is not equal to the total variance of the original pixels. For this reason, the IC basis images cannot be easily ranked by their variance.

4.4.1 Principal component analysis

Having explained the difference between the two algorithms, we describe the details of the calculations. PCA is a textbook application of linear algebra [37], so the first step in the process is to represent a set of images in matrix form. Consider a set of N_{I} images of $\hat{p}$ pixels each. The pixel values of each image i are written as the components of a vector $\mathbf{X}_i$. If the mean image, defined as

$$\mathbf{M} = \frac{1}{N_{\mathrm{I}}}(\mathbf{X}_1 + \ldots + \mathbf{X}_{N_{\mathrm{I}}}), \tag{4.4}$$

is subtracted from each image, a $\hat{p} \times N_{\mathrm{I}}$ matrix of the images in mean-deviation form can be constructed:

$$\begin{aligned} \hat{X} &= (\mathbf{X}_1 - \mathbf{M} \quad \mathbf{X}_2 - \mathbf{M} \quad \cdots \quad \mathbf{X}_{N_{\mathrm{I}}} - \mathbf{M}) \\ &= (\hat{\mathbf{X}}_1 \quad \hat{\mathbf{X}}_2 \quad \cdots \quad \hat{\mathbf{X}}_{N_{\mathrm{I}}}). \end{aligned} \tag{4.5}$$

The $\hat{p} \times \hat{p}$ sample covariance matrix of the image set is calculated from $\hat{X}$:

$$S = \frac{1}{N_{\mathrm{I}} - 1}\hat{X}\hat{X}^T. \tag{4.6}$$

The diagonal element S_{jj} is the sample variance of pixel j:

$$S_{jj} = \sigma_{jj}^2 = \frac{1}{N_{\mathrm{I}} - 1}\sum_{i=1}^{N_{\mathrm{I}}} \hat{X}_{ji}^2, \tag{4.7}$$

and the total variance of all the pixels is $\mathrm{tr}(S)$. The off-diagonal element S_{jk} is the covariance of pixels j and k:

$$S_{jk} = \sigma_{jk}^2 = \frac{1}{N_{\mathrm{I}} - 1}\sum_{i=1}^{N_{\mathrm{I}}} \hat{X}_{ji}\hat{X}_{ki}. \tag{4.8}$$

If $\sigma_{jk}^2 = 0$, then pixels j and k are uncorrelated.

PCA uses the covariance matrix to calculate a new basis for the images. Each column i of $\hat{X}$ (representing one image $\hat{\mathbf{X}}_i$) is a linear combination of the original pixel basis vectors:

$$\hat{\mathbf{X}}_i = \hat{X}_{1i}\begin{pmatrix} 1 \\ 0 \\ \vdots \\ 0 \end{pmatrix} + \hat{X}_{2i}\begin{pmatrix} 0 \\ 1 \\ \vdots \\ 0 \end{pmatrix} + \ldots \hat{X}_{N_{\mathrm{I}}\, i}\begin{pmatrix} 0 \\ 0 \\ \vdots \\ 1 \end{pmatrix}. \tag{4.9}$$

In the PCA basis, the image is represented as a linear combination of a new orthonormal set of N_{I} vectors/images:

$$\hat{\mathbf{X}}_i = Y_{1i}^{(P)}\mathbf{u}_1^{(P)} + Y_{2i}^{(P)}\mathbf{u}_2^{(P)} + \ldots + Y_{N_{\mathrm{I}}\,i}^{(P)}\mathbf{u}_{N_{\mathrm{I}}}^{(P)}. \tag{4.10}$$

We assume here that $N_{\mathrm{I}} < \hat{p}$, a reasonable assumption for high-resolution digital images. These PC basis images can be written as a $\hat{p}\times N_{\mathrm{I}}$ orthonormal matrix $P^{(P)} = (\mathbf{u}_1^{(P)} \quad \mathbf{u}_2^{(P)} \quad \cdots \quad \mathbf{u}_{\hat{p}}^{(P)})$. The two representations of the data set are related by

$$\hat{X} = P^{(P)}Y^{(P)}. \tag{4.11}$$

Here and in Eq. (4.10), the matrix $Y^{(P)}$ is an $N_{\mathrm{I}} \times N_{\mathrm{I}}$ matrix in which column i is the set of coefficients (or weights) of image i in the PC basis.

The requirement that the set of coefficients of any PC be uncorrelated with the set of coefficients of any other PC is met if and only if the sample covariance matrix of the PC basis,

$$D = \frac{1}{N_{\mathrm{I}}-1} Y^{(P)} \left(Y^{(P)}\right)^T, \tag{4.12}$$

is diagonal. By using Eqs. (4.6) and (4.11), along with the orthonormality of P, D may be rewritten as

$$\begin{aligned} D &= \frac{1}{N_{\mathrm{I}}-1} \left(P^{(P)}\right)^T \hat{X}\hat{X}^T P^{(P)} \\ &= \left(P^{(P)}\right)^T S P^{(P)}. \end{aligned} \tag{4.13}$$

The sample covariance matrices are related by

$$S = P^{(P)} D \left(P^{(P)}\right)^T. \tag{4.14}$$

If D is diagonal, then the PCs are the unit eigenvectors of S. The eigenvalue of a PC is the variance of its coefficient. It is often referred to as the “strength” of the PC.

4.4.2 Reduction of dimensionality with PCA

It only remains to show explicitly how to reconstruct an image using the PC basis. Assume the PCs have been sorted in order of decreasing strength. Then image i is written in the new basis as

$$\mathbf{X}_i = \mathbf{M} + Y_{1i}^{(P)}\mathbf{u}_1^{(P)} + Y_{2i}^{(P)}\mathbf{u}_2^{(P)} + \ldots + Y_{N_\mathrm{I}\,i}^{(P)}\mathbf{u}_{N_\mathrm{I}}^{(P)}. \tag{4.15}$$

In the analysis of a set of similar images, most of the variance will be captured by the first q PCs, where q is the smallest eigenvalue of S above some cutoff value. As a result, the most important features of image i can still be reconstructed if the image is represented only as

$$\mathbf{X}_i \approx \mathbf{M} + Y_{1i}^{(P)}\mathbf{u}_1^{(P)} + Y_{2i}^{(P)}\mathbf{u}_2^{(P)} + \ldots + Y_{qi}^{(P)}\mathbf{u}_q^{(P)}. \tag{4.16}$$

The dimensionality of each image is thereby reduced from $\hat{p}$ pixels to q PC weights. If each of these q strongest PCs can be positively identified with the variation of a specific experimental parameter, then its weight in an image is proportional to the value of the associated parameter in that experimental trial.

The choice of how many PCs to retain is often a difficult one. A detailed analysis of rules that are often applied to make that choice is found in [38]. The method that we have found to be most useful is the scree graph, a plot of σ_j^2 (the variance of PC j, when sorted in decreasing order) vs. j. We show the scree plot for a particular data set in Fig. 4.6. This data set was the second of two sets of 100 trials obtained on 14 January 2008, so we will refer to it for the rest of the chapter as 0114b. The scree graph is used to identify the PC q at which the plot's "elbow" occurs. This is defined as the first PC beyond which the plot defines a straight line. If there is more than one straight line defined by the smaller PCs, then the elbow is taken to be the first PC on the first of those lines. For the 0114b set, the elbow is located at the fifth PC.

The scree plot method is somewhat subjective, but in our experience it produces reliable results. Figure 4.7 shows the six strongest PCs for the 0114b data set. We see visually that the first five images primarily encode changes in the recorded momentum distribution. On the other hand, a dominant feature of the sixth image is a set of diagonal lines caused by diffraction in the probe laser beam. The decision to discard this PC made using the scree graph therefore seems quite sensible.

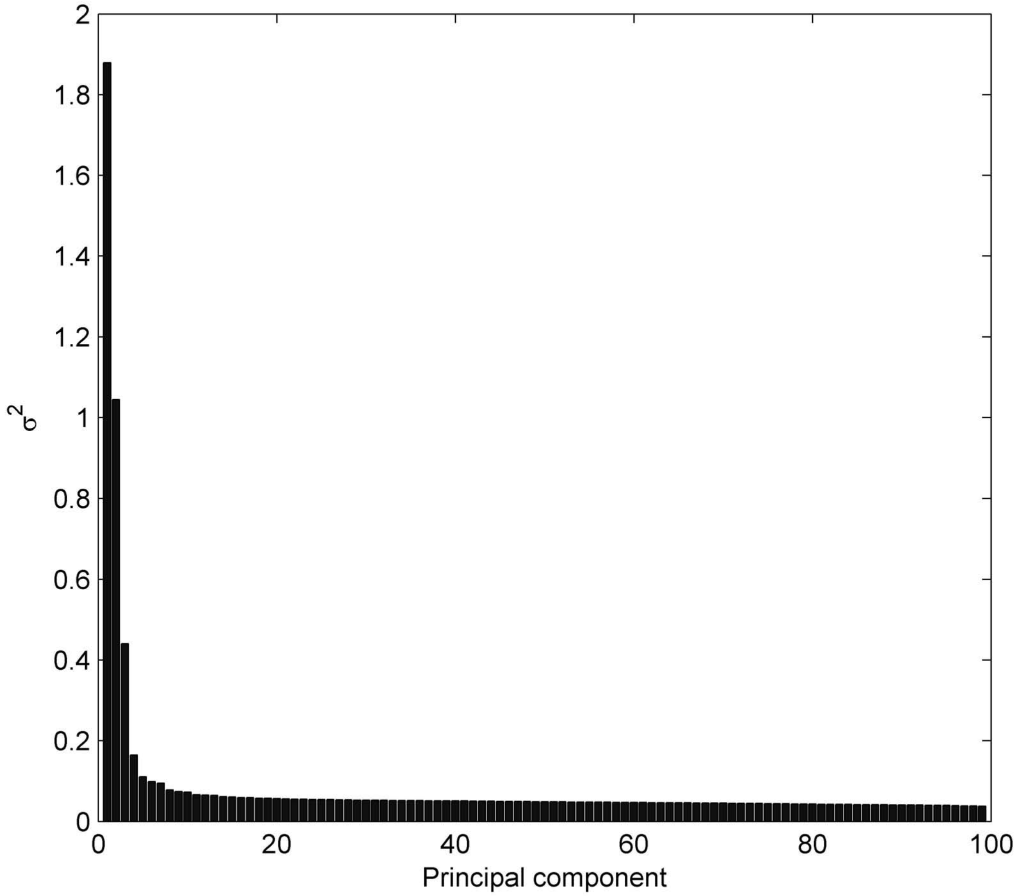

Figure 4.6: Scree plot for 0114b data set. Elbow occurs at PC 5.

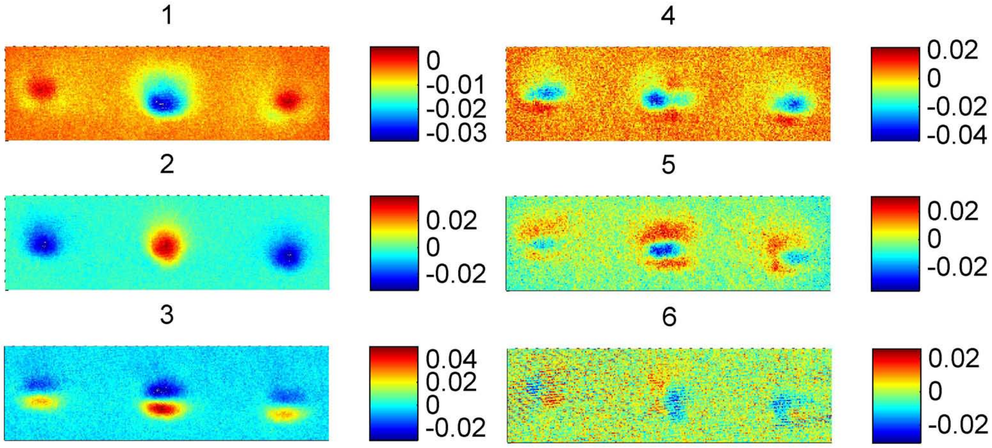

Figure 4.7: (Color). Strongest PCs of 0114b data set, organized in order of decreasing variance.

4.4.3 Independent component analysis

In both this data set and the set shown in Fig. 4.4, the signal R_c appears to be encoded by two PCs. ICA is needed to isolate the signal for sets of this type. The statistically independent representation of $\hat{X}$ found by ICA [39, 40] is given by

$$\hat{X} = P^{(I)} Y^{(I)}, \tag{4.17}$$

where $P^{(I)} = (\mathbf{u}_1^{(I)} \quad \mathbf{u}_2^{(I)} \quad \ldots \quad \mathbf{u}_{N_\mathrm{I}}^{(I)})$ is the matrix of ICs and $Y^{(I)}$ is the new matrix of coefficients. The challenge is to find $P^{(I)}$ and $Y^{(I)}$ such that Eq. (4.3) is satisfied.

ICA is more effective than PCA only if the underlying experimental parameters are not normally distributed, because ICA uses tests on the higher order statistical moments of the coefficients to determine independence. Since these are all zero for a normal distribution, PCA has already produced a statistically independent set; ICA can do no better.

Fortunately, our experimental signal is not expected to be normally distributed when $\Delta\phi$ is a random variable with a uniform distribution. The noticeably not normal probability density of $A\cos\Delta\phi$ [see Eq. (4.1)] for a uniformly distributed $\Delta\phi$ with zero mean and range much greater than π is shown in Fig. 4.8(a). ICA should therefore (at least for some data sets) find a better representation of the signal than PCA. The results of the analysis of the 0114b data back up this statement, as the shape of the histogram of the set of coefficients for the interference signal IC [see Fig. 4.8(d)] resembles that of the expected probability density. (This comparison is purely qualitative). On the other hand, the histograms of PC coefficients [Fig. 4.8(b) and (c)] do not resemble the shape of Fig. 4.8(a) at all. The deviations of Fig. 4.8(d) from the ideal can be accounted for by the finite size of the data set and the addition of normally distributed detection noise. See Sec. 4.5 for more details, including a method for extracting the probability density's amplitude A from the data. Note that it is not a hard rule that ICA's basis image for the signal is always better than PCA's; we have seen data sets for which the two are nearly identical.

The relation of higher order moments to the independence of variables is given by the

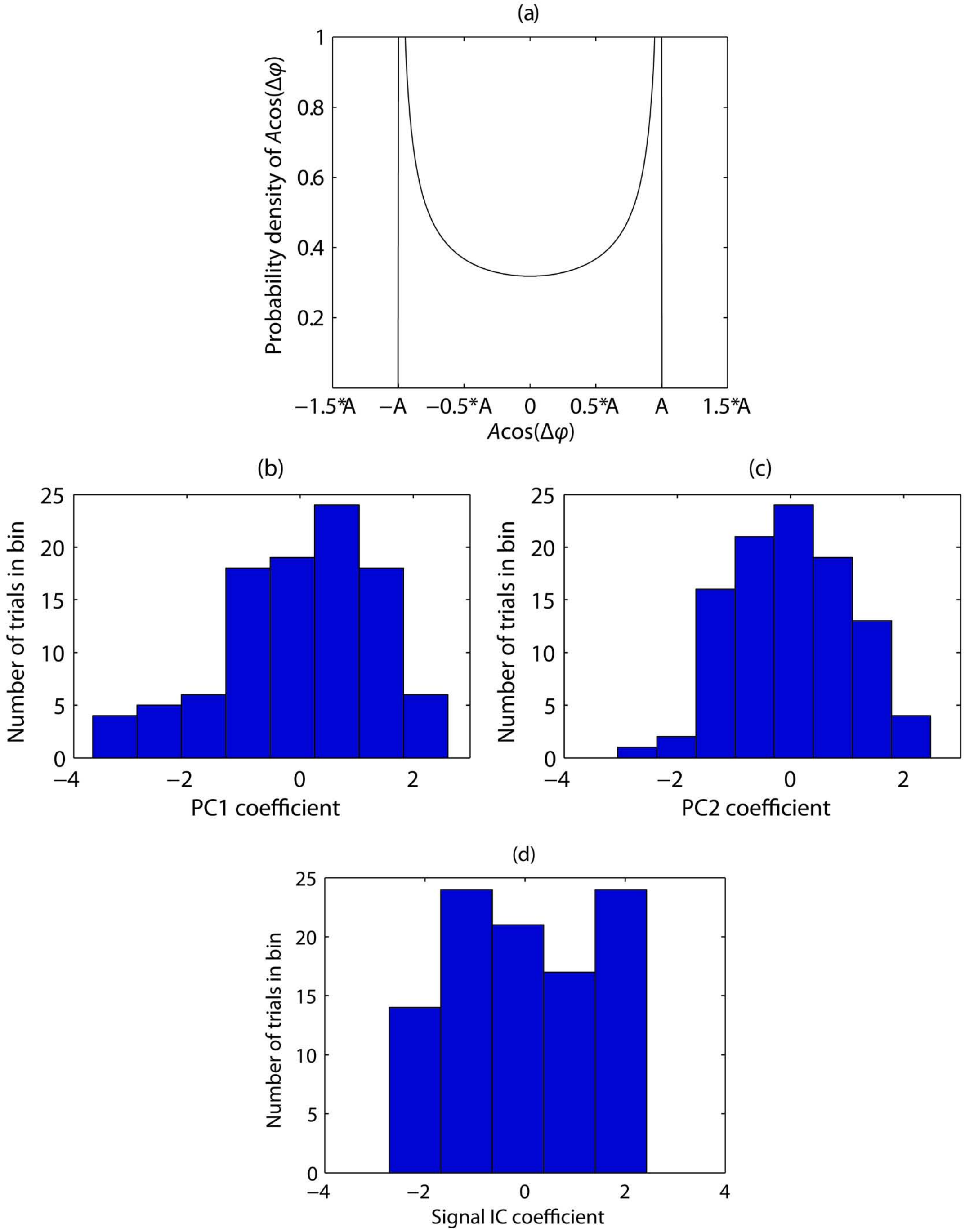

Figure 4.8: (Color). (a) The non-Gaussian ideal probability density of $A \cos \Delta\phi$ for uniform distribution of $\Delta\phi$. (b) and (c) From 0114b data, the Gaussian-like histograms of the coefficients of the PCs imperfectly representing the interference signal. (d) For the same data set, the clearly non-Gaussian histogram of the coefficient of the signal IC.

central limit theorem. This states that the sum of two independent variables has a probability density that resembles a Gaussian at least as well as either of the densities of the independent variables themselves. A corollary is that the density of an independent variable is “less Gaussian” than the density of the sum of the variable and any other variable. Therefore, an ICA algorithm maximizes the “non-Gaussianity” of the density of the calculated IC’s coefficients. Many possible measurements of non-Gaussianity exist; one of the simplest is the normalized kurtosis excess, defined as

$$\gamma_2 = \frac{\mu_4}{\sigma^4} - 3. \tag{4.18}$$

In this expression, σ^4 is the square of the variance of a variable, and μ_4 is its fourth moment. Kurtosis excess measures the “peakedness” of the variable’s density; a variable for which $\gamma_2 > 0$ has a density more highly peaked than a Gaussian of the same variance and vice versa. A number of more elaborate measures of non-Gaussianity exist, but all depend in some way on calculating the higher order moments of the distributions of the coefficients.

ICA begins with a calculation of the PC basis of a set of images. It is next assumed that each PC is actually a linear combination of the underlying ICs (which are therefore not orthogonal). The algorithm then forms an initial guess at the ICs by filling the columns of $P^{(I)}$ with N_I random, linearly independent linear combinations of the PCs. The coefficient matrix of the guess is calculated by inverting $P^{(I)}$:

$$Y^{(I)} = \left(P^{(I)}\right)^{-1} \hat{X}. \tag{4.19}$$

A test of non-Gaussianity (perhaps kurtosis) is then applied to each row of $Y^{(I)}$. An optimization routine is used to adjust the guess of $P^{(I)}$, and the process is repeated until the coefficients of the optimized ICs are sufficiently non-Gaussian.

4.5 Parameter extraction from PCA/ICA results

In the previous section, it was mentioned that the constant of proportionality A between the signal-related PC or IC and the real experimental result R_c could be determined by fitting a data set's signal coefficients to its expected statistical distribution. That fitting procedure is the subject of this section.

4.5.1 Model for probability density of PC/IC signal

We begin by assuming that the phase shift $\Delta\phi$ has the probability density [Fig. 4.9(a)]:

$$f_{\Delta\phi}(\Delta\phi) = \begin{cases} 1/(2\pi) & \text{if } |\Delta\phi| \leq \pi \\ \\ 0 & \text{if } |\Delta\phi| > \pi \end{cases} . \tag{4.20}$$

This is a reasonable assumption for experiments in which $\Delta\phi$ is uniformly varied over a range much broader than $[-\pi, \pi]$, as our experimental output measures $\Delta\phi$ modulo 2π. Recall Eq. (4.1), relating the PCA/ICA coefficient y to $\Delta\phi$:

$$y = A \cos \Delta\phi. \tag{4.21}$$

The probability density of y is [41]

$$\begin{aligned} f_y(y) &= \sum_i \frac{f_{\Delta\phi}(\Delta\phi_i)}{y'(\Delta\phi_i)} \\ &= \frac{1}{\sqrt{A^2 - y^2}} \sum_i f_{\Delta\phi}(\Delta\phi_i), \end{aligned} \tag{4.22}$$

where each $\Delta\phi_i$ is a root of Eq. (4.21). For any given value of y, there are two values of $\Delta\phi$ in the range $[-\pi, \pi]$ that satisfy Eq. (4.21). We retain those two terms, obtaining

$$f_y(y) = \begin{cases} 1/(\pi\sqrt{A^2 - y^2}) & \text{if } |y| < A \\ \\ 0 & \text{if } |y| \geq A \end{cases} \tag{4.23}$$

[see Fig. 4.9(b)]. Recall Fig. 4.8, in which we saw that the histogram of a typical data set has tails outside of the peaks predicted by Eq. (4.23). We may include these tails in the model by assuming that the PC/IC coefficient measures normally-distributed detection noise along with the signal. We will call this convoluted measurement

$$z = y + x, \tag{4.24}$$

where x has the probability density [Fig. 4.9(c)]

$$f_x(x) = \frac{1}{\sigma\sqrt{2\pi}} e^{-x^2/2\sigma^2}. \tag{4.25}$$

The probability density of a sum of two random variables is [Fig. 4.9(d)]:

$$\begin{aligned}
f_z(z) &= \int_{-\infty}^{\infty} f_x(z-y) f_y(y)\, dy \\
&= \frac{1}{\sigma\sqrt{2\pi}} \int_{-A}^{A} \frac{1}{\pi\sqrt{A^2-y^2}} \exp\left(\frac{-(z-y)^2}{2\sigma^2}\right)\, dy \\
&= \frac{-1}{\sigma\pi\sqrt{2\pi}} \int_{-\pi}^{0} \frac{\sin\Delta\phi}{\sqrt{1-\cos^2\Delta\phi}} \exp\left(\frac{-(z-A\cos\Delta\phi)^2}{2\sigma^2}\right)\, d\Delta\phi \\
&= \frac{1}{\sigma\pi\sqrt{2\pi}} \int_{-\pi}^{0} \exp\left(\frac{-(z-A\cos\Delta\phi)^2}{2\sigma^2}\right)\, d\Delta\phi.
\end{aligned} \tag{4.26}$$

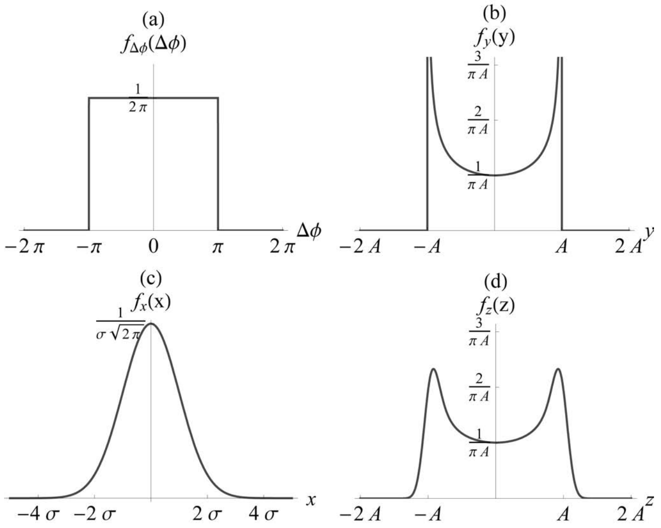

Figure 4.9: Plots of various probability densities. (a) $f_{\Delta\phi}(\Delta\phi)$, (b) $f_y(y)$, (c) $f_x(x)$, (d) $f_z(z)$.

4.5.2 Maximum likelihood estimation of parameters

Our goal now is to extract the values of the proportionality parameter A and noise parameter σ from a given data set. A common method for fitting a probability density like Eq. (4.26) to a set of observations is maximum likelihood estimation (MLE) [42]. Consider the joint probability density of a set of observations $\mathbf{z}$ and our unknown parameters:

$$f(\mathbf{z};\ A,\ \sigma). \tag{4.27}$$

If we insert an observed set of sample values for $\mathbf{z}$, then Eq. (4.27) becomes the likelihood function of the two unknown parameters. The likelihood can be thought of as the complement of the joint probability density, in which the observed data and the parameters have exchanged roles. The maximum likelihood estimators of the parameters, $\hat{A}$ and $\hat{\sigma}$, are those choices that maximize the likelihood for a given set of observations $\mathbf{z} = (z_1,\ z_2,\ \ldots,\ z_{N_\mathrm{I}})$. In our case, the likelihood is

$$f_L(\mathbf{z};\ A,\ \sigma) = \left(\frac{1}{\sigma\pi\sqrt{2\pi}}\right)^{N}_{\mathrm{I}} \prod_{i=1}^{N_\mathrm{I}} \left[\int_{-\pi}^{0} \exp\left(\frac{-(z_i - A\cos\Delta\phi)^2}{2\sigma^2}\right)\, d\Delta\phi\right]. \tag{4.28}$$

For ease of calculation, MLE typically maximizes the natural logarithm of the likelihood:

$$\ln f_L = -N_\mathrm{I}\ln(\sigma\pi\sqrt{2\pi}) + \sum_{i=1}^{N_\mathrm{I}} \ln\left[\int_{-\pi}^{0} \exp\left(\frac{-(z_i - A\cos\Delta\phi)^2}{2\sigma^2}\right)\, d\Delta\phi\right]. \tag{4.29}$$

The result for the 0114b data set is

$$\begin{aligned} A &= 1.83 \\ \sigma &= .40. \end{aligned} \tag{4.30}$$

This fit is shown superimposed on a normalized histogram of the data in Fig. 4.10. The fit is not perfect, as the data set is of finite size. We can obtain confidence regions for the fit by making a contour plot of the likelihood (normalized to 1) around the fit value (Fig. 4.11). The plot shows that the likelihood is approximately a two-dimensional Gaussian. We wish to find the contours that enclose 50%, 68%, and 95% of the area of the Gaussian, which are equivalent to the 50%, 68%, and 95% confidence regions for the parameters. The circular coverage function [43]

$$p_c\left(\frac{r_d}{s}\right) = \frac{1}{2\pi s^2}\int\int_{x^2+y^2\le r_d^2} \exp\left(\frac{-(x^2+y^2)}{2s^2}\right)\, dx\ dy \tag{4.31}$$

can be used to find the radius of the circular Gaussian that encloses the desired area fraction. This radius is then inserted back into the Gaussian to find the value of the function at that radius, and therefore the desired contour (this contour is the same for our elliptical case). These contours we seek are located at 0.52, 0.3, and 0.05 respectively, and are marked on the figure.

The individual parameter 68% confidence regions [44] are

$$A = 1.83\ (1.68,\ 1.97)$$
$$\sigma = 0.40\ (0.31,\ 0.54), \tag{4.32}$$

shown by dashed lines in Fig. 4.11. More accurate confidence region estimates could be made by numerically integrating the normalized likelihood, but this would be computationally intensive. The estimate method given here can be carried out rapidly. Note that this method of parameter extraction is generally applicable to all data sets; we have only used the 0114b set as an example.

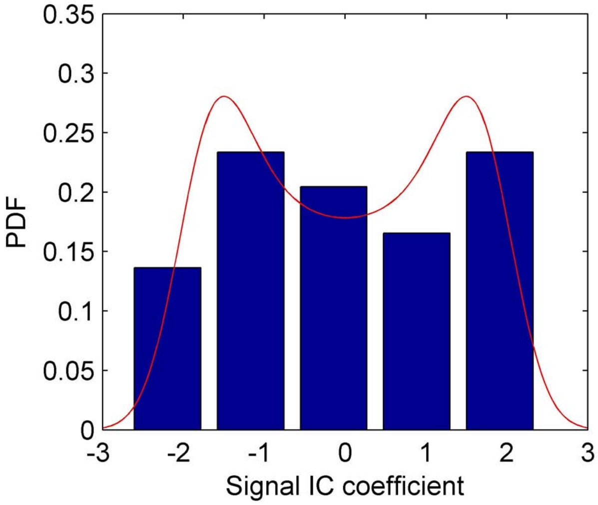

Figure 4.10: (Color). Result of MLE of probability density function (PDF) superimposed on normalized histogram of 0114b data set. We see that the MLE of the scaling parameter A qualitatively fits the data.

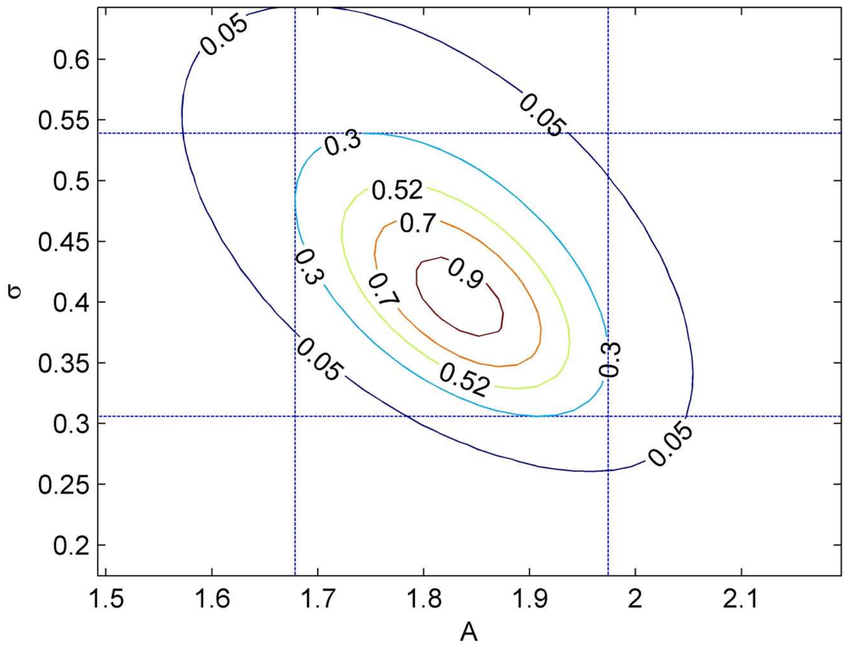

Figure 4.11: (Color). Plot of normalized likelihood near fit values for 0114b data set. The 0.3 contour is approximately the 68% confidence region for the two parameters. Individual parameter confidence regions are given by the projection of the ellipse onto the axes, shown here as blue dashed lines.

Chapter 5

Results and lessons learned from Michelson interferometry

In this chapter, we use the output of PCA and ICA to extract the results of the free-return Michelson experiment. We determine that the interferometer phase was randomized by a combination of apparatus vibrations and quantum phase diffusion. Experimental modifications to minimize these two factors would have been difficult to carry out in the Michelson apparatus, leading us towards the design and construction of a new apparatus.

5.1 Michelson calibration and results

Before beginning a long run of the experiment, we used PCA to calibrate the apparatus. The timing of the second optical pulse is a critical experimental parameter. For the BECs to be maximally overlapped at the moment of the second pulse, the separation in time between the two pulses must be a multiple (or one-half of a multiple) of the trap period. However, the period can slowly drift by hundreds of microseconds. The problem is compounded by the 90 s cycle time of the apparatus; a data set of 100 attempts represents more than 2 h of accumulated drift. To recalibrate before taking a set, we vary this parameter around the expected value and perform ten attempts of the interferometry cycle at each value. The attempts carried out at a given pulse time are done with widely varying values of $\Delta\phi$ (applied with a magnetic field gradient) to ensure high interference contrast from shot to shot. We then carry out PCA separately on each small set of images taken at one particular pulse time. At the pulse time that results in the highest interference contrast, the variance of the coefficient of the basis image corresponding to the phase shift signal will be maximized. Figure 5.1 shows the result of a typical calibration run; a value of zero variance has been assigned for recombination times at which PCA did not produce a basis image that could be positively identified with the interference signal. Since PCA is computationally fast, a plot like Fig. 5.1 can be generated as quickly as the data are taken.

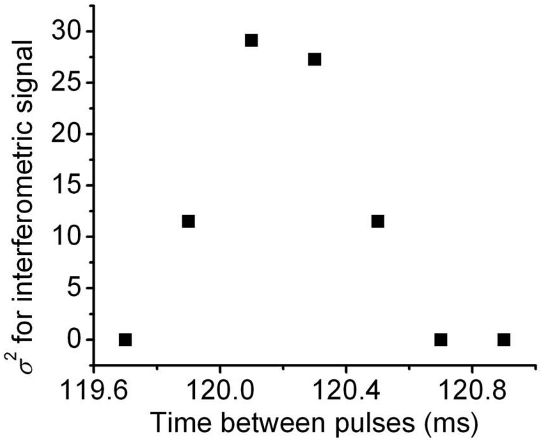

Figure 5.1: Plot of the variance of the coefficient of the basis image representing the interference signal vs time between optical pulses; a value of zero variance is used to indicate times at which the interference signal cannot be identified with a single basis image.

A data run containing more than 100 interferometry experiments began immediately after calibration was complete. Figure 4.5 presents a typical result of our interferometry work, taken after a full trap period (240 ms, in this experiment) of propagation time. The visibility of the interference pattern

$$V = \frac{R_c^{\max} - R_c^{\min}}{R_c^{\max} + R_c^{\min}} \tag{5.1}$$

as obtained with Gaussian fits was fairly good, at about 50%. Of more concern for the future development of instruments was that the phase of the interfereometer was not controllable. In the remainder of this section, we will outline two factors that work together to randomize the phase, and must be mitigated in future experiments. This outline is based on the full analysis of the experiment found in a previous dissertation [25].

5.1.1 Vibrations of the apparatus

The first randomizing effect that we will consider is the coupling of apparatus vibrations to the differential phase. As we will see, this noise coupling mechanism can be dealt with by better isolating the experiment from environmental mechanical noise and an adjustment of experimental parameters.

Recall from Eq. (2.34) that the BECs that are propagating in the trap acquire a phase shift from their transfer into non-zero momentum states by the initial beamsplitter pulse. That phase term is $\exp[\pm 2k_0 z(0)]$, where we will take the positive sign to be for the condensate propagating along the $+z$ direction. Here, $z(0)$ is the distance between the retro-reflecting mirror and the initial location of the BEC. The second pulse imprints a phase opposite in magnitude in its attempt to stop the atoms, multiplying the wavefunctions by $\exp[\mp 2k_0 z(T)]$ [$z(T)$ is the distance between the mirror and the two overlapped BECs at the moment of reunion]. The end result is a differential phase shift between the two BECs equal to

$$\Delta\phi_{\text{laser}} = 4k_0(z(0) - z(T)). \tag{5.2}$$

In the ideal experiment $z(0) = z(T)$, so this laser-induced differential phase shift vanishes.

In real experiments, $z(T)$ is not necessarily equal to $z(0)$. A vibration of the apparatus directed along the guide axis modifies the equation of motion of the moving BECs to include a driving acceleration $a(t)$:

$$\ddot{z} + \omega_z z = a(t). \tag{5.3}$$

The general solution (obtained by variation of parameters [45]) is

$$z(t) = A_1 \cos\omega_z t + A_2 \sin\omega_z t + \frac{\sin\omega_z t}{\omega_z}\int_0^t a(t')\cos(\omega_z t')\, dt' - \frac{\cos\omega_z t}{\omega_z}\int_0^t a(t')\sin(\omega_z t')\, dt'. \tag{5.4}$$

The shift in phase at the end of one axial period ($t = T = 2\pi/\omega_z$) due to the acceleration is therefore

$$\Delta\phi_{\text{laser}} = -\frac{4k_0}{\omega_z}\int_0^T a(t')\sin(\omega_z t')\, dt'. \tag{5.5}$$

Vibration of the apparatus can be generally expressed as

$$a(t) = a(\omega_v)\sin(\omega_v t + \phi_v) \tag{5.6}$$

for any given frequency ω_v, amplitude $a(\omega_v)$, and initial phase ϕ_v. The phase shift for that vibration is

$$\begin{aligned}\Delta\phi_{\text{laser}} =& \frac{2k_0}{\pi(1+\omega_v/\omega_z)} T^2 a(\omega_v) \text{sinc}\left[\pi\left(\frac{\omega_v}{\omega_z} - 1\right)\right] \\ &\times \left\{\sin\phi_v \sin\left[\pi\left(\frac{\omega_v}{\omega_z} - 1\right)\right] - \cos\phi_v \cos\left[\pi\left(\frac{\omega_v}{\omega_z} - 1\right)\right]\right\}.\end{aligned} \tag{5.7}$$

The sum in quadrature of both in- and out-of-phase vibrations is shown in Fig. 5.2. We see that low-frequency vibrations near the axial trap frequency can significantly shift the output of the interferometer, with the greatest shift

$$\Delta\phi_{\text{laser}}(\max) = -\frac{k_0 T^2 a(\omega_v)}{\pi} \tag{5.8}$$

occurring for in-phase vibrations at ω_z. For our typical axial trap of $\omega_z = 2\pi \times 4.2$ Hz, $\Delta\phi_{\text{laser}}(\max) = \pi$ for $a(\omega_v) = 2.2 \times 10^{-5}$ m/s^2.

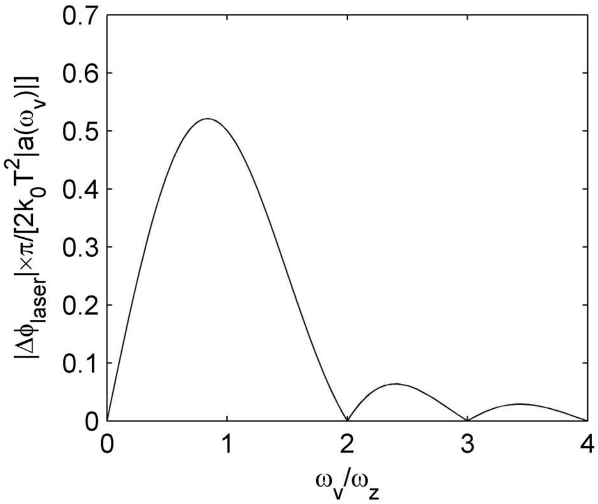

Figure 5.2: Quadrature sum of differential phase shifts caused by in-phase and out-of-phase vibrations vs vibration frequency.

To determine if the vibrations were having a noticeable effect on the experiment, we carefully measured the spectrum of the vibrations of our optical table along the guide axis using a seismometer. Two results are shown in Fig. 5.3: in (a) the table is resting on its supports, in (b) it is floating on its pneumatic isolators. The plots indicate that vibration-induced phase randomization should be significant at $\omega_z = 2\pi \times 4.2$ Hz, though it should be less of a problem when the table is floating.

The experimental results support that hypothesis. Data sets taken with the table resting on its supports have the characteristic double-peaked probability density of large phase variation even when the phase is not intentionally varied. In contrast, consider Fig. 5.4, which shows the histogram of the signal IC from a data set taken while the table was floating. Instead of the familiar shape of Sec. 4.5, we see a density that appears to be missing one of its wings. This plot is a qualitative indication that the spread in phase has been reduced.

While the mitigation of vibration effects by floating the table is encouraging, we still do not have sufficient control over the differential phase for stable interferometry. An effort was made to precisely measure the vibrations of the apparatus during the experiment using the already mentioned seismometer, and thereby calculate the expected vibration phase shift. There was no correlation between this calculated shift and the output of the interferometer. Among the proposed technical problems with the procedure is that the structure holding the microtrap module is not perfectly rigid (see Fig. 5.5), so the vibrations measured by the seismometer could not have been perfectly correlated with the actual mirror vibrations.

5.1.2 Quantum phase diffusion

Technical problems notwithstanding, a more fundamental effect is expected to cause phase randomization. Quantum phase diffusion offers a compelling explanation for the failure to correlate the measured vibrations with the interferometer output. The source of this phase diffusion is the energy of the interactions of the atoms in each BEC. This energy is parameterized by the chemical potential μ, a function of the number of atoms in the BEC. The wavefunctions of the two condensates (identified here as "$j = +$" and "$j = -$") of our experiment each include a phase evolution term $\exp[i\mu_j(N_j)t/\hbar]$ due to this energy. The fundamental quantum

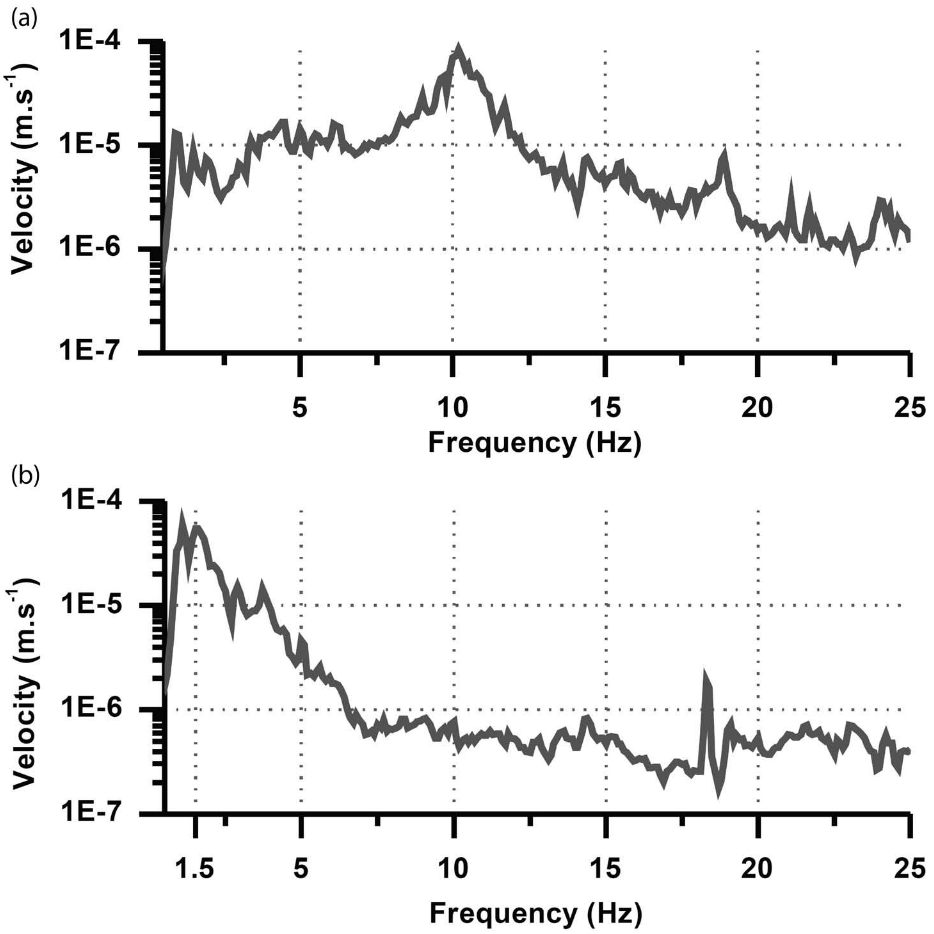

Figure 5.3: Spectra of optical table vibrations along guide axis. (a) Table is resting on legs, (b) table is floating on isolators [25].

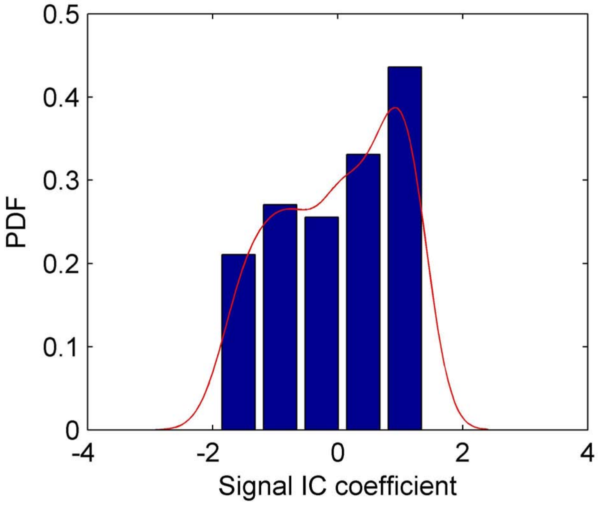

Figure 5.4: (Color). Normalized histogram of signal IC from data set taken with table floating and without any intentional phase variation, superimposed with a kernel smoothing estimate of the probability density function (PDF). See Sec. 4.5 for details on extracting the proportionality constant A that relates the signal IC coefficient to $\cos \Delta\phi$.

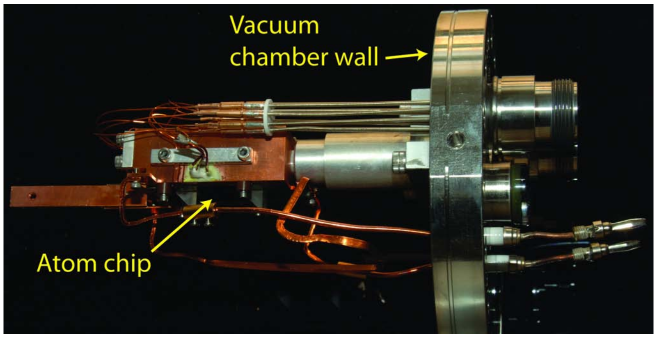

Figure 5.5: (Color). Microtrap module from Michelson apparatus. The atom chip is suspended from a cantilevered arm projecting from the wall of the vacuum chamber. This cantilever is not expected to be perfectly rigid.

uncertainty of the number of atoms in the two condensates causes the relative phase to develop its own uncertainty. The initially well-known differential phase is said to "diffuse" over time [30]. We follow the treatment of [46] to estimate the diffusion rate.

We first calculate the uncertainty in the splitting process. Consider a trapped BEC containing N_T atoms that is adiabatically split into two physically separated wells. Our case of momentum-state splitting is analogous, as long as the duration of the splitting process itself (during which the two BECs interact with each other) is much shorter than the total duration of the experiment. Immediately after splitting, the wavefunction of each individual atom i is a coherent superposition of two opposite momentum states: $[\psi_+(\mathbf{r}_i) + \psi_-(\mathbf{r}_i)]/\sqrt{2}$. We use the Hartree approach to find the total many-body wavefunction

$$\begin{aligned}\Psi(\mathbf{r}_i, \ldots, \mathbf{r}_{N_T}, t=0) &= \frac{1}{2^{N_T/2}} \prod_{i=1}^{N_T} [\psi_+(\mathbf{r}_i) + \psi_-(\mathbf{r}_i)] \\ &= \frac{1}{2^{N_T/2}} \sum_{k=0}^{N_T} \sqrt{\begin{pmatrix} N_T \\ N_- \end{pmatrix}} \chi_{N_-, N_T-N_-}(\mathbf{r}_i, \ldots, \mathbf{r}_{N_T}), \end{aligned} \tag{5.9}$$

where we have used the binomial coefficient in the summation. The unit-normalized wavefunction for the state in which N_- atoms are in the $-$ BEC and $N_T - N_-$ atoms are in the $+$ BEC is χ_{N_-, N_T-N_-}. The corresponding state vector is

$$|\Psi(t=0)\rangle = \frac{1}{2^{N_T/2}} \sum_{N_-=0}^{N_T} \sqrt{\begin{pmatrix} N_T \\ N_- \end{pmatrix}} |N_-, N_T - N_-\rangle . \tag{5.10}$$

We see that for large, even N_T that the most likely measured result of N_- is $N_- = N_T/2$, with approximate uncertainty $\sqrt{N_T}$. For the rest of these calculations, we will continue to assume N_T is even; the end result for odd N_T is the same, though the derivation is slightly different.

To calculate the evolution of the state, we will need to estimate the energy of the system. Near $N_- = N_T/2$, the most probable value of N_-, the energy of a given number state is

$$\begin{aligned}E_-(N_-) + E_+(N_T - N_-) &\approx 2E\left(N_- = \frac{N_T}{2}\right) + \frac{d^2E(N_- = N_T/2)}{dN_-^2}\left(N_- - \frac{N_T}{2}\right)^2 \\ &\approx \hbar\left(\omega_{N_T/2} + \xi(N_- - N_T/2)^2\right). \end{aligned} \tag{5.11}$$

The state at time t is therefore

$$|\Psi(t)\rangle = \frac{\exp(-i\omega_{N_T/2}t)}{2^{N_T/2}} \sum_{N_-=0}^{N_T} \sqrt{\begin{pmatrix} N_T \\ N_- \end{pmatrix}} \exp\left(-i\xi t(N_- - N_T/2)^2\right) |N_-, N_T - N_-\rangle \,. \tag{5.12}$$

We see that the phase for each value of N_- evolves at a different rate.

We find the probability of measuring a specific phase difference $\Delta\phi$ by computing

$$P(\Delta\phi_{\check{p}}) = |\langle\Delta\phi_{\check{p}}|\Psi(t)\rangle|^2, \tag{5.13}$$

where $|\Delta\phi_{\check{p}}\rangle$ is an eigenstate of the phase-difference operator. These states are [47]:

$$|\Delta\phi_{\check{p}}\rangle = \frac{1}{\sqrt{N_T+1}} \sum_{N_-=0}^{N_T} \exp\left(iN_-\Delta\phi_{\check{p}}\right) |N_-, N_T - N_-\rangle \,, \tag{5.14}$$

for eigenvalues $\Delta\phi_{\check{p}} = 2\pi\check{p}/(N_T+1)$, $\check{p} = -N_T/2, -N_T/2+1, \ldots, N_T/2$. The inner product of the states is

$$\langle\Delta\phi_{\check{p}}|\Psi(t)\rangle = \frac{\exp(-i\omega_{N_T/2}t)}{2^{N_T/2}\sqrt{N_T+1}} \sum_{N_-=0}^{N_T} \sqrt{\begin{pmatrix} N_T \\ N_- \end{pmatrix}} \exp\left[-i\left(\xi t\left(N_- - \frac{N_T}{2}\right)^2 + N_-\Delta\phi_{\check{p}}\right)\right]. \tag{5.15}$$

In the limit $N_T \gg 1$, the binomial coefficient can be replaced with a Gaussian:

$$\begin{pmatrix} N_T \\ N_- \end{pmatrix} \approx \frac{2^{N_T+1}}{\sqrt{2\pi N_T}} \exp\left(\frac{-2(N_- - N_T/2)^2}{N_T}\right). \tag{5.16}$$

It is also appropriate to approximate the sum by an integral, obtaining

$$\begin{aligned}\langle\Delta\phi_{\check{p}}|\Psi(t)\rangle = {} & \frac{\exp(-i\omega_{N_T/2}t)}{2^{N_T/2}\sqrt{N_T+1}} \left(\frac{2^{N_T+1}}{\sqrt{2\pi N_T}}\right)^{1/2} \\ & \times \int_0^{N_T} dN_- \exp\left[-i\left(\xi t\left(N_- - \frac{N_T}{2}\right)^2 + N_-\Delta\phi_{\check{p}}\right) - \frac{(N_- - N_T/2)^2}{N_T}\right].\end{aligned} \tag{5.17}$$

As $N_T \to \infty$,

$$\begin{aligned}\langle\Delta\phi_{\check{p}}|\Psi(t)\rangle = {} & \frac{\exp(-i\omega_{N_T/2}t)\sqrt{\pi}}{2^{N_T/2}\sqrt{N_T+1}} \left(\frac{2^{N_T+1}}{\sqrt{2\pi N_T}}\right)^{1/2} \\ & \times \frac{1}{\sqrt{i\xi t + 1/N_T}} \exp\left[\frac{-iN_T\Delta\phi_{\check{p}}}{2} - \frac{\Delta\phi_{\check{p}}^2}{4(i\xi t + 1/N_T)}\right].\end{aligned} \tag{5.18}$$

Multiplying Eq. (5.18) by its complex conjugate, we obtain

$$P(\Delta\phi_{\check{p}}) = \frac{1}{N_T+1}\frac{\sqrt{2\pi}}{\sigma_{\Delta\phi}}\exp\left(-\frac{\Delta\phi_{\check{p}}^2}{2\sigma_{\Delta\phi}^2}\right), \tag{5.19}$$

with standard deviation

$$\sigma_{\Delta\phi} = \sqrt{\frac{1}{N_T} + N_T\xi^2 t^2}. \tag{5.20}$$

The probability density for $\Delta\phi$ is obtained by the transformation

$$f(\Delta\phi)\; d\Delta\phi = P(\Delta\phi_{\check{p}}), \tag{5.21}$$

where $d\Delta\phi = 2\pi/(N_T+1)$. The result is

$$f(\Delta\phi) = \frac{1}{\sqrt{2\pi}\sigma_{\Delta\phi}}\exp\left(-\frac{\Delta\phi^2}{2\sigma_{\Delta\phi}^2}\right), \tag{5.22}$$

where we now consider $\Delta\phi$ to be a continuous variable. Note that the equivalent equation in [46] seems to have been printed with the incorrect normalization. Regardless, the key result is that the standard deviation of the differential phase increases approximately linearly at rate $R = \sqrt{N}\xi$.

We can easily calculate R for a BEC in the Thomas-Fermi limit. The total energy of such a condensate is [35]

$$E = \frac{5}{14}\left(\frac{15N_- a_s}{\bar{a}}\right)^{2/5}\hbar\bar{\omega}N_-, \tag{5.23}$$

where N_- is the number of atoms, a_s is the scattering length, $\bar{\omega}$ is the geometric mean trapping frequency, and $\bar{a}$ is the corresponding oscillator length. Using the definition of ξ in Eq. (5.11), we find

$$\begin{aligned} R &= \left(\frac{72}{125}\right)^{1/5}\left(\frac{a_s}{\bar{a}}\right)^{2/5}\frac{\bar{\omega}}{N_T^{1/10}} \\ &\propto \omega_\rho^{4/5}. \end{aligned} \tag{5.24}$$

For our typical experimental parameters ($N_T = 5000$ ^{87}Rb atoms in $|1,-1\rangle$ ground state, $\omega_\rho = 2\pi \times 80$ Hz, $\omega_z = 2\pi \times 4.2$ Hz), the standard deviation of the phase is 1.6 rad. Note that R is a very weak function of the total number of atoms, but that it scales relatively strongly with respect to the radial trap frequency.

This model is fairly simplistic. It assumes that the splitting is adiabatic and that the BEC is in the Thomas-Fermi limit. It also does not describe the effects (if any) of the recombination process on the phase diffusion rate. Finally, it contains no calculation of the possible effects of phase diffusion on the visibility of the interference signal. This model's results should therefore not be assumed to apply to our experiment without further support. Numerical modeling provides a piece of corroborating evidence. A simulation of the Gross-Pitaevskii equation using our experimental parameters found a number for $\sigma_{\Delta\phi}$ very similar to the analytic result (see [25] for details). The single-peak experimental result of Fig. 5.4 provides some further support. Recall that in this set, no phase shift was intentionally applied and vibrations were significantly reduced by floating the optical table on air. Our contention is that the remaining randomization of the phase is explained by quantum diffusion. To check that, we simulate a 100 point data set in which $\Delta\phi$ is a normally distributed random variable with zero mean and $\sigma_{\Delta\phi} = 1.6$ rad. Figure 5.6 shows the probability density of $\cos\Delta\phi$ for one simulated set. The shape resembles that of Fig. 5.4. Note that the assumption that the mean value of $\Delta\phi$ is 0 is not rigorously supported; the value is not actually known a priori due to the phase randomization. In the end, we can make no strong conclusions although we see some indications that phase diffusion is present in the experiment. Future interferometry work will have to further explore this issue.

5.2 Lessons for future experiments

For any future experiments to be successful, we will have to find some way to address the effect of random vibrations. It should be possible to subtract the phase shift due to vibration from our signal by independently measuring the vibration of the apparatus. Since our previous efforts towards this goal were not successful (see Sec. 5.1.1 and [25]), it is perhaps safer to focus our next efforts on better isolating the experiment from mechanical noise. Operating the axial trap at a higher frequency might help to reduce the amplitude of vibrations transmitted to the mirror, as well as reducing the expected phase shift from the vibrations. The higher trap frequency would give less time for quantum phase diffusion to develop as well. However, as

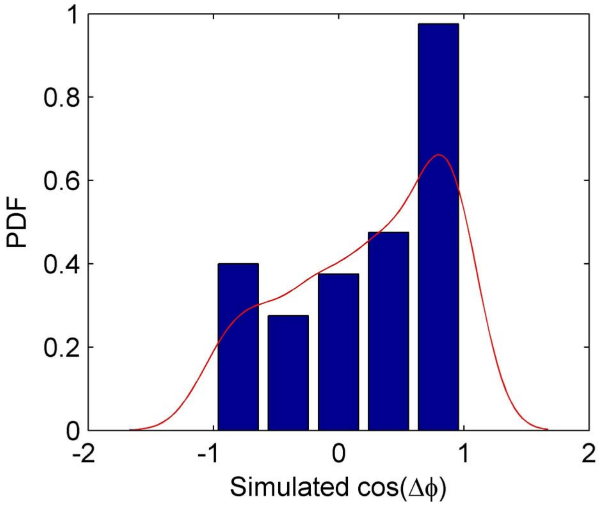

Figure 5.6: (Color). Probability density of simulated data set subject to quantum phase diffusion. We show both a histogram and a kernel smoothing approximation of the PDF (to guide the eye only).

described in Sec. 2.1.2, an increase in the axial confinement leads to an increased tilt of the waveguide with respect to the permanently positioned standing wave mirror. Further increasing that relative tilt would have caused the propagating BECs to oscillate along the radial axis of the guide, reducing the overlap of the two at the application of the second set of beamsplitter pulses. Correcting this problem would have required a redesign of the microtrap assembly or of its surrounding vacuum chamber.

Further investigation of the possible effects of phase diffusion must also be on the agenda. One simple experiment would be to attempt to adjust the phase diffusion rate R. We saw in Eq. (5.24) that $R \propto \omega_\rho^{4/5}$, so a small decrease in the radial confinement would reduce phase diffusion effects. However, as we will see in Sec. 6.5.5, the area enclosed by our proposed gyroscope scales quite strongly with ω_ρ. Future experiments will therefore require a careful selection of an optimal value for ω_ρ.

Another possible way to mitigate the effects of phase diffusion would be obtain more data from the experiment. Assume we have increased the axial frequency to $\omega_z = 2\pi \times 10$ Hz but maintained the same radial frequency. The estimated standard deviation of the phase (using the simple model of the previous section) for this axial frequency is 1 rad; better than before, but still quite large. In Fig. 5.7, we show the results of a simulation of this experiment, in which $\Delta\phi$ is intentionally varied uniformly in the range $[-\pi, \pi]$. The measured output of the experiment is $\cos(\Delta\phi + \phi_D)$, where ϕ_D is a normally distributed phase diffusion contribution with zero mean. On the left side of the figure, we show results for $\sigma_{\Delta\phi} = 1.6$ rad and data sets containing 100, 1000, and 10000 experiments. On the right side, we show results for $\sigma_{\Delta\phi} = 1.6$ rad. Figure 5.7(a), which shows a simulation of the Michelson experimental conditions, shows quite clearly that our data sets that contain 100 points and $\sigma_{\Delta\phi} = 1.6$ rad will never be useful for extracting the phase of the experiment. With more data, the sine wave becomes visible against the noise. A fit to the function $a_1 \cos(\omega_1 \Delta\phi)$ becomes plausible. The fit parameter ω_1 should be 1, and the amplitude a_1 is a fair measure of the visibility of the signal over the noise. The results of these fits are shown in Table 5.1. We see that with $\sigma_{\Delta\phi} = 1$ rad, the fit becomes reliable at 1000 data points. The fit is also twice as visible on the background as it is for the $\sigma_{\Delta\phi} = 1.6$ rad case.

$\sigma_{\Delta\phi}$ (rad)	Number of trials	a_1	ω_1
1.6	100	N/A	N/A
1.6	1000	0.3 [0.1,0.6]	0.8 [0.3,1.3]
1.6	10000	0.30 [0.27,0.34]	0.9 [0.8,1.0]
1.0	100	0.7 [0.4,0.9]	1.0 [0.6,1.4]
1.0	1000	0.60 [0.54,0.65]	1.04 [0.95,1.13]
1.0	10000	0.61 [0.59,0.63]	0.99 [0.96,1.03]

Table 5.1: Fit parameters for simulated data in Fig. 5.7. 95% confidence regions for fit parameters are shown in brackets.

We conclude that we need three apparatus improvements in order to be ready for gyroscope experiments: (1) We need a way to adjust the angle of the standing wave with respect to the chip wires so that higher axial trap frequencies can be used. (2) We need to decrease the time required to make a BEC. A 1000-run data set would take more than a day to obtain with the existing 90 s cycle time. (3) We need to develop a way to rotate the experiment in order to carry out gyroscope tests. Improvement (1) could probably have been made by a modification of the existing apparatus. Improvements (2) and (3) would require fundamentally changing the the apparatus, which was designed to use familiar, but large and slow, "macrotrap" methods in order to reduce the unknowns in operating the machine. It is for this reason that the Michelson apparatus was retired after long years of service. Our recent efforts have focused on the design and construction of a new all-microtrap system that promises the small size and rapid BEC production required to test a Sagnac gyroscope based on Michelson interferometry.

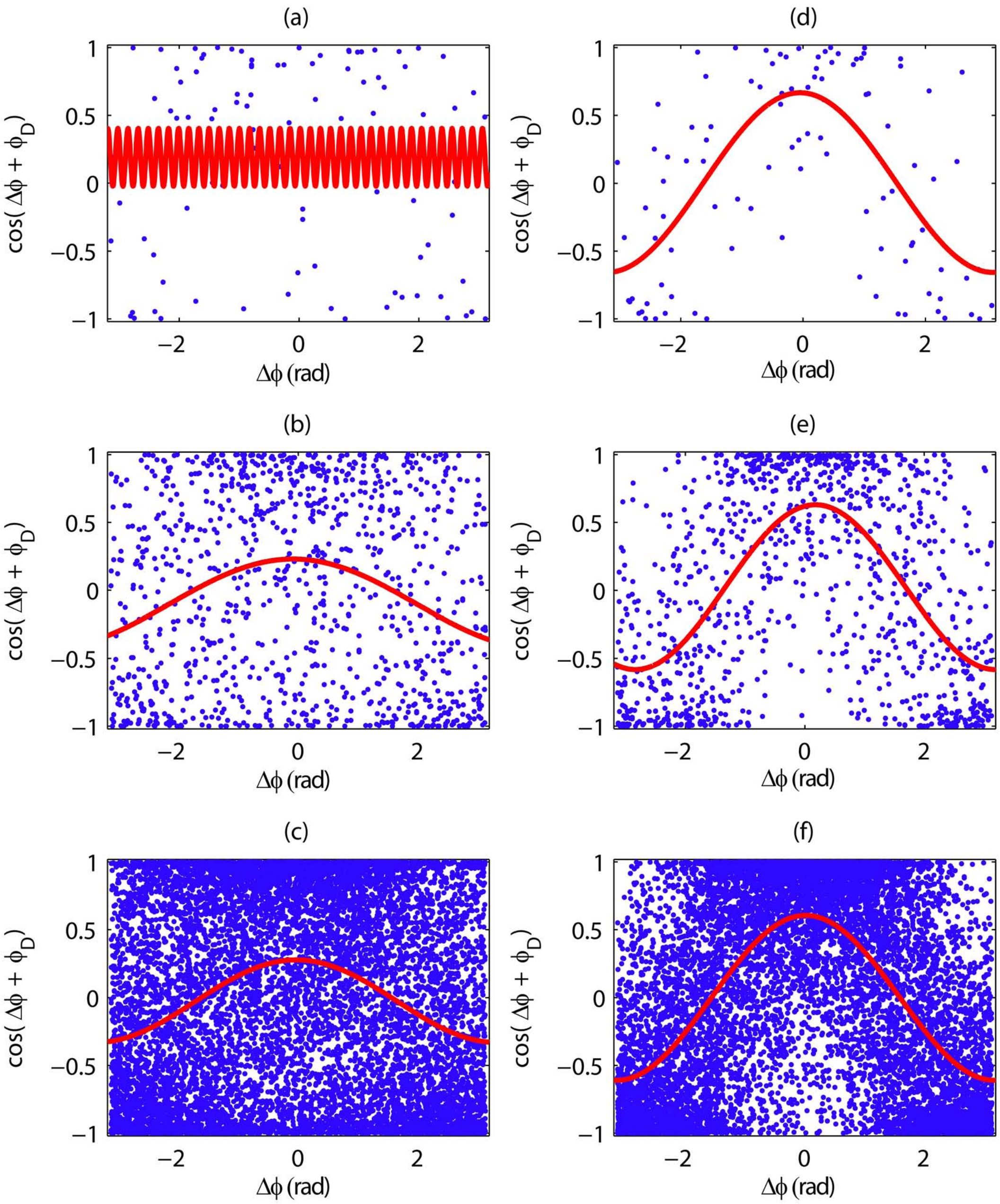

Figure 5.7: (Color). Results of simulated data sets for various numbers of trials and amount of phase diffusion. The experimenter intentionally varies $\Delta\phi$ uniformly in the range $[-\pi, \pi]$. The plots show the measured quantity $\cos(\Delta\phi + \phi_D)$, where ϕ_D is the phase noise due to diffusion. (a), (b), and (c) have $\sigma_{\Delta\phi} = 1.6$ rad with 100, 1000, and 10000 trials respectively. (d) through (f) show the results for $\sigma_{\Delta\phi} = 1$ rad. Fits to the simulated data are shown as well. A similar figure is shown in [25].

Chapter 6

Theory and design of the atom chip gyroscope

6.1 Parallel wire concept

The Michelson interferometry experiments discussed in the previous two chapters showed that guided BEC interferometry is possible. Our next step towards the goal of building an ultracold waveguide Sagnac gyroscope was to develop an area-enclosing guided interferometer that would incorporate the lessons learned from the linear Michelson interferometer.

It has been demonstrated [48] that it is possible to use a linear waveguide to guide atoms around an enclosed area. The key idea is to translate the guide transverse to its axis during the interferometry sequence. See Fig. 6.1 for a schematic of the idea. The method pursued in [48] uses a magnetic waveguide generated by an arrangement of permalloy foils poled by current-carrying coils (see Fig. 6.2). The guide's position is translated by adjusting the current in the central coils. This method has been used to translate a waveguide by about 1 mm, which is only a factor of 3 less than the diameter of a circular path that has a Sagnac phase shift of π rad at Ω_{Earth} for ^{87}Rb (see Section 1.1.3).

This coil-based approach to a moving waveguide is quite large, occupying a footprint of $200 \times 100 \times 25.4$ mm. The waveguide potential is 7 mm above the top of the foils. The large size allows the experimenters to translate the guide by simply adjusting the current running through the two central coils, but at the cost of portability.

As suggested in the conclusion of [48], an alternative approach would be to use "a mul-

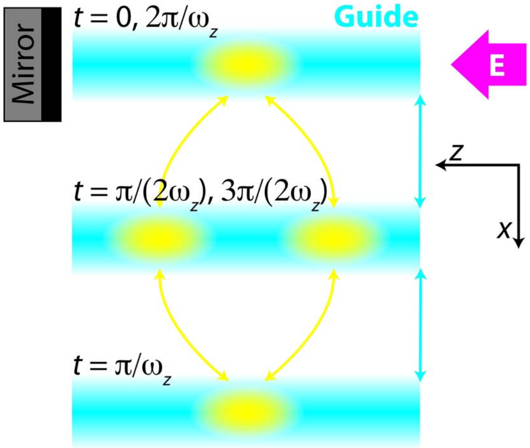

Figure 6.1: (Color). Schematic of translating waveguide interferometer. A gas of atoms (shown in yellow) is initially stationary in a magnetic waveguide (cyan) aligned along the z axis. The atomic potential includes a weak axial trap (period T) along z. At $t = 0$, a standing wave light pulse (**E**, shown in magenta) splits the cloud into two wave packets moving in opposite directions along the waveguide axis. Simultaneously, the waveguide begins to move along the x axis. The wave packets reach their classical turning points at $t = T/4$ and reverse their axial motion. At $t = T/2$, as the packets overlap at the center of the guide, the transverse motion has been stopped. It is reversed for the second half of the packets' axial oscillation, eventually bringing the packets together again in their initial position at $t = T$. A second pulse of **E** recombines the packets. Based on a figure in [48].

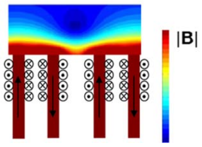

Figure 6.2: (Color) Schematic of moving guide apparatus from [48]. Coils wrapped around permalloy foils (shown in dark red) pole the foils in the indicated directions. The false color plot above the wires shows the location of the waveguide, which is aligned perpendicular to the plane of the image. By adjusting the ratio between the currents running in the inner two coils, the guide's position may be moved horizontally by about 1 mm.

tiwire 1D conveyor belt on an atom chip" to translate the waveguide. To visualize this idea, consider an atom chip patterned with an array of parallel wires [see Fig. 6.3(a)]. The wires are then driven in such a way that a waveguide that is initially positioned over wire **A** moves across the array. A very simple way to do this is to sequentially turn on and then off the current in the wires [see Fig. 6.3(b)]. The total current density of this system resembles a soliton moving down the wire array. Assuming a constant transverse bias field, the guide is effectively "handed off" by this action from wire to wire, translating it across the chip.

It is also possible to drive the wires such that the total current density of the system resembles a traveling wave moving across the array [see Fig. 6.3(c)]. When properly biased, the resulting potential would have multiple waveguides that would travel with the current wave. The traveling wave idea should be simple to apply in a practical system. While the "hand-off" concept requires an independently driven current supply for each wire, a traveling wave would be created by driving the wires periodically in space and time. For spatial period L and wire density N/L, this approach requires only N supplies. For experimental simplicity, we plan to use the traveling wave approach.

6.2 Magnetic field of parallel wires carrying sinusoidal current density

In this section, we develop the mathematics to describe the magnetic field generated by an array of parallel wires driven by a traveling wave of current. These calculations are the result

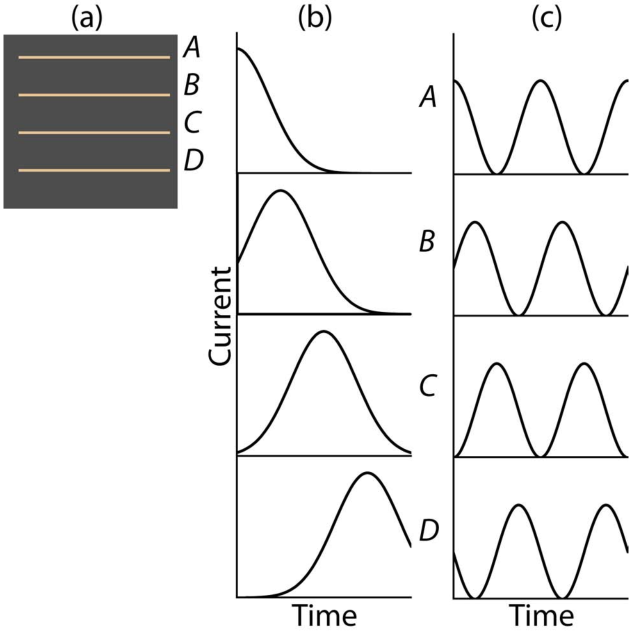

Figure 6.3: Multiple parallel wire waveguide operation. (a) Schematic of wire layout. Here, 4 parallel wires, labeled **A** through **D**, have been patterned onto a chip. A bias field transverse to the wire direction is present, but not shown. (b) "Hand-off" operation. Initially, only wire **A** has current running through it, so the guide is located directly above it. The wires are smoothly turned on and off in sequence, causing the waveguide to be handed off from one wire to the next. (c) Running wave operation. The wires are driven sinusoidally in time, each with a slight phase shift from the previous wire. Atoms initially loaded into the magnetic field minimum above wire **A** move down the array as the minimum moves.

of a collaboration with Prof. Alex Zozulya of Worcester (MA) Polytechnic Institute.

6.2.1 Field of sinusoidal current density

We begin with a stationary wave of current. Consider an infinite sheet of current in the xz plane, described by current density

$$\mathbf{J} = K(x)\delta_D(y)\hat{\mathbf{z}}. \tag{6.1}$$

Here $K(x)$ is the magnitude of the surface current density and $\delta_D(y)$ is the Dirac delta function. The field of this sheet is given by the Biot-Savart law:

$$\begin{aligned}\mathbf{B}(\mathbf{r}) &= \frac{\mu_0}{4\pi}\int \mathbf{J}(\mathbf{r}') \times \frac{\mathbf{r}-\mathbf{r}'}{|\mathbf{r}-\mathbf{r}'|^3}\, d^3x' \\ &= \frac{\mu_0}{2\pi}\int K(x')\frac{-y\hat{\mathbf{x}} + (x-x')\hat{\mathbf{y}}}{(x-x')^2+y^2}\, dx'. \end{aligned} \tag{6.2}$$

If the current density is sinusoidal with spatial period L and amplitude $K_1^{(c)}$, then

$$K(x) = K_1^{(c)} \cos\left(\frac{2\pi x}{L}\right). \tag{6.3}$$

The field for this current density is

$$\mathbf{B}(\mathbf{r}) = \frac{\mu_0 K_1^{(c)}}{2\pi}\int \cos\left(\frac{2\pi x'}{L}\right)\frac{-y\hat{\mathbf{x}} + (x-x')\hat{\mathbf{y}}}{(x-x')^2+y^2}\, dx'. \tag{6.4}$$

Fourier integrals of this type may be evaluated by the residue method [45], using the formula

$$\int_{-\infty}^{\infty} g(x)\cos wx\; dx = -2\pi \sum \text{Im Res}[g(z)e^{iwz}]. \tag{6.5}$$

Here the sum is over the residues of $g(z)e^{iwz}$ in the upper half of the complex number plane. The resulting field is

$$\mathbf{B}(\mathbf{r}) = \frac{\mu_0 K_1^{(c)}}{2} e^{-2\pi y/L}\left(-\cos\frac{2\pi x}{L}\hat{\mathbf{x}} + \sin\frac{2\pi x}{L}\hat{\mathbf{y}}\right), \tag{6.6}$$

where $y \geq 0$.

6.2.2 Field of periodic current density

Building on the previous section, we next consider the field of a sheet carrying a more general periodic current density. For spatial period L, the surface current density may be written as a Fourier series:

$$K(x) = K_0 + \sum_{n=1}^{\infty} \left(K_n^{(c)} \cos \frac{2\pi n x}{L} + K_n^{(s)} \sin \frac{2\pi n x}{L} \right). \tag{6.7}$$

The Fourier coefficients are given by

$$\begin{aligned} K_0 &= \frac{1}{L} \int_0^L K(x) \; dx \\ K_n^{(c)} &= \frac{2}{L} \int_0^L K(x) \cos \frac{2\pi n x}{L} \; dx \\ K_n^{(s)} &= \frac{2}{L} \int_0^L K(x) \sin \frac{2\pi n x}{L} \; dx. \end{aligned} \tag{6.8}$$

The field of the general periodic surface current density is found by inserting Eq. (6.7) into Eq. (6.2) to obtain

$$\begin{aligned} \mathbf{B}_0(\mathbf{r}) &= -\frac{\mu_0 K_0}{2} \hat{\mathbf{x}} \\ \mathbf{B}_n^{(c)}(\mathbf{r}) &= \frac{\mu_0 K_n^{(c)}}{2} e^{-2\pi n y/L} \left(-\cos \frac{2\pi n x}{L} \hat{\mathbf{x}} + \sin \frac{2\pi n x}{L} \hat{\mathbf{y}} \right) \\ \mathbf{B}_n^{(s)}(\mathbf{r}) &= \frac{\mu_0 K_n^{(s)}}{2} e^{-2\pi n y/L} \left(-\sin \frac{2\pi n x}{L} \hat{\mathbf{x}} - \cos \frac{2\pi n x}{L} \hat{\mathbf{y}} \right). \end{aligned} \tag{6.9}$$

Here, we have again used the Fourier cosine integral formula in Eq. (6.5), along with the similar sine formula

$$\int_{-\infty}^{\infty} g(x) \sin wx \; dx = 2\pi \sum \mathrm{Re}\ \mathrm{Res}[g(z) e^{iwz}]. \tag{6.10}$$

6.2.3 Field of sinusoidal current density generated by wires

In the previous two sections, we calculated the magnetic field generated by an infinite sheet of periodic current density. We will now consider a more realistic situation, in which the periodic current density flows through an array of parallel wires instead of a continuous sheet. See Fig. 6.4 for an illustration of the variables that will be used in this calculation.

Consider an infinite array of parallel, infinitely long wires of width Δx. The current in each wire is a periodic function of its position, with period L. There are N wires in each spatial period, where $N > 1$. The wires are evenly spaced, such that wire m begins at position

$$\hat{x}_m = \frac{L}{N} m \tag{6.11}$$

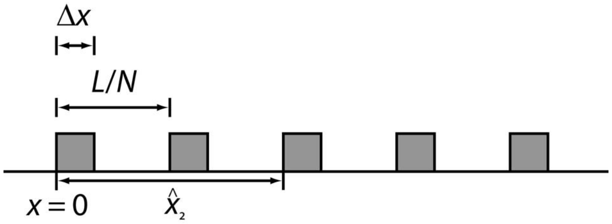

Figure 6.4: Illustration of variables associated with periodic current density calculation. Consider an array of wires carrying a sinusoidal current density of spatial period L. There are N wires in each period, spaced at a distance L/N. Δx is the wire width. $\hat{x}_m$ is the position of the left edge of wire m.

and carries current

$$I_m = I \cos \frac{2\pi m}{N}. \tag{6.12}$$

The index m runs from 0 to $N-1$. The total current density in each period is given by Eq. (6.1) where

$$K(x) = \frac{I}{\Delta x} \sum_{m=0}^{N-1} \cos \frac{2\pi m}{N} [\Theta(x - \hat{x}_m) - \Theta(x - \hat{x}_m - \Delta x)]. \tag{6.13}$$

$\Theta(x)$ is the unit step function.

To use the mathematics developed in section 6.2.2, we must write Eq. (6.13) as a Fourier series. Using Eq. (6.8) to calculate the coefficients, we find

$$\begin{aligned}
K_0 &= \frac{I}{L\Delta x}\sum_{m=0}^{N-1}\cos\frac{2\pi m}{N}\int_0^L [\Theta(x-\hat{x}_m)-\Theta(x-\hat{x}_m-\Delta x)]\;dx \\
&= \frac{I}{L}\sum_{m=0}^{N-1}\cos\frac{2\pi m}{N} \qquad (6.14)\\
K_n^{(c)} &= \frac{2I}{L\Delta x}\sum_{m=0}^{N-1}\cos\frac{2\pi m}{N}\int_0^L \cos\frac{2\pi n x}{L}[\Theta(x-\hat{x}_m)-\Theta(x-\hat{x}_m-\Delta x)]\;dx \\
&= \frac{2I}{L\Delta x}\sum_{m=0}^{N-1}\cos\frac{2\pi m}{N}\int_{\hat{x}_m}^{\hat{x}_m+\Delta x}\cos\frac{2\pi n x}{L}\;dx \\
&= \frac{I}{n\pi\Delta x}\sum_{m=0}^{N-1}\cos\frac{2\pi m}{N}\left(\sin\frac{2\pi n(\hat{x}_m+\Delta x)}{L}-\sin\frac{2\pi n\hat{x}_m}{L}\right) \\
&= \frac{I}{n\pi\Delta x}\sum_{m=0}^{N-1}\cos\frac{2\pi m}{N}\left[\sin\frac{2\pi nm}{N}\left(\cos\frac{2\pi n\Delta x}{L}-1\right)+\cos\frac{2\pi nm}{N}\sin\frac{2\pi n\Delta x}{L}\right] \qquad (6.15)\\
K_n^{(s)} &= \frac{2I}{L\Delta x}\sum_{m=0}^{N-1}\cos\frac{2\pi m}{N}\int_{\hat{x}_m}^{\hat{x}_m+\Delta x}\sin\frac{2\pi n x}{L}\;dx \\
&= \frac{I}{n\pi\Delta x}\sum_{m=0}^{N-1}\cos\frac{2\pi m}{N}\left(\cos\frac{2\pi n\hat{x}_m}{L}-\cos\frac{2\pi n(\hat{x}_m+\Delta x)}{L}\right) \\
&= \frac{I}{n\pi\Delta x}\sum_{m=0}^{N-1}\cos\frac{2\pi m}{N}\left[\cos\frac{2\pi nm}{N}\left(1-\cos\frac{2\pi n\Delta x}{L}\right)+\sin\frac{2\pi nm}{N}\sin\frac{2\pi n\Delta x}{L}\right]. \qquad (6.16)
\end{aligned}$$

To sum the series, we use the orthogonality relations of the discrete trigonometric functions [49] to state

$$\begin{aligned}
\sum_{m=0}^{N-1}\cos\frac{2\pi m}{N}\sin\frac{2\pi nm}{N} &= 0 \\
\sum_{m=0}^{N-1}\cos\frac{2\pi m}{N}\cos\frac{2\pi nm}{N} &= \frac{N}{2}(\delta_{n-1,\hat{a}N}+\delta_{n+1,\hat{a}N}) \\
\sum_{m=0}^{N-1}\sin\frac{2\pi m}{N}\sin\frac{2\pi nm}{N} &= \frac{N}{2}(\delta_{n-1,\hat{a}N}-\delta_{n+1,\hat{a}N}) \\
\sum_{m=0}^{N-1}\sin\frac{2\pi m}{N} = \sum_{m=0}^{N-1}\cos\frac{2\pi m}{N} &= 0, \qquad (6.17)
\end{aligned}$$

where $\hat{a}$ is any non-negative integer. Applying these relations, we obtain

$$\begin{aligned}
K_0 &= 0 \\
K_n^{(c)} &= \frac{NI}{L}\frac{\sin 2\alpha_n}{2\alpha_n}(\delta_{n+1,\hat{a}N}+\delta_{n-1,\hat{a}N}) \\
K_n^{(s)} &= \frac{NI}{L}\frac{\sin^2\alpha_n}{\alpha_n}(\delta_{n+1,\hat{a}N}+\delta_{n-1,\hat{a}N}) \qquad (6.18)
\end{aligned}$$

where

$$\alpha_n = \frac{n\pi\Delta x}{L}. \tag{6.19}$$

Plugging these Fourier coefficients into Eq. (6.9), we find the magnetic field of harmonic n is

$$\begin{aligned} B_{n,x} &= -B_w \frac{\sin\alpha_n}{\alpha_n} e^{-2\pi n y/L} \cos\left(\frac{2\pi n x}{L} - \alpha_n\right) \\ B_{n,y} &= B_w \frac{\sin\alpha_n}{\alpha_n} e^{-2\pi n y/L} \sin\left(\frac{2\pi n x}{L} - \alpha_n\right) \end{aligned} \tag{6.20}$$

where

$$B_w = \frac{\mu_0 I N}{2L}. \tag{6.21}$$

We see from Eq. (6.20) that the lowest nonzero harmonic has the largest amplitude, so we may approximate the field as consisting of only harmonic $n = 1$. We now add a uniform bias $B_{0,x}\hat{\mathbf{x}}$ to form waveguides in the $+y$ half space. To find the location of the waveguides, we use Eq. (6.20) to calculate the set of locations x_0 where the y component of the wire field vanishes:

$$\begin{aligned} 0 &= \sin\left(\frac{2\pi x_0}{L} - \alpha_1\right) \\ x_0 &= \frac{\Delta x}{2} + \frac{bL}{2}, \end{aligned} \tag{6.22}$$

where b is an integer. When $x = x_0$, the x component of the field vanishes at $y = y_0$, given by

$$0 = B_{0,x} - B_w \frac{\sin\alpha_1}{\alpha_1} e^{-2\pi y_0/L} \cos b\pi. \tag{6.23}$$

If both $B_{0,x} > 0$ and $B_w > 0$, then we must constrain b to be an even integer. With that constraint in place, we find

$$y_0 = \frac{L}{2\pi} \ln\left(\frac{B_w}{B_{0,x}} \frac{\sin\alpha_1}{\alpha_1}\right). \tag{6.24}$$

We see that the periodically driven array of wires forms an infinite array of waveguides at height y_0, spaced by the current's spatial period L.

The final step in this calculation is to add an axial bias field $B_{0,z}$ and then calculate the waveguide's trap frequency. We Taylor expand the field magnitude $B_1 = \sqrt{(B_{1,x} + B_{0,x})^2 + B_{1,y}^2 + B_{0,z}^2}$ around a field minimum line (x_0, y_0), finding

$$B_1 \approx |B_{0,z}| + \frac{2\pi^2 B_{0,x}^2}{|B_{0,z}| L^2} \rho^2. \tag{6.25}$$

The coordinate ρ is defined as $\rho = \sqrt{(x-x_0)^2 + (y-y_0)^2}$. The harmonic frequency of the waveguide for trapped atoms is

$$\omega_\rho = 2\pi \sqrt{\frac{g_F m_F \mu_{\mathrm{B}}}{M B_{0,z}}} \frac{B_{0,x}}{L}. \tag{6.26}$$

We see in Eq. (6.18) that the next nonzero harmonic is $n = N-1$. This harmonic contribution to the magnetic field at the center of a waveguide is insignificant when

$$\begin{aligned} \frac{\sin\alpha_1}{\alpha_1} e^{-2\pi y_0/L} &\gg \frac{\sin\alpha_{N-1}}{\alpha_{N-1}} e^{-2\pi(N-1)y_0/L} \\ 1 &\gg \frac{\alpha_1 \sin\alpha_{N-1}}{\alpha_{N-1}\sin\alpha_1} e^{-2\pi(N-2)y_0/L} \\ &\gg \left(\frac{B_{0,x}}{B_w}\right)^{N-2} \left(\frac{\alpha_1}{\sin\alpha_1}\right)^{N-1} \frac{\sin\alpha_{N-1}}{\alpha_{N-1}}. \end{aligned} \tag{6.27}$$

If this parameter is kept small, then the contributions of all higher harmonics will also be insignificant.

6.2.4 Field of traveling sinusoidal current density generated by wires

In this section we will calculate the field generated by an array of wires carrying a traveling wave of current density, in place of the stationary wave of the previous sections. The current in wire m is in this case given by

$$I_m = I \cos\left(\frac{2\pi}{L}(\hat{x}_m - v_c t)\right), \tag{6.28}$$

where v_c is the speed at which the waveguides will move across the array of wires. The wire position $\hat{x}_m$ is defined in Eq. (6.11). Using the methods of Sec. 6.2.3, we calculate the Fourier coefficients of the current density to be

$$\begin{aligned} K_0 &= 0 \\ K_n^{(c)} &= \frac{IN}{L}\frac{\sin\alpha_n}{\alpha_n}\left[\delta_{n+1,\hat{a}N}\cos\left(\frac{2\pi v_c t}{L} - \alpha_n\right) + \delta_{n-1,\hat{a}N}\cos\left(\frac{2\pi v_c t}{L} + \alpha_n\right)\right] \\ K_n^{(s)} &= \frac{IN}{L}\frac{\sin\alpha_n}{\alpha_n}\left[-\delta_{n+1,\hat{a}N}\sin\left(\frac{2\pi v_c t}{L} - \alpha_n\right) + \delta_{n-1,\hat{a}N}\sin\left(\frac{2\pi v_c t}{L} + \alpha_n\right)\right]. \end{aligned} \tag{6.29}$$

We consider now the field of the $n = 1$ harmonic only, given by

$$\begin{aligned} B_{1,x} &= -B_w \frac{\sin\alpha_1}{\alpha_1} e^{-2\pi y/L} \cos\left(\frac{2\pi}{L}(x - v_c t) - \alpha_1\right) \\ B_{1,y} &= B_w \frac{\sin\alpha_1}{\alpha_1} e^{-2\pi y/L} \sin\left(\frac{2\pi}{L}(x - v_c t) - \alpha_1\right) \end{aligned} \tag{6.30}$$

Adding bias field $\mathbf{B_0} = (B_{0,x}, 0, B_{0,z})$ to the wire fields results in an array of waveguide potentials, similar to the results of the previous section. In this case, however, the waveguides move in time along x. We calculate the waveguide positions (x_0, y_0) to be

$$\begin{aligned} x_0 &= \frac{\Delta x}{2} + v_c t + bL \\ y_0 &= \frac{L}{2\pi} \ln\left(\frac{B_w}{B_{0,x}} \frac{\sin\alpha_1}{\alpha_1}\right) \end{aligned} \tag{6.31}$$

for any integer b. The trap frequency ω_ρ is given by Eq. (6.26).

In the traveling case, unlike the stationary case, the perturbations due to the higher harmonics cause shifts in the trap potential that oscillate in time. Such oscillations could excite collective modes in a BEC trapped in the moving waveguide, so we must calculate their amplitude and frequency. We consider the total field from $n = 1$ and the next non-zero harmonic, $n = N - 1$:

$$\begin{aligned} B_x &\approx B_{0,x} \left[1 - e^{-2\pi\bar{y}/L} \cos\frac{2\pi\bar{x}}{L} \right. \\ &\qquad \left. -\beta\epsilon^{N-2} e^{-2\pi(N-1)\bar{y}/L} \cos\left(\frac{2\pi\bar{x}}{L}(N-1) + N\tilde{\omega}t\right)\right] \\ B_y &\approx B_{0,x} \left[e^{-2\pi\bar{y}/L} \sin\frac{2\pi\bar{x}}{L} \right. \\ &\qquad \left. +\beta\epsilon^{N-2} e^{-2\pi(N-1)\bar{y}/L} \sin\left(\frac{2\pi\bar{x}}{L}(N-1) + N\tilde{\omega}t\right)\right]. \end{aligned} \tag{6.32}$$

These equations use a number of new symbols. The coordinates x and y have been re-centered according to

$$\begin{aligned} \bar{x} &= x - x_0 \\ \bar{y} &= y - y_0. \end{aligned} \tag{6.33}$$

The new parameters ϵ, β, and $\tilde{\omega}$ are defined as

$$\begin{aligned}\epsilon &= e^{-2\pi y_0/L} = \frac{B_{0,x}}{B_w}\frac{\alpha_1}{\sin\alpha_1}\\ \tilde{\omega} &= \frac{2\pi v_c}{L}\\ \beta &= \frac{\sin\alpha_{N-1}}{\alpha_{N-1}}\frac{\alpha_1}{\sin\alpha_1}.\end{aligned} \tag{6.34}$$

In the following equations, we will assume that y_0 and L have been chosen so that ϵ is small. The parameter β will also be small for larger values of N. We next Taylor expand the field around $\bar{x} = \bar{y} = \epsilon = 0$, obtaining

$$\begin{aligned}B \approx{}& B_{0,z} + \frac{2\pi^2}{L^2}\frac{B_{0,x}^2}{B_{0,z}}(\bar{x}^2 + \bar{y}^2)\\ &+ \frac{2\pi}{L}\frac{B_{0,x}^2}{B_{0,z}}\beta\epsilon^{N-2}(\bar{x}\sin N\tilde{\omega}t - \bar{y}\cos N\tilde{\omega}t)\\ &+ \frac{2\pi^2}{L^2}\frac{B_{0,x}^2}{B_{0,z}}\beta\epsilon^{N-2}[(2N-3)\bar{x}^2\cos N\tilde{\omega}t - 2\bar{x}\bar{y}\sin N\tilde{\omega}t + (2N-1)\bar{y}^2\cos N\tilde{\omega}t].\end{aligned} \tag{6.35}$$

The potential for an atom in this field is

$$\begin{aligned}U ={}& \frac{\hbar\omega_\rho}{2\rho_0^2}\Big(\bar{x}^2 + \bar{y}^2\\ &+ \frac{L}{\pi}\beta\epsilon^{N-2}(\bar{x}\sin N\tilde{\omega}t - \bar{y}\cos N\tilde{\omega}t)\\ &+ \beta\epsilon^{N-2}[(2N-3)\bar{x}^2\cos N\tilde{\omega}t + (2N-1)\bar{y}^2\cos N\tilde{\omega}t]\\ &- 2\beta\epsilon^{N-2}\bar{x}\bar{y}\sin N\tilde{\omega}t\Big),\end{aligned} \tag{6.36}$$

where the trap frequency ω_ρ is given in Eq. (6.26) and $\rho_0 = \sqrt{\hbar/M\omega_\rho}$ is the harmonic oscillator length scale. This is a two-dimensional harmonic oscillator potential with a small periodic driving force (third term), and periodic perturbations to the trap shape (fourth and fifth terms).

6.3 Collective mode excitation due to parallel wires

In this section, we calculate the amplitudes of the collective modes that the perturbation terms in Eq. (6.36) could excite in a trapped BEC. A BEC whose shape is oscillating during the experiment will also have an oscillating mean-field interaction energy. The interaction phase evolution term in the BEC wavefunction, $\exp[i\mu_j(N_j,t)t/\hbar]$ (see Sec. 5.1.2), will therefore have a complicated time dependence. Consequently, the calculation of quantum phase diffusion effects in the case of excited BECs is more complex. Modeling the outcome of our interferometry experiments will be much simpler if we can keep the excitation amplitudes very small, so that the BECs are still well-described by a static wavefunction.

6.3.1 Slosh modes

The lowest energy collective modes for a BEC in a harmonic trap are the dipole or "slosh" modes. In these modes, the condensate's center of mass oscillates in the trap at the harmonic frequency; the BEC itself does not change its shape. By keeping these modes small, we ensure that the transverse motion of our trapped condensates is well-described by $x_0(t)$. This mode is equivalent to the oscillation of a classical system in a harmonic potential. Just as with a classical oscillator, the BEC can be forced into sloshing by the application of a driving force such as the one in the third term of Eq. (6.36). The equation of motion of the center of mass along the $\bar{y}$ axis is [50]

$$\bar{y} = \frac{\hbar\omega_\rho}{2\rho_0^2}\frac{L\beta\epsilon^{N-2}}{\pi M(\omega_\rho^2 - N^2\tilde{\omega}^2)}(-\cos\omega_\rho t + \cos N\tilde{\omega}t), \tag{6.37}$$

for a condensate that is initially at rest when the non-resonant driving force is turned on. The oscillations along the $\bar{x}$ axis have the same amplitude. We want these amplitudes to be small with respect to the size of the condensate, which for a typical condensate of atoms with repelling interactions is slightly larger than the harmonic oscillator length ρ_0 [35]. Thus, oscillations obeying

$$1 \gg \frac{L}{2\pi\rho_0}\left|\frac{\omega_\rho^2}{\omega_\rho^2 - N^2\tilde{\omega}^2}\right|\beta\epsilon^{N-2} \tag{6.38}$$

will be acceptably small.

For the case of resonant drive, the equation of motion is

$$\bar{y} = \frac{\hbar\omega_\rho}{4\rho_0^2}\frac{L\beta\epsilon^{N-2}}{\pi M\omega_\rho}t\sin\omega_\rho t. \tag{6.39}$$

The condition for small oscillations is

$$1 \gg \frac{L}{2\pi\rho_0}\omega_\rho \check{T}\beta\epsilon^{N-2}, \tag{6.40}$$

where $\check{T}$ is the duration of the resonant drive.

6.3.2 Breathing and quadrupole modes

The fourth term in Eq. (6.36) causes periodic perturbations to the trap frequency of the guide potential, in the form

$$\omega_j^2 = \omega_\rho^2(1 + \eta_j \cos\tilde{\Omega}\tau). \tag{6.41}$$

In this equation, the amplitude of the modulation is given by

$$\begin{aligned} \eta_x &= \beta\epsilon^{N-2}(2N-3) \\ \eta_y &= \beta\epsilon^{N-2}(2N-1), \end{aligned} \tag{6.42}$$

the dimensionless perturbation frequency is

$$\tilde{\Omega} = \frac{N\tilde{\omega}}{\omega_\rho}, \tag{6.43}$$

and the dimensionless time coordinate is

$$\tau = \omega_\rho t. \tag{6.44}$$

These perturbations cause collective oscillations of the shape of a trapped condensate (referred to here as "shape oscillations"). We will use a semi-classical treatment [51] to find the lowest-energy shape oscillations, as well as design constraints that make excitation of those modes unlikely.

Consider a BEC in the waveguide potential of Eq. (6.36), to which has been added a much weaker axial confinement of trap frequency ω_z. In the Thomas-Fermi limit, the density of a BEC in this time-dependent trap is

$$N|\Psi(\mathbf{r},t)|^2_{\mathrm{TF}} = \frac{\mu - \sum_{j=1}^{3} M\omega_j^2(0)r_j^2/[2\lambda_j^2(t)]}{g\lambda_x(t)\lambda_y(t)\lambda_z(t)}, \tag{6.45}$$

where μ is the chemical potential and g is the contact interaction strength. The dimensionless scaling parameters λ_j obey a system of differential equations

$$\ddot{\lambda}_j = \frac{\omega_j^2(0)}{\lambda_j \lambda_x \lambda_y \lambda_z} - \omega_j^2(t)\lambda_j, \tag{6.46}$$

where $j = x,\ y,$ or z. In the limit of small modulation amplitudes, where $\eta_j \ll 1$, this system may be simplified by defining $\lambda_j = 1 + \delta\lambda_j$ and dropping terms that are second order or higher in $\delta\lambda_j$ and η_j. We obtain a linear approximation to Eq. (6.46):

$$\begin{aligned}
\frac{d^2}{d\tau^2}\delta\lambda_x(\tau) &= -3\delta\lambda_x - \delta\lambda_y - \delta\lambda_z + \eta_x(1 - \cos\tilde{\Omega}\tau) \\
\frac{d^2}{d\tau^2}\delta\lambda_y(\tau) &= -3\delta\lambda_y - \delta\lambda_x - \delta\lambda_z + \eta_y(1 - \cos\tilde{\Omega}\tau) \\
\frac{d^2}{d\tau^2}\delta\lambda_z(\tau) &= \gamma^2(-3\delta\lambda_z - \delta\lambda_x - \delta\lambda_y),
\end{aligned} \tag{6.47}$$

where $\gamma = \omega_z/\omega_\rho \ll 1$. To leading order in γ, the eigenmodes of this system are a slowly oscillating quadrupole mode at $\tilde{\Omega}_{\text{slow}} = \sqrt{5/2}\gamma$ along $(1, 1, -4)$ [Fig. 6.5(a)], a breathing mode at $\tilde{\Omega}_{\text{breathe}} = 2$ along $(1, 1, 0)$ [Fig. 6.5(b)], and a quickly oscillating quadrupole mode at $\tilde{\Omega}_{\text{fast}} = \sqrt{2}$ along $(1, -1, 0)$ [Fig. 6.5(c)].

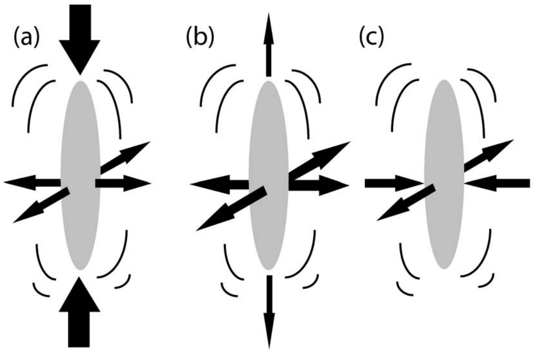

Figure 6.5: Lowest energy shape oscillations of a BEC in a cylindrically symmetric trap. (a) Slow quadrupole mode: radial size oscillates out of phase with axial size. (b) Breathing mode: radial and axial sizes oscillate in phase. (c) Fast quadrupole mode: radial size oscillates with $m = 2$ symmetry [30].

The general solution of this system can be found by first using the method of undetermined coefficients to find the particular solution. The general solution is the sum of the particular solution and oscillations at the eigenfreqencies, where the amplitudes are set so that the system is initially in equilibrium. For non-resonant drive, the general solution is

$$\begin{aligned}
\delta\lambda_x = &-\frac{1}{4}(1+2R_1-2R_2)(\eta_x-\eta_y)\cos\sqrt{2}\tau \\
&-\frac{1}{8}(1+4R_1+4R_2+2R_z)(\eta_x+\eta_y)\cos 2\tau \\
&+\frac{1}{40}(10R_z-1)(\eta_x+\eta_y)\cos\sqrt{\frac{5}{2}}\gamma\tau+\frac{4\eta_x-\eta_y}{10}+(R_1\eta_x+R_2\eta_y)\cos\tilde{\Omega}\tau \\
\delta\lambda_y = &\frac{1}{4}(1+2R_1-2R_2)(\eta_x-\eta_y)\cos\sqrt{2}\tau \\
&-\frac{1}{8}(1+4R_1+4R_2+2R_z)(\eta_x+\eta_y)\cos 2\tau \\
&\frac{1}{40}(10R_z-1)(\eta_x+\eta_y)\cos\sqrt{\frac{5}{2}}\gamma\tau+\frac{4\eta_y-\eta_x}{10}+(R_2\eta_x+R_1\eta_y)\cos\tilde{\Omega}\tau \\
\delta\lambda_z = &\frac{1}{10}(1-10R_z)(\eta_x+\eta_y)\cos\sqrt{\frac{5}{2}}\gamma\tau-\frac{\eta_x+\eta_y}{10}+R_z(\eta_x+\eta_y)\cos\tilde{\Omega}\tau.
\end{aligned} \tag{6.48}$$

The frequency-dependent parts of the amplitudes have been abbreviated as

$$\begin{aligned}
R_1 &= \frac{\tilde{\Omega}^4+8\gamma^2-3\tilde{\Omega}^2(1+\gamma^2)}{(\tilde{\Omega}^2-2)[\tilde{\Omega}^4+10\gamma^2-\tilde{\Omega}^2(4+3\gamma^2)]} \\
R_2 &= \frac{\tilde{\Omega}^2-2\gamma^2}{(\tilde{\Omega}^2-2)[\tilde{\Omega}^4+10\gamma^2-\tilde{\Omega}^2(4+3\gamma^2)]} \\
R_z &= \frac{\gamma^2}{\tilde{\Omega}^4+10\gamma^2-\tilde{\Omega}^2(4+3\gamma^2)}.
\end{aligned} \tag{6.49}$$

To prevent excitation of shape oscillations with a non-resonant drive frequency $\tilde{\Omega}$, we must design our array of wires such that all of the amplitudes are much less than 1.

The worst-case scenario for exciting these modes is resonant drive. If the drive frequency is equal to any of the mode frequencies, then the oscillation amplitudes will increase linearly with time (we are ignoring dissipative effects). The method of undetermined coefficients may be used once again to calculate these amplitudes:

$$\begin{aligned}
a_{\text{fast,resonant}} &= \frac{\sqrt{2}}{4}\beta\epsilon^{N-2}\omega_\rho\check{T} \\
a_{\text{breathe,resonant}} &= \frac{1}{2}(N-1)\beta\epsilon^{N-2}\omega_\rho\check{T} \\
a_{\text{slow,resonant}} &= \gamma\frac{\sqrt{10}}{10}(N-1)\beta\epsilon^{N-2}\omega_\rho\check{T}.
\end{aligned} \tag{6.50}$$

Here, $\check{T}$ denotes the amount of time spent driving on resonance. Note that the amplitude given for the slow mode in Eq. (6.50) is actually the amplitude of the size oscillation along the weak trap axis, which is 4 times larger than the amplitude in the radial direction.

The fifth term in Eq. (6.36) likewise will cause periodic perturbations to the harmonic confinement, but along a set of axes rotated by $\pi/4$ rad in the $\bar{x}\bar{y}$ plane. To see this, define the new coordinate system

$$\begin{aligned} x' &= \frac{\bar{x}+\bar{y}}{\sqrt{2}} \\ y' &= \frac{-\bar{x}+\bar{y}}{\sqrt{2}} \\ z' &= z. \end{aligned} \tag{6.51}$$

The fifth term in Eq. (6.36) is now given by

$$\Delta U = \frac{\hbar\omega_\rho}{2\rho_0^2}\beta\epsilon^{N-2}(y'^2 - x'^2)\sin N\tilde{\omega}t. \tag{6.52}$$

The resulting perturbations to the rotated system's trap frequencies are

$$\begin{aligned} \omega_{x'}^2 &= \omega_\rho^2(1-\eta_{xy}\sin\tilde{\Omega}\tau) \\ \omega_{y'}^2 &= \omega_\rho^2(1+\eta_{xy}\sin\tilde{\Omega}\tau), \end{aligned} \tag{6.53}$$

where the amplitude of the modulation is

$$\eta_{xy} = \beta\epsilon^{N-2}. \tag{6.54}$$

The dynamics of the resulting shape oscillations are described by a system of differential equations similar to Eq. (6.47):

$$\begin{aligned} \frac{d^2}{d\tau^2}\delta\lambda_{x'}(\tau) &= -3\delta\lambda_x - \delta\lambda_y - \delta\lambda_z + \eta_{xy}\sin\tilde{\Omega}\tau \\ \frac{d^2}{d\tau^2}\delta\lambda_{y'}(\tau) &= -3\delta\lambda_y - \delta\lambda_x - \delta\lambda_z - \eta_{xy}\sin\tilde{\Omega}\tau \\ \frac{d^2}{d\tau^2}\delta\lambda_{z'}(\tau) &= \gamma^2(-3\delta\lambda_z - \delta\lambda_x - \delta\lambda_y). \end{aligned} \tag{6.55}$$

The eigenmodes of the new system are the same, but the general solution will be different. Once more using the method of undetermined coefficients, we calculate the general solution for non-resonant drive. Assuming a condensate initially in equilibrium, the general solution for the scale factor changes is

$$\begin{aligned}
\delta\lambda_{x'} &= \frac{\eta_{xy}}{2-\tilde{\Omega}^2}\left(-\frac{\tilde{\Omega}}{\sqrt{2}}\sin\sqrt{2}\tau + \sin\tilde{\Omega}\tau\right) \\
\delta\lambda_{y'} &= \frac{\eta_{xy}}{2-\tilde{\Omega}^2}\left(\frac{\tilde{\Omega}}{\sqrt{2}}\sin\sqrt{2}\tau - \sin\tilde{\Omega}\tau\right) \\
\delta\lambda_{z'} &= 0.
\end{aligned} \tag{6.56}$$

For resonant driving frequency $\tilde{\Omega} = \sqrt{2}$, the amplitude of scale factor oscillations along both x' and y' is

$$a' = \frac{\sqrt{2}}{4}\beta\epsilon^{N-2}\omega_\rho\check{T}. \tag{6.57}$$

6.3.3 Collective mode minimizing parameters

Table 6.1 summarizes the resonant frequencies and the normalized amplitudes that must be kept much smaller than 1 for each oscillation to be small. Amplitudes are given for both resonant drive (“res”) and non-resonant drive (“nr”). For the shape oscillations along the unprimed axes, we give the amplitude of each oscillating term in Eq. (6.48). For the terms oscillating at the resonance frequencies, the largest amplitude oscillation out of all three axes is given. The “particular” term is the term in Eq. (6.48) that oscillates at the drive frequency $\tilde{\Omega}$. A similar naming convention is used for the primed axes. These amplitudes must all be kept much smaller than 1 to avoid exciting collective modes. The resonance frequencies are given in dimensionless units.

6.4 Parallel wire design parameters

In this section, we use the mode amplitudes calculated in the previous section to estimate values for period L, wire density N, and wire width Δx such that the amplitudes of collective modes will be kept acceptably small. We begin by initially ignoring the effects of wire width.

Term/mode name	Frequency of oscillation	Normalized amplitude	Source equation
Slosh, nr	1	$\frac{L}{2\pi\rho_0}\left\lvert\frac{1}{1-\tilde{\Omega}^2}\right\rvert\beta\epsilon^{N-2}$	(6.38)
Slosh, res	1	$\frac{L}{2\pi\rho_0}\omega_\rho\check{T}\beta\epsilon^{N-2}$	(6.40)
Breathing, nr	2	$(N-1)\left\lvert\frac{1+4R_1+4R_2+2R_z}{2}\right\rvert\beta\epsilon^{N-2}$	(6.48), (6.49)
Fast quadrupole, nr	$\sqrt{2}$	$\left\lvert\frac{1+2R_1-2R_2}{2}\right\rvert\beta\epsilon^{N-2}$	(6.48), (6.49)
Slow quadrupole, nr	$\sqrt{5/2}\gamma$	$\left\lvert\frac{2(1-10R_z)}{5}\right\rvert\beta\epsilon^{N-2}$	(6.48), (6.49)
$\delta\lambda_x$, particular nr	$\tilde{\Omega}$	$\lvert(2N-3)R_1+(2N-1)R_2\rvert\beta\epsilon^{N-2}$	(6.48), (6.49)
$\delta\lambda_y$, particular nr	$\tilde{\Omega}$	$\lvert(2N-1)R_1+(2N-3)R_2\rvert\beta\epsilon^{N-2}$	(6.48), (6.49)
$\delta\lambda_z$, particular nr	$\tilde{\Omega}$	$4(N-1)\lvert R_z\rvert\beta\epsilon^{N-2}$	(6.48), (6.49)
Breathing, res	2	$\frac{1}{2}(N-1)\omega_\rho\check{T}\beta\epsilon^{N-2}$	(6.50)
Fast quadrupole, res	$\sqrt{2}$	$\frac{\sqrt{2}}{4}\omega_\rho\check{T}\beta\epsilon^{N-2}$	(6.50)
Slow quadrupole, res	$\sqrt{5/2}\gamma$	$\frac{\sqrt{10}}{10}(N-1)\omega_z\check{T}\beta\epsilon^{N-2}$	(6.50)
Fast quadrupole, nr, primed axes	$\sqrt{2}$	$\left\lvert\frac{\tilde{\Omega}}{\sqrt{2}(2-\tilde{\Omega}^2)}\right\rvert\beta\epsilon^{N-2}$	(6.56)
Particular, nr, primed axes	$\sqrt{2}$	$\left\lvert\frac{1}{2-\tilde{\Omega}^2}\right\rvert\beta\epsilon^{N-2}$	(6.56)
Fast quadrupole, res, primed axes	$\sqrt{2}$	$\frac{\sqrt{2}}{4}\omega_\rho\check{T}\beta\epsilon^{N-2}$	(6.57)

Table 6.1: Normalized amplitudes of collective mode oscillations for sinusoidally driven parallel wires

For $\Delta x = 0$,

$$\begin{aligned} \beta &= \frac{\sin \alpha_{N-1}}{\alpha_{N-1}} \frac{\alpha_1}{\sin \alpha_1} \\ &= 1. \end{aligned} \tag{6.58}$$

We next assume that we will use ^{87}Rb, confined at $\omega_\rho = 2\pi \times 80$ Hz and $y_0 = 300$ μm (the values used in the Michelson interferometry experiments). To avoid being sensitive to the low-frequency vibrations of the apparatus (discussed in the previous chapter), we will set $\omega_z = 2\pi \times 10$ Hz. As the experimental duration in this case is only 100 ms, the effects of quantum phase diffusion should be smaller than they were in previous work.

We see in lines 6 and 7 of Table 6.1 that, apart from the effects of resonances and wire width, the shape oscillation amplitudes will be small if the parameter

$$c_1 = (2N-1)\epsilon^{N-2} \tag{6.59}$$

is small. Similarly, the sloshing mode amplitudes will be small if the parameter

$$c_2 = \frac{L}{2\pi\rho_0}\epsilon^{N-2} \tag{6.60}$$

is small. Note that for ^{87}Rb and our desired confinement, $\rho_0 = 1.21$ μm. Figure 6.6 shows the values of c_1 and c_2 as a function of L for various values of N. We see in these plots that reasonable choices for the wire layout are $L = 1.2$ mm and $N = 8$, such that $c_1 = 1.2 \times 10^{-3}$ and $c_2 = 0.013$. The wire pitch for these values is 150 μm.

Using these parameter choices, we now calculate the effects of resonances and wire width. Our design goal is to construct a Sagnac gyroscope using ^{87}Rb that records a phase shift of π rad when rotating at Earth's rotation rate. As discussed in section 1.1.3, a circular path of radius 1.6 mm achieves this sensitivity. To move 4×1.6 mm $= 6.4$ mm in 100 ms, we would have to translate the guide at an average speed of $v_c = 6.4$ cm/s. The average drive frequency for trap perturbations is therefore $N\tilde{\omega} = 2\pi \times 427$ Hz, or $\tilde{\Omega} = 5.33$ in dimensionless units. Numerical results for the amplitudes of the collective modes are shown in Table 6.2. We see that our choice

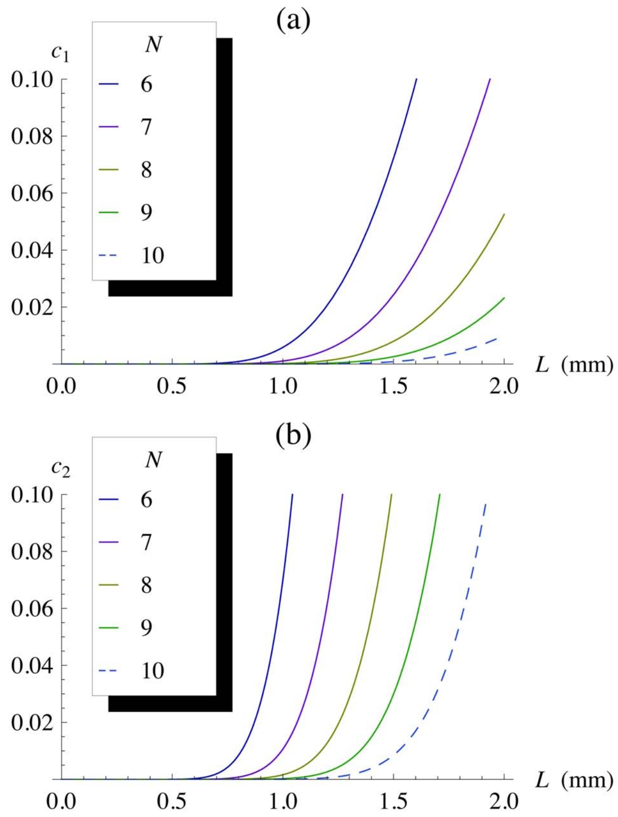

Figure 6.6: (Color). Plot of parameters (a) c_1 and (b) c_2 for vs. L for various values of N.

of N and L should not cause large excitations of collective modes while the guide is moving at this average speed.

Term/mode name	Amplitude ($\Delta x = 0$)	Amplitude ($\Delta x = 80\ \mu$m)
Slosh, nr	4.7×10^{-4}	3.2×10^{-4}
Slosh, res	$6.4\check{T}$	$4.4\check{T}$
Breathing, nr	3.3×10^{-4}	2.2×10^{-4}
Fast quadrupole, nr	4.3×10^{-5}	3.0×10^{-4}
Slow quadrupole, nr	3.2×10^{-5}	2.2×10^{-4}
$\delta\lambda_x$, particular nr	4.3×10^{-5}	2.9×10^{-5}
$\delta\lambda_y$, particular nr	4.9×10^{-5}	3.4×10^{-5}
$\delta\lambda_z$, particular nr	5.1×10^{-8}	3.5×10^{-8}
Breathing, res	$0.14\check{T}$	$0.097\check{T}$
Fast quadrupole, res	$0.014\check{T}$	$0.0098\check{T}$
Slow quadrupole, res	$0.09\check{T}$	$0.061\check{T}$
Fast quadrupole, nr, primed axes	1.2×10^{-5}	7.9×10^{-6}
Particular, nr, primed axes	3.1×10^{-6}	2.1×10^{-6}
Fast quadrupole, res, primed axes	$0.014\check{T}$	$0.0098\check{T}$

Table 6.2: Values of amplitude parameters from Table 6.1 for $L = 1.2$ mm, $N = 8$.

The last analytic calculation to be carried out is the effect of finite wire width Δx. We want to use wide wires to reduce resistance, and therefore heat dissipation. For the pitch of 150 μm that we chose in this section, a wire width of 80 μm occupies just over 50% of the available chip surface area. The wire width parameter for this design choice is $\beta = 0.68$. The collective mode amplitudes for this wire width are shown in Table 6.2.

6.5 Transverse acceleration profile

We conclude this chapter by considering the acceleration of the guide. Jumping immediately from a stationary waveguide to a moving guide at velocity v_c would surely excite large-amplitude dipole slosh modes along the x axis. We will instead design a smooth acceleration profile. The analytical approach we follow here calculates formulas for the area enclosed by this profile for BECs that are split using the familiar techniques of the Michelson experiment. We also find the expected slosh amplitude, which is minimized by setting $1/\gamma$ equal to an even integer. For our selected trap frequencies, we calculate a transport distance of 1.1 mm with minimal sloshing, providing an enclosed area greater than 1 mm^2.

6.5.1 Motion of the trap center

We consider a motion sequence composed of two consecutive periods of sinusoidal acceleration of opposite sign (see Fig. 6.7). The first half of the drive sequence moves the BECs away from their initial position at $x = 0$, leaving them nearly at rest at a turning point $x(T/2)$. The second half of the drive sequence brings them back to their initial position.

Motion of the BECs in the accelerating trap is determined by the differential equation

$$\ddot{x}(t) = -\omega_\rho^2 \left[x(t) - x_0(t) \right], \tag{6.61}$$

where $x(t)$ is the position of the BECs along the x axis and $x_0(t)$ is the position of the trap center. The acceleration $a_c(t)$ of the trap center is given by the piecewise sinusoidal waveform

$$a_c(t) = K_a \times \begin{cases} \sin \hat{\Omega} t & 0 \leq t < \hat{T} \\ -\sin \hat{\Omega}(t - \hat{T}) & \hat{T} \leq t < 2\hat{T} \end{cases}, \tag{6.62}$$

where K_a is a constant, the drive frequency is $\hat{\Omega} = 2\omega_z$, and $\hat{T} = 2\pi/\hat{\Omega}$ is the drive period. The acceleration is integrated over time to give the velocity $v_c(t)$ of the trap center:

$$v_c(t) = \frac{K_a}{\hat{\Omega}} \times \begin{cases} 1 - \cos \hat{\Omega} t & 0 \leq t < \hat{T} \\ -1 + \cos \hat{\Omega}(t - \hat{T}) & \hat{T} \leq t < 2\hat{T} \end{cases}. \tag{6.63}$$

The velocity is integrated a second time to yield the position $x_c(t)$ of the trap center:

$$x_0(t) = \frac{K_a}{\hat{\Omega}^2} \times \begin{cases} \hat{\Omega} t - \sin \hat{\Omega} t & 0 \leq t < \hat{T} \\ \hat{\Omega}(2\hat{T} - t) + \sin \hat{\Omega}(t - \hat{T}) & \hat{T} \leq t < 2\hat{T} \end{cases}. \tag{6.64}$$

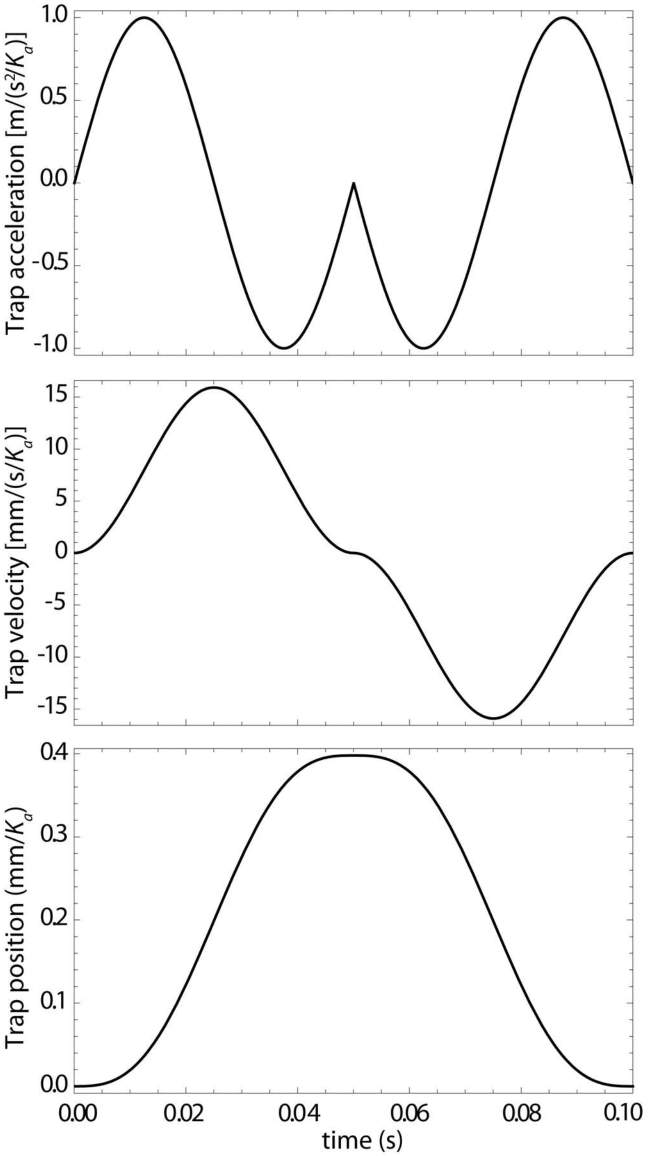

Figure 6.7: Acceleration, velocity, and position of the trap center for $\omega_z = 2\pi \times 10$ Hz.

6.5.2 Equation of motion of the BECs

To find the equation of motion for the BECs, we solve Eq. (6.61) using Eq. (6.64) for the trap position $x_c(t)$. For the first half of the sequence, where $0 \leq t < \hat{T}$, the general solution is

$$x^{(1)}(t) \quad = \quad A_1 \sin \omega_\rho t + A_2 \cos \omega_\rho t + A_3 t + A_4 \sin \hat{\Omega} t + A_5, \tag{6.65}$$

where the A_i are constants. The BECs move in phase with the sinusoidal acceleration ramp, and therefore there is no quadrature term in the solution (i.e. a term proportional to $\cos \hat{\Omega} t$). The particular solution coefficients are

$$\begin{aligned} A_3 &= \frac{K_a}{\hat{\Omega}} \\ A_4 &= \frac{K_a \omega_\rho^2}{\hat{\Omega}^2(\hat{\Omega}^2 - \omega_\rho^2)} \\ A_5 &= 0. \end{aligned} \tag{6.66}$$

Here, we assume that the BECs are initially at $x = 0$ and are not sloshing. The solution is therefore

$$x^{(1)}(t) = \frac{K_a \hat{\Omega}}{\omega_\rho(\omega_\rho^2 - \hat{\Omega}^2)} \sin \omega_\rho t + \frac{K_a}{\hat{\Omega}} t + \frac{K_a \omega_\rho^2}{\hat{\Omega}^2(\hat{\Omega}^2 - \omega_\rho^2)} \sin \hat{\Omega} t. \tag{6.67}$$

To solve Eq. (6.61) for the second half of the drive sequence, where $\hat{T} < t \leq 2\hat{T}$, we use for initial conditions the final values of position and velocity obtained from Eq. (6.67):

$$\begin{aligned} x^{(1)}(\hat{T}) &= \frac{K_a \hat{\Omega}}{\omega_\rho(\omega_\rho^2 - \hat{\Omega}^2)} \sin \omega_\rho \hat{T} + \frac{K_a}{\hat{\Omega}} \hat{T} \\ \dot{x}^{(1)}(\hat{T}) &= \frac{K_a \hat{\Omega}}{\omega_\rho^2 - \hat{\Omega}^2} \cos \omega_\rho \hat{T} + \frac{K_a}{\hat{\Omega}} + \frac{K_a \omega_\rho^2}{\hat{\Omega}(\hat{\Omega}^2 - \omega_\rho^2)}. \end{aligned} \tag{6.68}$$

The general solution is

$$\begin{aligned} x^{(2)}(t) =& A_1' \sin \omega_\rho (t - \hat{T}) + A_2' \cos \omega_\rho (t - \hat{T}) \\ &+ A_3'(t - \hat{T}) + A_4' \sin \hat{\Omega}(t - \hat{T}) + A_5', \end{aligned} \tag{6.69}$$

where the particular solution coefficients are

$$\begin{aligned} A_3' &= -\frac{K_a}{\hat{\Omega}} \\ A_4' &= \frac{K_a \omega_\rho^2}{\hat{\Omega}^2(\omega_\rho^2 - \hat{\Omega}^2)} \\ A_5' &= \frac{K_a \hat{T}}{\hat{\Omega}}. \end{aligned} \tag{6.70}$$

The initial condition $\dot{x}^{(2)}(\hat{T}) = \dot{x}^{(1)}(\hat{T})$ is satisfied when

$$A_1' = \frac{\dot{x}^{(1)}(\hat{T})}{\omega_\rho} + \frac{K_a \hat{\Omega}}{\omega_\rho(\hat{\Omega}^2 - \omega_\rho^2)}. \tag{6.71}$$

In addition, the initial condition $x^{(2)}(\hat{T}) = x^{(1)}(\hat{T})$ is satisfied when

$$A_2' = x^{(1)}(\hat{T}) - \frac{K_a \hat{T}}{\hat{\Omega}}. \tag{6.72}$$

The complete solution for $x^{(2)}(t)$ is

$$\begin{aligned} x^{(2)}(t) =& \frac{K_a \hat{\Omega}}{\omega_\rho(\omega_\rho^2 - \hat{\Omega}^2)} (\cos \omega_\rho \hat{T} - 2) \sin \omega_\rho (t - \hat{T}) \\ &+ \frac{K_a \hat{\Omega}}{\omega_\rho(\omega_\rho^2 - \hat{\Omega}^2)} \sin \omega_\rho \hat{T} \cos \omega_\rho (t - \hat{T}) \\ &- \frac{K_a}{\hat{\Omega}} (t - 2\hat{T}) - \frac{K_a \omega_\rho^2}{\hat{\Omega}^2(\hat{\Omega}^2 - \omega_\rho^2)} \sin \hat{\Omega}(t - \hat{T}). \end{aligned} \tag{6.73}$$

6.5.3 Even-ratio trap frequencies

If either the final position $x^{(2)}(2\hat{T})$ or final velocity $\dot{x}^{(2)}(2\hat{T})$ are not zero, then the BECs will slosh in the final stationary trap. Fortunately, we can eliminate this final slosh if $1/\gamma$ is an even integer m. In this case

$$\begin{aligned} \sin \omega_\rho \hat{T} &= 0 \\ \cos \omega_\rho \hat{T} &= 1. \end{aligned} \tag{6.74}$$

The transverse position and velocity in the second half of the trajectory simplify to

$$\begin{aligned} x^{(2)}(t) &= \frac{K_a \hat{\Omega}}{\omega_\rho(\hat{\Omega}^2 - \omega_\rho^2)} \sin \omega_\rho t + \frac{K_a}{\hat{\Omega}} (2\hat{T} - t) - \frac{K_a \omega_\rho^2}{\hat{\Omega}^2(\hat{\Omega}^2 - \omega_\rho^2)} \sin \hat{\Omega} t \\ \dot{x}^{(2)}(t) &= \frac{K_a \hat{\Omega}}{\hat{\Omega}^2 - \omega_\rho^2} \cos \omega_\rho t - \frac{K_a}{\hat{\Omega}} - \frac{K_a \omega_\rho^2}{\hat{\Omega}(\hat{\Omega}^2 - \omega_\rho^2)} \cos \hat{\Omega} t, \end{aligned} \tag{6.75}$$

both of which vanish at $t = 2\hat{T}$.

Note that even though the BECs do not slosh after the drive sequence has ended, they do deviate from the trap center during the course of their trajectories. Figure 6.8 shows the deviation for $\omega_\rho = 2\pi \times 80$ Hz and $\omega_z = 2\pi \times 10$ Hz during the second half of the trajectory. The deviation is

$$x^{(2)}(t) - x_0(t) = \frac{K_a \hat{\Omega}}{\omega_\rho(\hat{\Omega}^2 - \omega_\rho^2)} \sin \omega_\rho t + \frac{K_a}{\omega_\rho^2 - \hat{\Omega}^2} \sin \hat{\Omega} t. \tag{6.76}$$

Since $\omega_\rho > \hat{\Omega}$, the second term dominates. The amplitude of the residual slosh is therefore approximately

$$\kappa = \frac{K_a}{\omega_\rho^2 - \hat{\Omega}^2}. \tag{6.77}$$

As long as κ is not much more than the size of the BECs, then they will remain in the harmonic regime of the waveguide. Both will also deviate identically when moving, ensuring good overlap when they come to rest at the end of the drive sequence. We can use κ as a convenient parameter in the expression for the turning point:

$$\begin{aligned} x(t = \hat{T}) &= \frac{2\pi K_a}{\hat{\Omega}^2} \\ &= 2\pi\kappa \frac{\omega_\rho^2 - \hat{\Omega}^2}{\hat{\Omega}^2}. \end{aligned} \tag{6.78}$$

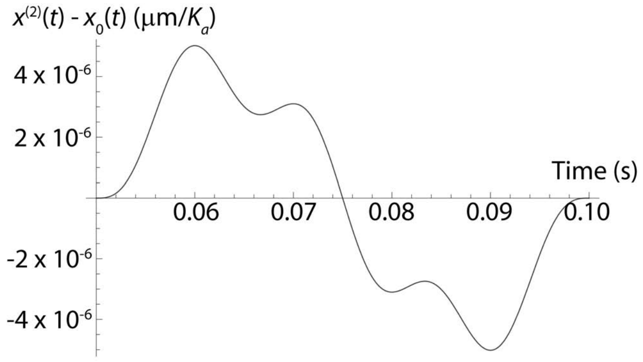

Figure 6.8: Deviation of BEC center from trap center during return trip, for $\omega_\rho = 2\pi \times 80$ Hz and $\omega_z = 2\pi \times 10$ Hz.

6.5.4 Enclosed area

Recall that in the axial direction, the clouds undergo simple harmonic motion:

$$z(t) = \pm z_0 \sin \omega_z t = \pm \frac{2n\hbar k_0}{M\omega_z} \sin \omega_z t, \tag{6.79}$$

where n is the diffraction order of the beamsplitter. We may combine this equation with Eq. (6.67) to find

$$x(z) = \frac{K_a \hat{\Omega}}{\omega_\rho(\omega_\rho^2 - \hat{\Omega}^2)} \sin\left(\frac{2\omega_\rho}{\hat{\Omega}} \sin^{-1}\frac{z}{z_0}\right) + \frac{2K_a}{\hat{\Omega}^2} \sin^{-1}\frac{z}{z_0} + \frac{K_a \omega_\rho^2}{\hat{\Omega}^2(\hat{\Omega}^2 - \omega_\rho^2)} \sin\left(2\sin^{-1}\frac{z}{z_0}\right), \tag{6.80}$$

valid for $0 \le t \le \hat{T}/2$. The full path traveled by both BECs is shown in Fig. 6.9. The total enclosed area is

$$\begin{aligned}
\mathbf{A} &= 4\int_0^{z_0} \left[x\left(\frac{\hat{T}}{2}\right) - x(z)\right] \hat{\mathbf{y}} dz \\
&= \left[\frac{4Kz_0}{\hat{\Omega}^2} - \frac{4Kz_0}{3\hat{\Omega}^2}\left(3\pi + \frac{32\omega_\rho^2}{\hat{\Omega}^2 - 4\omega_\rho^2}\right)\right] \hat{\mathbf{y}} \\
&= \frac{8Kz_0\omega_\rho^2}{3\omega_z^2(\omega_\rho^2 - \omega_z^2)}\hat{\mathbf{y}} \\
&= \frac{8\kappa z_0 \omega_\rho^2}{3\omega_z^2}\hat{\mathbf{y}}.
\end{aligned} \tag{6.81}$$

6.5.5 Parameter estimates for enclosed area

We conclude this chapter by estimating the enclosed area that will be attainable for our expected $(80, 80, 10)$ Hz trap. We want to limit κ such that it is not too much larger than the oscillator length ρ_0. A BEC with repulsive atomic interactions will always have a larger transverse size than the oscillator length, so the condition $\kappa/\rho_0 \simeq 10$ keeps the deviations to a range not too much larger than the size of the BEC. For ^{87}Rb $\rho_0 = 1.2\ \mu$m, so we require

$$K_a \simeq 10 \times \rho_0(\omega_\rho^2 - \omega_z^2) = 3\ \text{m/s}^2. \tag{6.82}$$

The extent of the transverse motion is therefore 1.2 mm. The enclosed area is $\mathbf{A} = 0.4n\hat{\mathbf{y}}\ \text{mm}^2$, where n is the order of the optical beamsplitter. It should therefore be possible to demon-

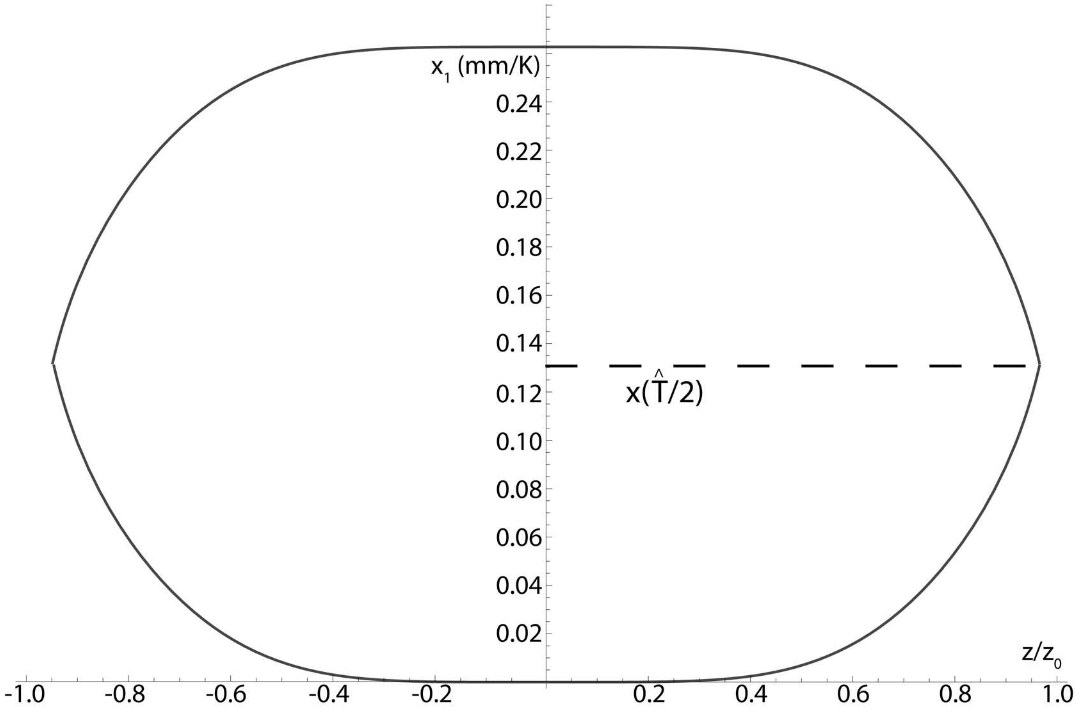

Figure 6.9: Trajectory of BECs in translating guide. Trap parameters are $\omega_\rho = 2\pi \times 80$ Hz and $\omega_z = 2\pi \times 10$ Hz.

strate a BEC Sagnac gyroscope with a sensitivity within an order of magnitude of the eventual performance goal of π rad of phase shift at Ω_{Earth}.

Using these values of K_a and ω_z, we can calculate the amplitude of the velocity of the trap center:

$$K_a/\hat{\Omega} = 24 \text{ mm/s}. \tag{6.83}$$

Examining the shape of the plot of $v_c(t)$ [Fig. 6.7(b)], we see that v_c spends a significant amount of the duration of the experiment moving at $v_c \approx K_a/\hat{\Omega}$. For our proposed wire pattern, at this velocity the perturbation drive frequency is $\tilde{\Omega} = 2$; we will be driving the breathing mode precisely on resonance. Fortunately, the amplitude of this mode will not become large for our proposed wire pattern. We see in Table 6.2 that the normalized amplitude of the breathing mode when driven on resonance is $0.097\check{T}$ for drive duration $\check{T}$. Again examining Fig. 6.7(b), we see that the drive frequency should only be near resonance for approximately 20 ms around the periods of peak velocity. The amplitude of the breathing mode should therefore not increase much past $\delta\lambda_i = 0.002$. This amplitude is small enough that it should have no noticeable effect on the experiment.

Chapter 7

Gyroscope apparatus: Design and construction progress

This chapter describes the design and construction of a new, compact apparatus for Sagnac gyroscope experiments. The heart of the apparatus is a new atom chip patterned with an array of parallel wires, capable of carrying out the translating waveguide idea proposed in the previous chapter. The new apparatus built around that chip has been designed to meet the requirements given at the end of Chap. 5 for a successful gyroscope. It has the optical access needed to control the angle of the optical standing wave with respect to the waveguide axis, allowing for axial traps of sufficiently high frequency for our purposes. It will be able to produce BECs with a cycle time of only a few seconds, allowing in only a few hours the collection of 1000 point data sets. Finally, it is small and light enough to be placed on a rotary table. Once operating, the apparatus will be capable of taking real rotation rate measurements.

The design and operation of similar compact BEC machines has been pursued by our group over the past decade [18, 52, 53]. The goal of this chapter is therefore not to provide a full manual for the production of BECs in compact systems. Our purpose is instead to detail the unique aspects of this new apparatus, as well as the new techniques and lessons learned during its construction. Significant elements of this updated system (magnetic field coils and vacuum system mount) were designed by Evan Salim.

There are major differences in design between the large Michelson apparatus and our compact systems. All successful BEC vacuum systems must execute a balancing act: The same system must be used to both capture a large number of atoms, and then hold those atoms in a trap long enough to evaporatively cool to degeneracy. Quick trap loading can be achieved in a vacuum chamber containing a relatively high vapor pressure of the atom of interest. However, the already trapped atoms will collide with any remaining warm vapor, heating the trapped atoms enough to cause them to escape. In the Michelson apparatus, this problem was solved by using a multi-chamber vacuum system. Rubidium atoms were initially collected from vapor into a MOT in one chamber, and then magnetically transported through a tube to an evaporation chamber. This chamber had only a small background pressure of Rb vapor, since untrapped atoms were unlikely to diffuse through the long tube. The compact apparatus also uses a multi-chamber system, but transport through a long tube is an impractically large and slow connection solution. Instead, the two chambers share a common wall, pierced by only a small pinhole. In the first chamber, a two-dimensional MOT (2D-MOT) collects ^{87}Rb atoms from a vapor. This 2D-MOT creates a beam of cold atoms that is aligned to pass directly through the aperture into the second chamber. Warm atoms not in the beam are unlikely to diffuse through the pinhole, so the pressure in the second chamber is significantly lower than in the first. In this chamber, the atoms in the beam are captured in a traditional three-dimensional MOT (3D-MOT). The atoms are subsequently loaded into a microtrap generated by an atom chip for evaporation to BEC. The chip forms one of the walls of the chamber, allowing the system to be smaller than competing designs. The use of ballistic transport between the chambers allows us to dispense with the water-cooled magnetic field coils and the servo-controlled track used for magnetic transport in the old system.

A further reduction in size and cycle time is achieved by dispensing with the Michelson experiment's use of a "macro" trap to evaporatively cool the atoms before delivery to the microtrap. As was explained in Sec. 2.1, the higher trap frequencies that can be practically obtained with microtraps allow efficient evaporative cooling in a significantly shorter time. The roadblock in the way of directly loading a microtrap from a MOT is the low trap depth of microtraps (typically a few hundred microkelvin), combined with the small size of the trap (typically less than 100 μm in radius). Atoms compressed directly from a MOT into the small volume of a microtrap would be far too hot to be confined. The solution in the Michelson apparatus was to slowly (about 1 min) evaporatively cool the atoms in a large volume trap generated by permanent magnets. The approach followed in our compact apparatus is to add a stage of polarization gradient optical cooling after the MOT, cooling the atoms sufficiently so that they can be directly loaded into a chip trap without any previous evaporation. The time allocated for evaporative cooling is thereby cut from over a minute to a few seconds.

In the remainder of the chapter, we detail the new apparatus component-by-component.

7.1 Lasers

The BEC production recipe developed in [52] requires four wavelengths of laser light: cooling and hyperfine repump light for optical cooling and trapping, light for optical pumping, and light for absorption imaging. Our system uses three temperature-stabilized external cavity diode lasers (ECDLs) to generate these wavelengths. The cooling light is produced by an ECDL (JILA design [54], Hitachi HL7851G diode) and amplified by a tapered amplifier (JILA design, SDL diode) to 500 mW. The repump light is produced by a commercial ECDL (New Focus Vortex) and amplified by a slave diode laser (JILA design, Sharp GH0781JA2C diode) to 100 mW. Some of this laser's light will be used to generate the standing wave beamsplitter. The pump and imaging (or "probe") light is generated by the third ECDL, producing 30 mW of power. The ECDLs were all recycled from the Michelson system. Figure 7.1 is a schematic of the system.

7.1.1 Frequency control

Frequency stabilization of the three lasers is obtained by peak-locking the ECDLs to crossover peaks in the saturated absorption spectrum of the $5S_{1/2} \rightarrow 5P_{3/2}$ transition of ^{87}Rb, located near 780 nm. The lock servos control both the current and grating orientation. The cooling and pump/probe lasers are locked to the $F = 2 \rightarrow F' = 2,3$ crossover, while the repump laser is locked to the $F = 1 \rightarrow F' = 1,2$ crossover (primes indicate excited electronic

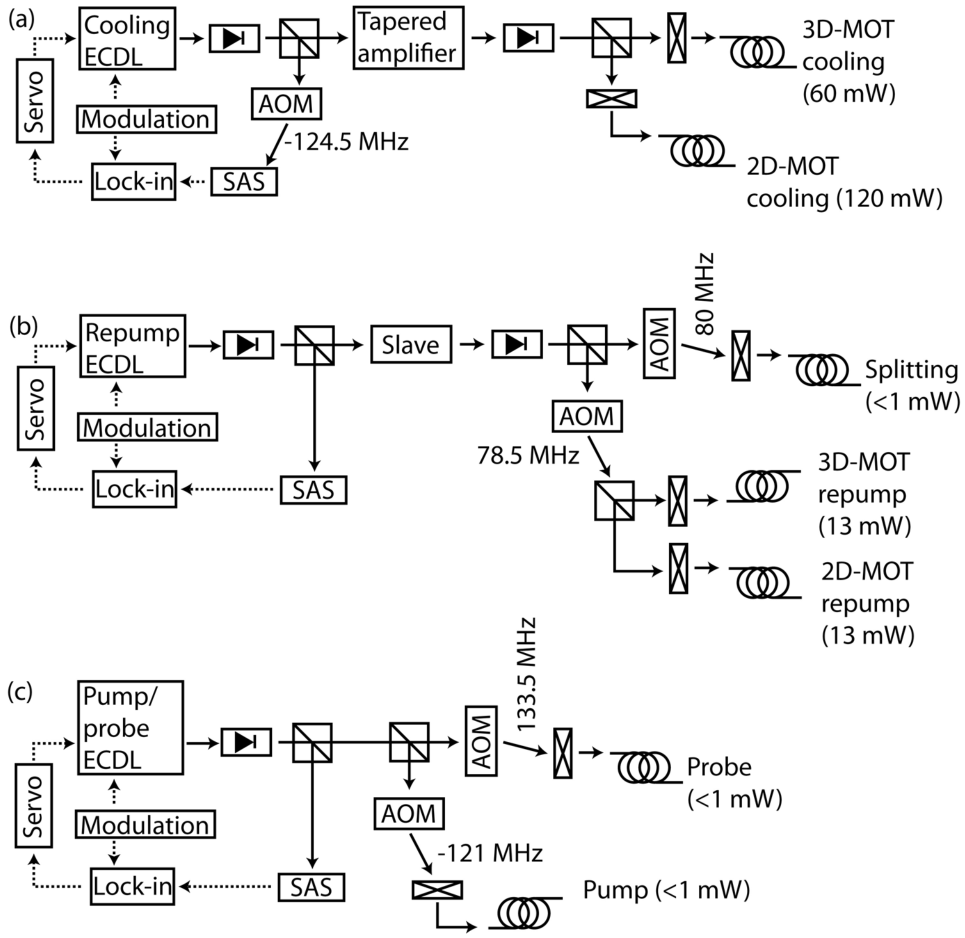

Figure 7.1: Schematic of laser system. (a) Cooling laser, (b) repump/beamsplitting laser, (c) pump/probe laser. Optical isolators are shown as diodes. Mechanical shutters are shown as boxes with an "x" through the center. Boxes marked "lock-in" are lock-in amplifiers, and those marked "SAS" denote saturated absorption spectroscopy. Optical paths are marked as solid lines, electrical signals as dashed lines. All beams are coupled into single-mode, polarization-maintaining optical fibers.

states). Modulation for the peak-lock is applied to the laser diode current. The lock-in amplifiers, frequency servo circuits, and temperature controllers are the same as those used in the Michelson apparatus, with minor modifications to remove ground loops from the power system.

We use acousto-optic modulators (AOMs) to shift the light to the precise frequencies required. The modulation frequencies used are shown in Fig. 7.1. The AOM shifts place the repump and splitting beams at the $F = 1 \rightarrow F' = 2$ resonance, the probe beam at the $F = 2 \rightarrow F' = 3$ resonance, and the pump beam 12.5 MHz to the blue of the $F = 2 \rightarrow F' = 2$ resonance. The cooling laser is stabilized 9 MHz to the red of the $F = 2 \rightarrow F' = 3$ resonance, but this detuning must be increased during MOT compression and polarization gradient cooling. We can adjust it by unlocking the cooling laser and applying a calibrated voltage to the piezoelectric actuator controlling the angle of the external cavity's grating. The servo is relocked after the laser cooling stages are finished.

7.1.2 Shutters and optical power control

All of the laser beam lines are controlled with commercial mechanical shutters, with the AOMs providing adjustable control over beam power. However, the mechanical shutters are not fast enough to generate sufficiently short pulses for the probe and beamsplitting beams. In these beams, the AOM is used as a high-speed, low-extinction shutter in series with the mechanical shutter. Pulses are generated by opening the mechanical shutter a few milliseconds before quickly pulsing the AOM's acoustic wave; the mechanical shutter is closed after the pulse so that none of the light leaking through the AOM in its off state reaches the atoms.

7.1.3 Optical fibers

Since our goal is to construct a rotating system, the laser beams cannot be delivered to the vacuum system through free space. We instead couple all seven beams into single-mode optical fibers. The fibers used are Corning PANDA PM 850 fibers that have been angle-polished on at least one side. These fibers provide a polarization- and intensity-stable, flexible path from the lasers to the rotating system.

7.2 Vacuum system

The vacuum system used in the new apparatus (see Fig. 7.2) is a standard design that is used in all of our group's BEC experiments; the only difference between the systems is the specific wire layout on the atom chip. These systems are designed to be quickly and easily swapped out from the surrounding optomechanics if a chip with a different wire layout is needed for future experiments. As the vacuum systems have previously been described in detail in [18], we will only describe here recent changes in design and construction.

The major design change for the gyro vacuum system is that the glass cell that comprises most of the BEC chamber has been anti-reflection (AR) coated. Recall that the Michelson experiment utilized a fixed, in-vacuum retro-reflector to establish the optical standing wave for beamsplitting. The fixed angle of the optic with respect to the guide wire placed a limit on the acceptable angle between the waveguide and the optic, thus limiting the practical axial confinement. In order to allow for greater flexibility in this parameter, in the gyroscope apparatus we will replace the fixed optic with a mirror on an adjustable mount, placed outside of the vacuum chamber. In order to form an acceptable standing wave, the reflected component of the beam must contain almost the same power as the incident component. Therefore the wall of the cell that sits between the retro-reflector and the trapped atoms must be AR coated.

The process for assembling the vacuum systems remains mostly unchanged, though we have modified the recipe for bonding the atom chip to reduce damage to its delicate wires. The anodic bonds [55] that we use are typically done at high temperature (400°C) to increase the bond strength. We have since discovered that bonding the chip at that temperature can cause the Au wires patterned on the side of the chip facing ambient pressure to deform (see Fig. 7.3). The formation of an anodic bond requires the application of steady pressure between the two pieces to be bonded, but Au is susceptible to deformation under negligible applied pressure at high temperatures [56]. We have therefore reduced the temperature for bonding the chip

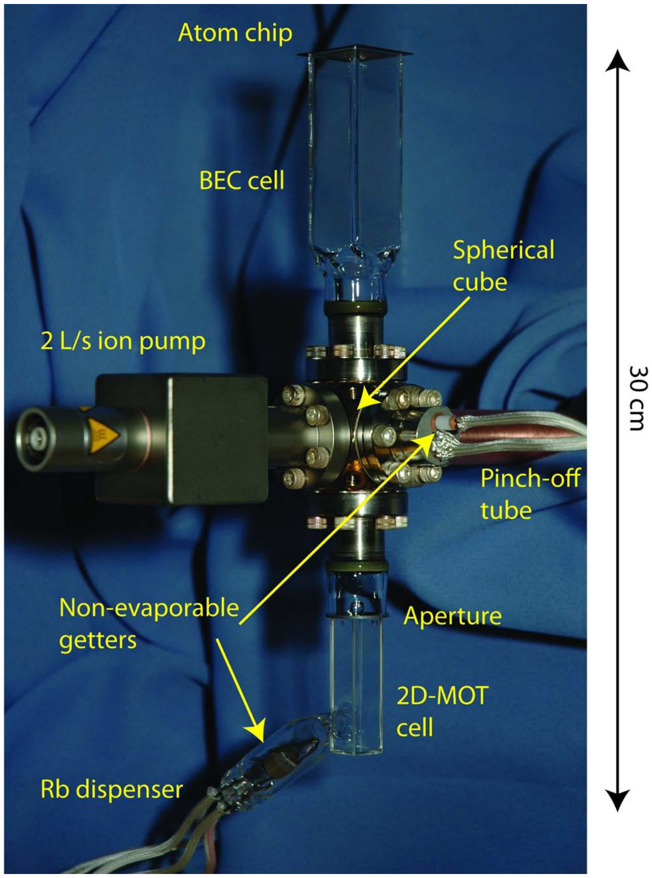

Figure 7.2: (Color). Annotated photograph of an assembled vacuum system. Ion pump magnets are not shown. Also not shown is the mounting plate that bolts to the spherical cube.

to 325°C. At this temperature no wire deformation is evident, and the resulting lower bond strength has not caused any problems.

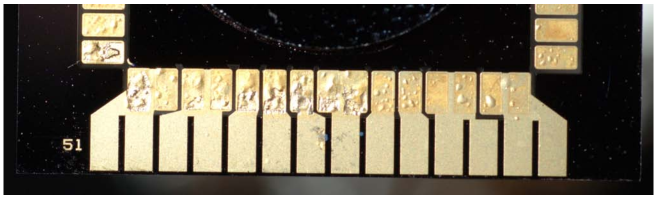

Figure 7.3: (Color). Deformation of Au wires on back of chip bonded at 400°C.

The recipe we use to pump and bake the assembled system is substantially similar to previous methods, though our procedures for detecting and sealing vacuum leaks have advanced. We use a He detector to check for leaks before beginning the bake. There exists a simpler method of leak detection, in which one sprays clean solvent on suspected locations of leaks. If there is a leak, the solvent will shortly afterwards register on the pressure gauge. However, this elegant method has not proved sensitive enough to find tiny leaks in the chip before the system has been subjected to a time-consuming bake. These leaks are extraordinarily difficult to permanently seal, so leaky chips must often be discarded. We find that it is better to learn whether a chip is fatally leaking before spending the time to bake the system to which it has been bonded.

The only leak sealant with which we have had any lasting success when applied before a system bake is Vacseal, a silicone resin suspended in a volatile solvent. Vacseal's product literature claims that it can be baked to 400°C before failing [57], although we have found that sealed leaks will often re-open during the cool-down of the system. There is evidence in published work that Vacseal should never be baked above 250°C [58]. We have therefore limited the bake of any system treated with Vacseal to this temperature; such systems likely do not achieve the lowest possible pressures.

The chip can also develop leaks while the BEC system is cooling down after the bake. The leaks can usually be located by the solvent method described previously. We have found that sealing these post-bake leaks with the application of Vacseal is possible, but difficult. An alternative sealant is Glyptal 1201B, an alkyd resin paint with a very low vapor pressure [58]. Chips sealed with Glyptal should not be exposed to temperatures in excess of 135°C for extended periods of time, so Glyptal may not be used before a system is baked.

It should be noted that we have not yet achieved BEC in the new system, so these leak sealing techniques should not be regarded as having been fully evaluated. Leaks have fortunately become less of a problem with the delivery of a new production run of atom chips, as the fabrication process now uses a technique less prone to failures. This is the best possible solution to the problem, as no leak sealant is perfect.

A final change to the vacuum system preparation process has been made to the terminal step, in which the BEC system is removed from the pumping station by pinching off the Cu tube with a pair of rounded steel jaws. Before pinch off, the tube must be cleaned of all oxides that accumulate during the bake. We have added a step to the preparation, in which we lightly coat the tube with clean machine oil just before the pinch. The oil allows the jaws to slide smoothly over the tube's surface.

7.3 Optomechanics structure

The gyro optomechanics structure supports all of the components needed to make a BEC other than the lasers, electrical power supplies, and control system. The structure weighs approximately 65 kg, and occupies a 60 cm by 60 cm footprint. This section details its design and construction.

The base of the structure is an air bearing rotary table, Precitech model RT200 (Fig. 7.4). Air bearings provide smooth, low-friction motion and are therefore quite suitable for precision rotation measurements. The RT200 has a 200 mm diameter table and an axial load capacity of 226 kg; care must be taken to ensure that the apparatus to be built on top of the table is well balanced to keep the load as axial as possible. The unit requires a regulated supply of clean, dry compressed air at 50 psi (0.34 MPa) to operate. The compressed air supplied to our lab has sufficient pressure, but it must be filtered (Norgren Excelon F72G-2AN-AL1) and then processed through an oil and water vapor separator trap (Norgren F64B-2AN-AT0). A second filter and a pressure regulator are in the supply line between the trap and the rotary table.

Figure 7.4: (Color). Rotary table, 200 mm diameter.

The 200 mm diameter rotary table is large enough to directly support a custom-made optomechanical structure for BEC production (for an example, see [53]), but we decided to save on materials and production costs in this apparatus by using mostly off-the-shelf hardware. This approach requires a larger surface area for the optical layout, which we support with a 60 cm by 60 cm industrial grade breadboard (Newport). The board combines a steel working surface with a trussed honeycomb core, providing a stiffer foundation with more vibration damping at a lower weight than would a solid metal plate.

The breadboard must sit precisely at the center of the rotary table to prevent off-axis loads from damaging the air bearing. Our breadboard has a tapped tube welded vertically into its structure at its precise center (Newport's "Microlock" system). A machined Al cylinder that is just under 38 mm in diameter is bolted into the Microlock tube on the underside of the board. This cylinder fits snugly inside the 38 mm diameter shaft that runs down the center of the rotary table (visible in Fig. 7.4). To mate the two pieces together, we first raise the breadboard on jacks. We then carefully position the rotary table, using the cylinder and the shaft to properly locate the relative position. We finally lower the breadboard to rest on top of the rotary table. The weight of the apparatus is enough to hold the pieces snugly together. The breadboard is typically not mated to the rotary table while we are optimizing the experiment.

The vacuum system and optics for the 2D-MOT are mounted directly on the breadboard. A solid Al baseplate for the BEC chamber's optical system is mounted 18 mm above the breadboard on a set of 4 pedestals (see Fig. 7.5). In order to maximize the 45.72 cm by 45.72 cm baseplate's mechanical resonance frequency, the pedestals are placed along the breadboard's diagonals, halfway between the center and the corners. A hole cut in the plate allows a compact camera mounted on the lower breadboard to record images of atoms trapped in the BEC chamber.

7.4 Double MOT

The job of the 2D-MOT is to produce the greatest possible flux of cold atoms into the ultrahigh vacuum BEC region of the system. To obtain a high flux, we use a pair of perpendicular, retroreflected, elliptically shaped cooling beams to take maximal advantage of the 25 mm by 10 mm size of the 2D-MOT cell. The total cooling power in each beam is approximately 50 mW, with major diameter 24 mm and minor diameter 7.1 mm ($1/e^2$).

A top view of the 2D-MOT optics is shown in Fig. 7.6. Light from both the 2D-MOT cooling and repump fibers is collimated with air-spaced doublet collimators (Thorlabs) and combined at a polarizing beamsplitter (PBS) cube. A confocal cylindrical telescope ($f = -38.1$ mm and $f = 130$ mm) expands the beam along the vertical direction. The retroreflectors for both beams each consist of a quarter-wave plate cemented to a dielectric mirror. Approximately 10% of the cooling light is picked off just after the collimator for use as a vertically aligned "push" beam. When correctly aligned with the 2D-MOT, the push beam forces most of the MOT's flux to travel upwards into the BEC chamber. Control over the push beam's power is provided by a variable attenuator consisting of a half-wave plate and a PBS; the excess light is

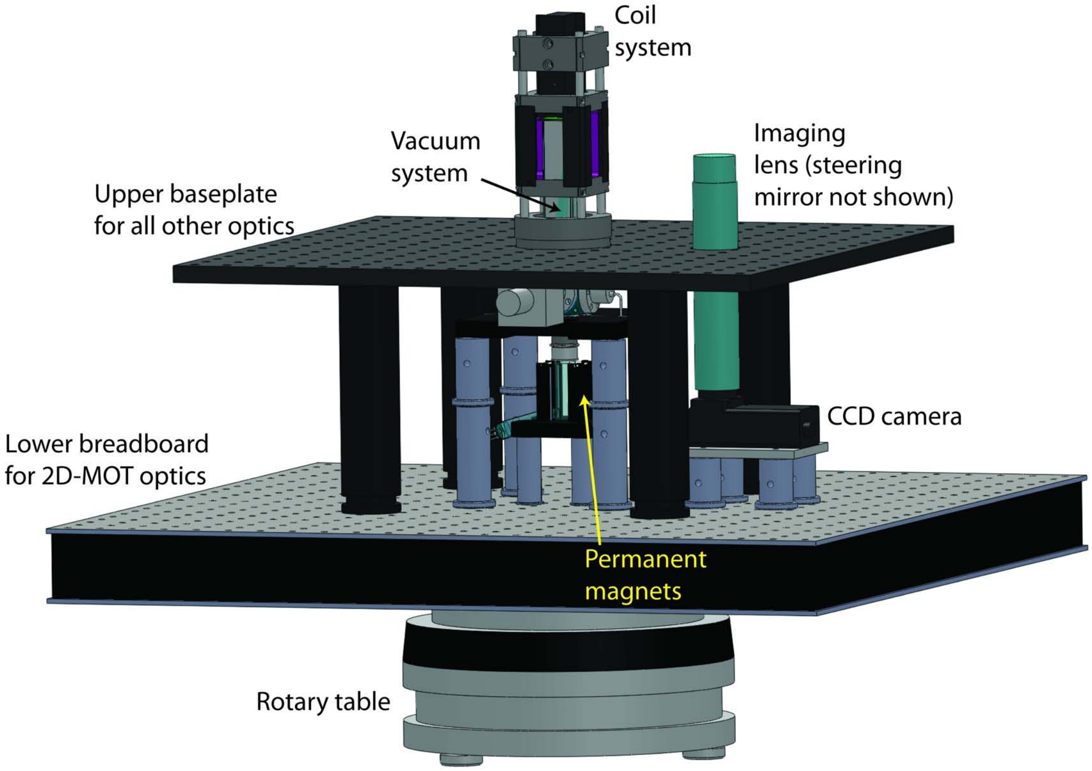

Figure 7.5: (Color). Schematic view of optomechanics structure, shown without optics.

dumped into a black piece of paper attached to the PBS's unused output face.

The two-dimensional quadrupole magnetic field for the 2D-MOT is generated by four NdFeB permanent magnets (Magnetic Component Engineering alloy N3578). These magnets have a square cross section with 1 mm sides, and are 40 mm long. The magnets are poled perpendicular to their length. They are mounted vertically with respect to the 2D-MOT cell, and placed at the corners of a square measuring 18 mm on a side. The sides of the square are normal to the propagation direction of the MOT beams. The resulting field gradient is between 30 and 35 G/cm.

A top view of the optics for the 3D-MOT is shown in Fig. 7.7. The total cooling power for this MOT is approximately 60 mW, split among three retroreflected beams. Both the repump and cooling beams are collimated with $f = 75$ mm doublet lenses, resulting in a 15 mm beam diameter ($1/e^2$). Power balancing between the beams is provided by a set of half-wave plate and PBS pairs. As explained in [18], our 3D-MOT does not use the traditional 90° angle between the cooling beams. One beam (the "horizontal" beam) is aligned parallel to the baseplate as it passes through the glass cell. The other two beams (the "angled" beams), which pass through the cell in the plane normal to the horizontal beam, are aligned at an elevation angle of 22° with respect to the plate. This configuration allows us to make a MOT significantly closer to the atom chip than would be possible with beams aligned at 90° (see Fig. 7.8). The retroreflectors for the angled beams are essentially identical to those used in the 2D-MOT, but the horizontal beam's retroreflector has a PBS in the beam path between the quarter-wave plate and the mirror. The quarter-wave plate is aligned so that all of the MOT light passes directly through the PBS. This more complicated reflector allows us to overlap the horizontal beam with the optical pumping beam; see the next section for more details.

The three-dimensional quadrupole field for the 3D-MOT is generated by a pair of rectangular anti-Helmholtz coils, oriented perpendicular to the horizontal MOT beam. These coils provide a gradient of 12 G/(cm A). The MOT coil pair is held in a machined Al mount, which slides over the BEC glass cell on a set of four steel rails. The rails are bolted to a collar, which

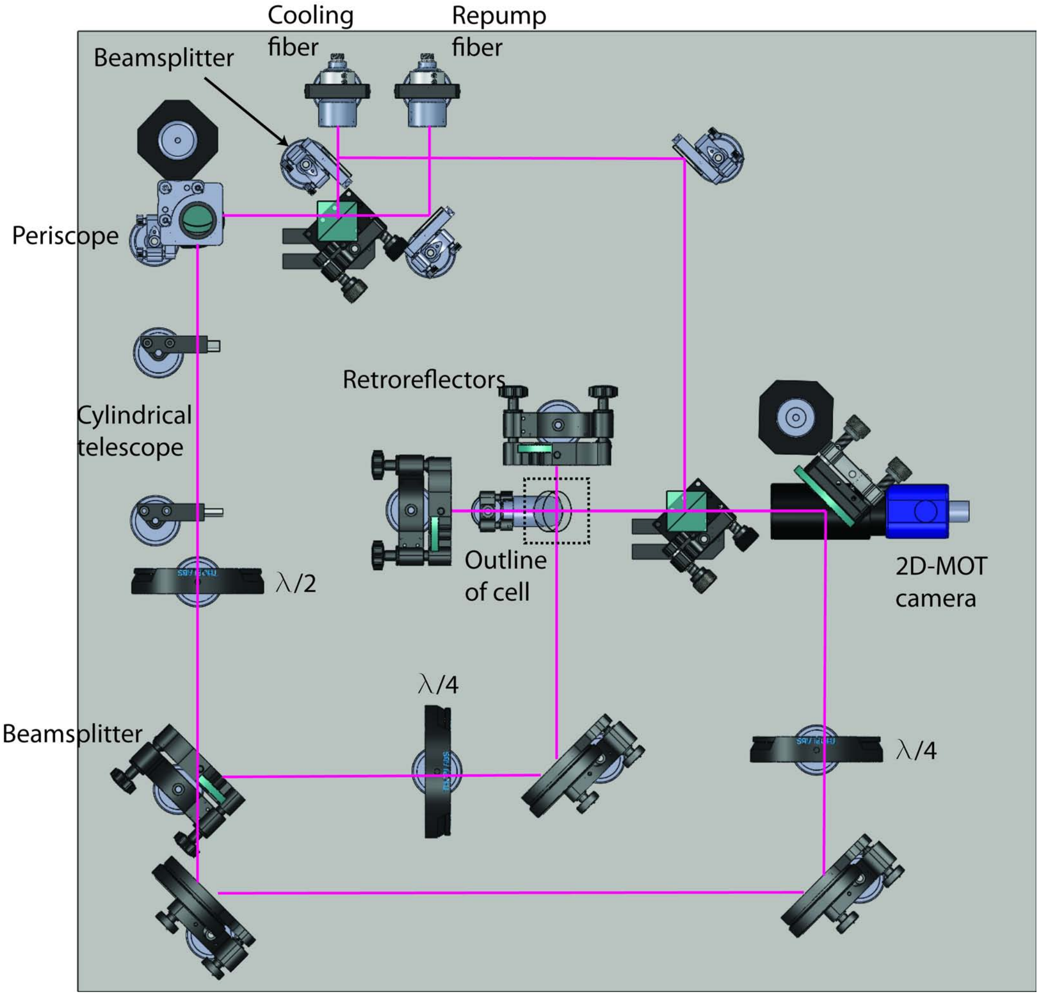

Figure 7.6: (Color). Optical layout of 2D-MOT. Magenta lines show beam paths.

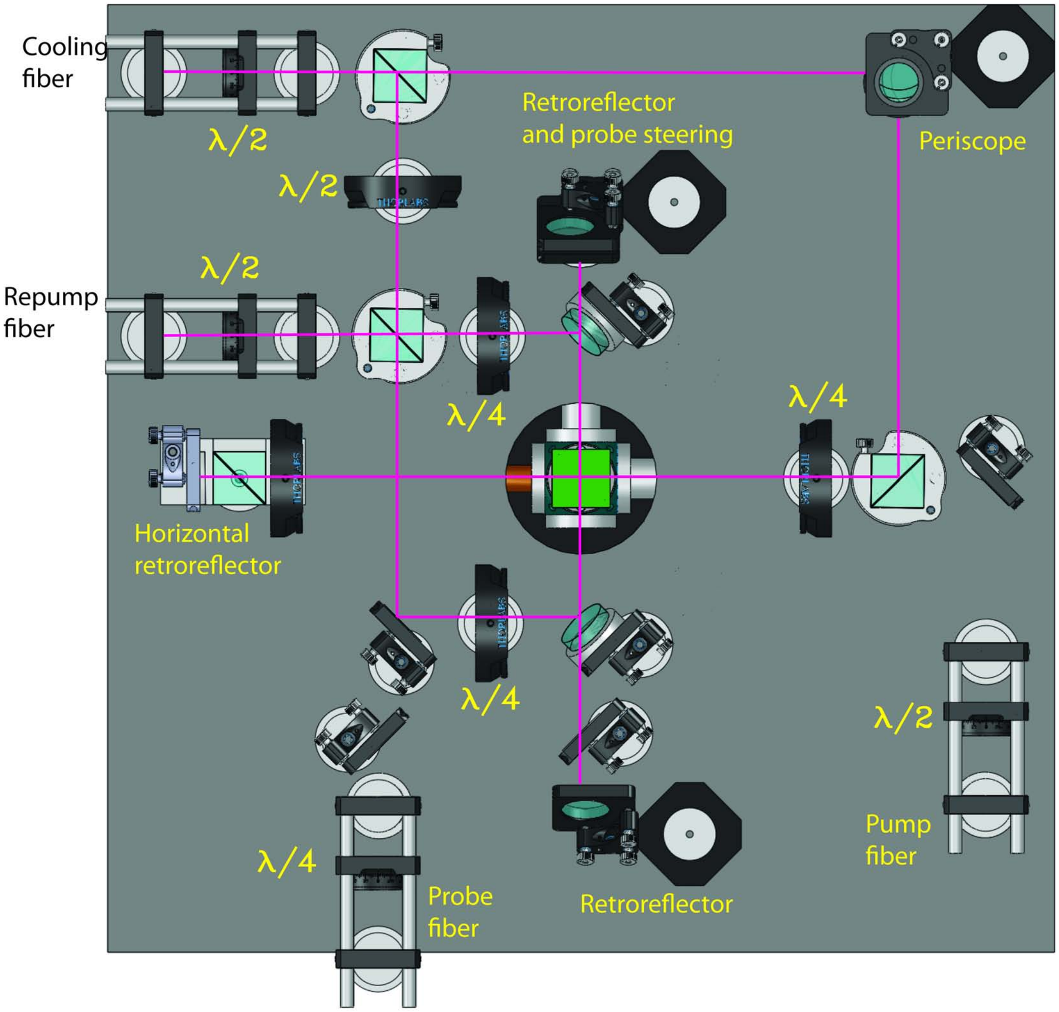

Figure 7.7: (Color). Optical layout of upper baseplate. 3D-MOT beam paths are shown in magenta. The horizontal beam passes from right to left across the center of this diagram.

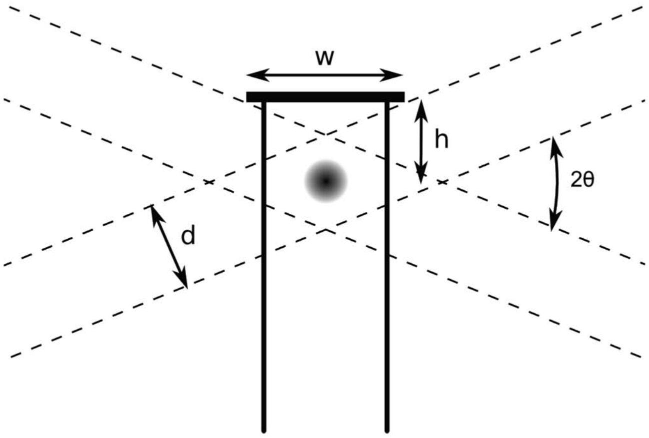

Figure 7.8: View of angled 3D-MOT along axis of horizontal beam. Reducing the angle θ allows the separation between the MOT and the atom chip h to be reduced without clipping the beams on the edge of the atom chip [18].

is itself bolted to the upper corners of the vacuum system's spherical cube. See Fig. 7.9. The coil mount also carries 3 pairs of rectangular Helmholtz coils to generate bias fields along the three Cartesian axes of the apparatus.

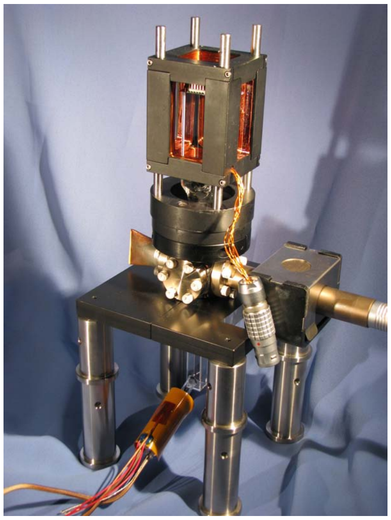

Figure 7.9: (Color). Mounted vacuum system with MOT and bias coils installed on rail system.

The current for the MOT coils is generated by a commercial linear, unipolar power supply (Kepco ATE). For the bias coils, we need the flexibility of bipolar supplies in order to generate the full range of microtraps. A trio of Kepco bipolar operational amplifier power supplies (BOPs) provides the needed bipolar behavior. However, they are unable to operate in a stable manner while driving current through inductive loads. The complex impedance of an inductive coil pair is

$$Z_{\text{coil}} = R_{\text{coil}} + i\omega L, \tag{7.1}$$

where ω is the angular frequency of a signal sent through the coils. At sufficiently high inductances, the imaginary part of the impedance becomes significant at frequencies within the bandwidth of the BOP power supply's servo. Instead of supplying DC current, the BOPs oscillate when driving our 0.5–1 mH coil pairs. A solution to this problem is to add a Zobel network [59] in parallel to the coil, which consists of a resistor and a capacitor in series. The total impedance is

$$Z = \frac{R_{\text{coil}}R_{\text{Zobel}} + L/C + i[\omega R_{\text{Zobel}}L - R_{\text{coil}}/(\omega C)]}{R_{\text{coil}} + R_{\text{Zobel}} + i[\omega L - 1/(\omega C)]}. \tag{7.2}$$

If $R_{\text{Zobel}} = R_{\text{coil}}$ and $C = L/R_{\text{coil}}^2$, then the impedance of the combination of the coil and the Zobel network is real and equal to R_{coil}. For our bias coil pairs, $R_{\text{coil}} \approx 2\ \Omega$, which sets $C =$ 125–250 μF. As this capacitance is larger than that of easily obtainable small capacitors, we typically set $C = 10\ \mu$F and set R_{Zobel} to minimize the imaginary part of Eq. (7.2) for that choice of C. We then optimize the choice of R_{Zobel}, monitoring the actual stability of the power supply with a Hall probe. We find $R_{\text{Zobel}} = 17\ \Omega$ works quite well.

We optimize the double MOT to obtain a large 3D-MOT cloud that loads quickly. We can measure both the number of atoms and loading time by monitoring the fluorescence of the 3D-MOT with a photodiode. The loading time is quite sensitive to the alignment of the 2D-MOT with the aperture, and to the alignment of the push beam. We use an inexpensive infrared-sensitive security camera to monitor the shape of the 3D-MOT while we are optimizing the beam alignment; typically, an irregularly-shaped MOT is not desirable. For a non-leaking vacuum system, we are usually able to load a few hundred million to a few billion atoms into the 3D-MOT in fewer than 3 s.

7.5 Transfer to chip trap

The procedure that we follow to transfer cold atoms from the 3D-MOT into a chip trap is identical to that explained in detail in [18]. We will therefore only briefly review the steps in the process. We concentrate on a description of the new gyroscope atom chip, which incorporates the array of parallel wires described in the previous chapter.

7.5.1 Loading the "big Z" trap

The next major step in the experiment is to load the atoms trapped in the 3D-MOT into a magnetic trap. In order to reduce the cooling that will have to be later carried out by evaporation, we strive to maximize the phase-space density of the magnetically trapped atoms. In pursuit of that goal we must reduce the spatial size and temperature of the cloud, while maximizing the number of trappable atoms in it.

A compressed MOT (CMOT) stage serves to shrink the spatial extent of the atomic cloud. As soon as the 3D-MOT has filled, we unlock and detune the cooling laser further to the red by an additional two linewidths. We simultaneously reduce the repump power by greater than 90%, using that laser's AOM. The reduced re-radiation pressure allows the cloud's size to drop from about 1 cm to about 1 mm. The CMOT duration is approximately 50 ms.

To reduce the temperature of the cloud, we follow the CMOT with a stage of polarization gradient optical molasses cooling (PGC). In this stage, the cooling laser is further detuned, now to a total of more than 11 linewidths from resonance. The MOT quadrupole field is turned off, and the bias coils are used to cancel out ambient magnetic fields. Temperatures in the range of 40 μK are easily obtained after only a few milliseconds of PGC. The cooling efficiency of PGC is in this case limited by the density of the compressed cloud of atoms. Lower temperatures (below 10 μK) can be obtained when the MOT load is kept small. The ideal balance between temperature and number of atoms after PGC is experimentally determined.

After PGC, the cloud of atoms is optically pumped into the $|2, 2\rangle$ ground state by the pump laser beam, which is set to σ^+ polarization with respect to an applied uniform magnetic field. The beam must not be retroreflected by our standard quarter-wave plate/mirror reflectors and sent back through the atoms. The polarization of the reflected beam would be σ^- with respect to the bias, and would tend to pump the atoms into the wrong state. Our solution to this problem is shown in Fig. 7.7. The pump beam is collimated and then combined with the horizontal MOT beam at a PBS (shown at right center of figure). The following quarter-wave plate converts the two beams of perpendicular linear polarization into two circularly polarized beams of opposite helicity (with respect to the direction of propagation). On the far side of the vacuum system, a second quarter-wave plate is aligned to convert the cooling beam into light polarized parallel to the baseplate. This beam passes directly through a second PBS and is retroreflected back towards the atoms. On the other hand, the pump beam is converted to light polarized perpendicular to the baseplate. This light is reflected by the PBS and blocked by a piece of black paper attached to its side output port.

The compressed, cooled, and pumped cloud of atoms is at this point ready to be magnetically trapped. Our initial "microtrap" is actually generated by a large Z-shaped wire (see Sec. 2.1.3) that is mounted directly above the chip, just outside of the vacuum system. The distance L_{H} between the "legs" of the Z is 27 mm. A significant amount of current is required to make a trap capable of supporting against gravity more than 18 mm away from the trapping wire (h in Fig. 7.8 is approximately 17 mm). This problem was solved in [18] by running > 100 A through 5 Z-shaped wires held together in an Al block and connected in series. In the new apparatus, we have replaced this high-current "big Z coil" with a version using approximately 30 wires (see Fig. 7.10). This coil allows us to use only 20 A to produce a similar trap.

7.5.2 Transport to chip height

Once the atoms have been caught in the big Z trap, they are transported up to the chip by simply ramping down the big Z current [recall that the distance between the wire and the field minimum is proportional to the current, Eq. (2.4)]. If the transverse bias is not adjusted, the trap becomes tighter in the transverse direction as the trap is pulled towards the chip [Eq. (2.9)]. However, as the distance from the wire to the trapped atoms $d + y_0$ becomes very small with respect to L_{H}, the trap loosens in the axial direction [Eq. (2.24)]. We therefore wrap an additional set of wires over the legs of the Z coil (labeled as "compression wires" in Fig. 7.10) and use them to effectively increase the axial trapping current as the atoms approach the chip. The transport ramp is usually completed in about 400 ms.

7.5.3 Gyroscope atom chip

The gyroscope chip is shown in Fig. 7.11. The central feature is an array of 40 parallel wires, placed at a spacing of 150 μm. Each wire is 80 μm wide. This chip is a realization of the

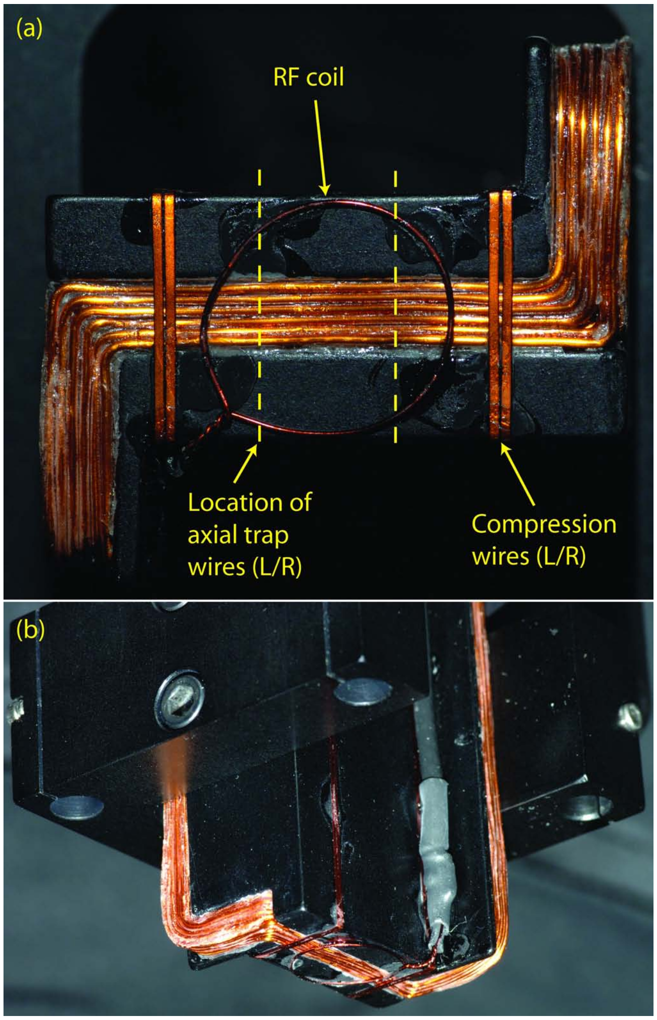

Figure 7.10: (Color). Views of the big Z assembly. (a) View from below, (b) angled view. This assembly is lowered down to just above the atom chip on the rails that also carry the MOT/bias coil assembly.

design proposed in Sec. 6.4. We plan to initially capture and evaporate the atoms to BEC in a trap generated by a wider 100 μm wire, crossed by a T wire (this wire appears above the array of parallel wires in the figure). These wires are connected to external power supplies through hermetic electrical "vias" that pass through the chip substrate. Longer-range axial confinement than can be generated by the T wire is provided by a selection of H-type wires patterned on the back of the chip [the vertical traces in Fig. 7.11(b)].

We make electrical connection to the chip's more than 100 contact pads by attaching commercial connectors to the pads with conductive epoxy (EPO-TEK E2101). This Ag-bearing adhesive is used in place of standard electrical solder, as Sn to Au solder joints are brittle and age poorly [60]. The connectors used for the parallel wire array have a pitch of 500 μm (Hirose FH19SC) and connect to flat flexible cable. The connectors for the BEC production wires have a pitch of 1.27 mm (Mill-Max 399-XX-XXX-00-310000 series). These are standard single in-line package connectors. We have built our own cables for these connectors, using ultra-flexible stranded Cu wire (available from Cooner Wire).

We do not have a commercial pick and place machine, so the process of attaching the connectors uses improvised equipment. We attach the connectors after the vacuum system has been pinched off from the pumping station. We use a 30 AWG wire clamped in a translation stage to apply a small bead of conductive epoxy to each individual pad on the chip. We then use a pair of tweezer clamped to the same stage to lower the connectors into place. We visually monitor both of these processes through a stereo microscope. After the connectors are placed, we cure the epoxy using a heat lamp. We have achieved excellent results with this process; see Fig. 7.12. After the conductive epoxy is cured, we typically add a few drops of mechanical epoxy to increase durability. We use a very compliant epoxy (EPO-TEK OD1001) to avoid placing excess strain on the chip.

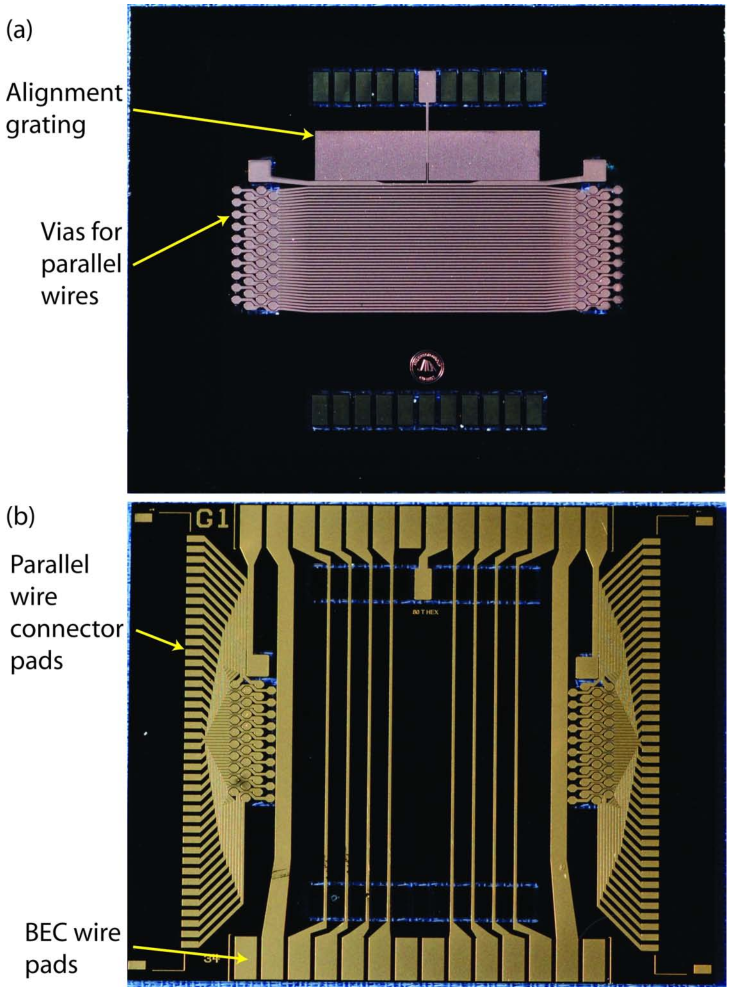

Figure 7.11: (Color). Photographs of both sides of the gyro chip: (a) vacuum side, (b) ambient side.

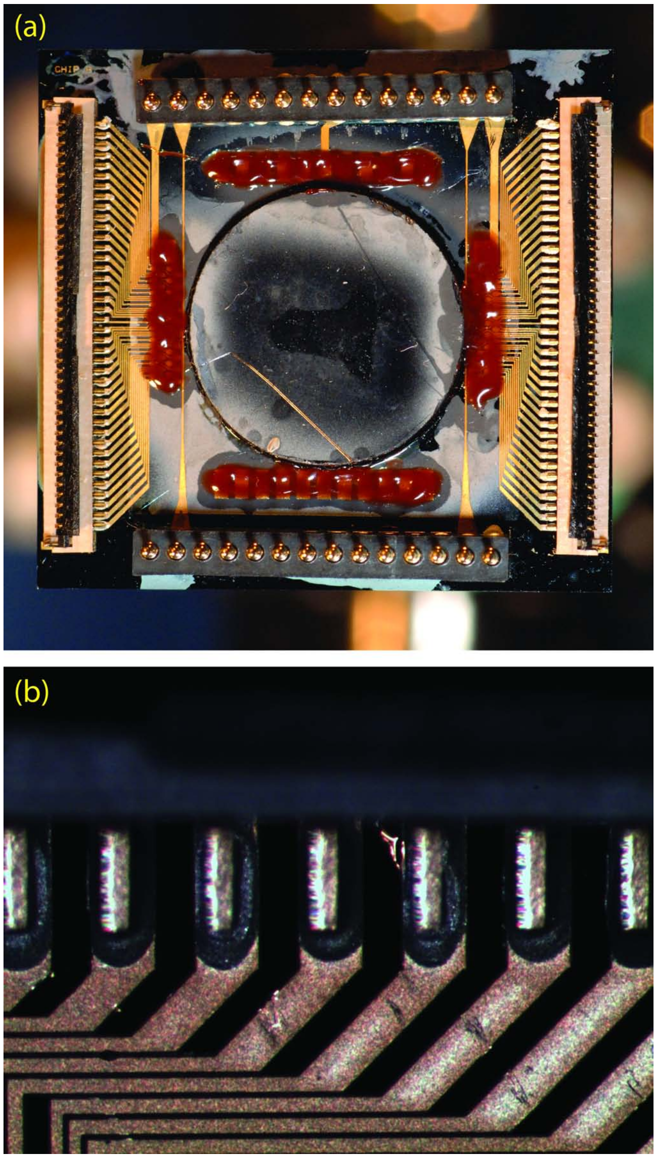

Figure 7.12: (Color). Views of gyro chip with electrical connectors. (a) View of all four connectors on chip. The red substance visible on the vias is Glyptal 1201B (Sec. 7.2). (b) Close-up of epoxy joints on high-pitch connector.

7.5.4 Loading the chip trap

The central section of the big Z coil is directly above the 100 μm wide chip wire, which generates the transverse confinement for the initial chip trap. As the big Z current is reduced during transport, the trapped atoms are brought to a position 1 mm directly under this wire. Following the procedure established in [18], we transfer the atoms from the big Z to the chip trap by simultaneously ramping the big Z current to zero and ramping the chip wire to 3 A over 100 ms. Axial confinement in the initial chip trap is provided by running current through the pair of H-wires on the back of the chip with the widest separation. The bias fields are adjusted during the transfer so that a trap with transverse frequency on the order of 1 kHz in the transverse axes is obtained approximately 100 μm below the chip. The T-wire is ramped on after loading to provide sufficient axial confinement for evaporative cooling.

Current for the chip wires is provided by JILA-designed current servos. These servos are powered by batteries to reduce current noise.

7.6 Imaging

All data collected about the state of system from the CMOT stage onwards is obtained by laser absorption imaging, using the $F = 2 \rightarrow F' = 3$ cycling transition. Two images are captured at the end of each experiment. The first is a data image, in which the atoms cast a shadow by scattering light out of the probe beam. The second is a normalization image, acquired as soon as the atoms have fallen out of the camera's field of view, in which the full power of the probe beam is captured. These two images are used to calculate the optical density (OD) of the cloud of atoms.

We use a compact digital camera (Basler scA1400-17fm), measuring 97 × 44 × 29 mm. It utilizes an interline charge-coupled device (CCD), in which every column of active pixels sits next to a column of inactive pixels. After an image is acquired, the accumulated charge is rapidly transferred from the active to the corresponding inactive pixels for read-out. A second image can begin acquisition nearly instantaneously while the first is being read [61]. The advantage of acquiring the data and normalization images in rapid succession is that the mechanical components of the apparatus have no time to shift in position between shots. There are therefore fewer of the artifacts in the OD image that are otherwise caused by vibration-induced shifts of diffraction and interference fringes in the probe laser beam [62]. Another feature of the CCD chip used by our camera is the inclusion of an electronic shutter, removing the need for a bulky, noisy mechanical shutter.

The lens system that we use for high-magnification imaging of microtrapped atoms is a machine vision microscope (custom, based on the Infinity InfiniTube Standard), AR coated for 780 nm. The lens has a magnification of 2.8 and working distance 145 mm. The camera's pixels are 6.45×6.45 μm squares, so each pixel will record a 2.3×2.3 μm area of the object plane. This is just larger than the lens's diffraction-limited 2 μm resolution. Decreasing that limit would require us to build an imaging system with a larger numerical aperture (NA), but the available NA for imaging is limited by the need to keep a clear path for the angled MOT beams (see Fig. 7.13). As can be seen in the figure, the lens tube is aligned vertically, poking through a hole in the upper baseplate. A mirror is used to steer the probe beam into the lens.

For imaging of atoms during earlier stages of the experiment, we remove the steering mirror and image horizontally with a lower-magnification lens system. The camera is mounted off of the breadboard in this type of imaging, so we are not able to image this way while the apparatus is rotating.

7.7 Control system

A computer system provides precisely timed control of the various elements of the apparatus. See Fig. 7.14 for a diagram of data flow in the control system. The system's core component is a field programmable gate array (FPGA). The FPGA (National Instruments PXI-7813R) is programmed to execute timed updates of its 160 digital outputs, using its own dedicated clock. The array of instructions for the FPGA resides in the memory of an embedded control computer

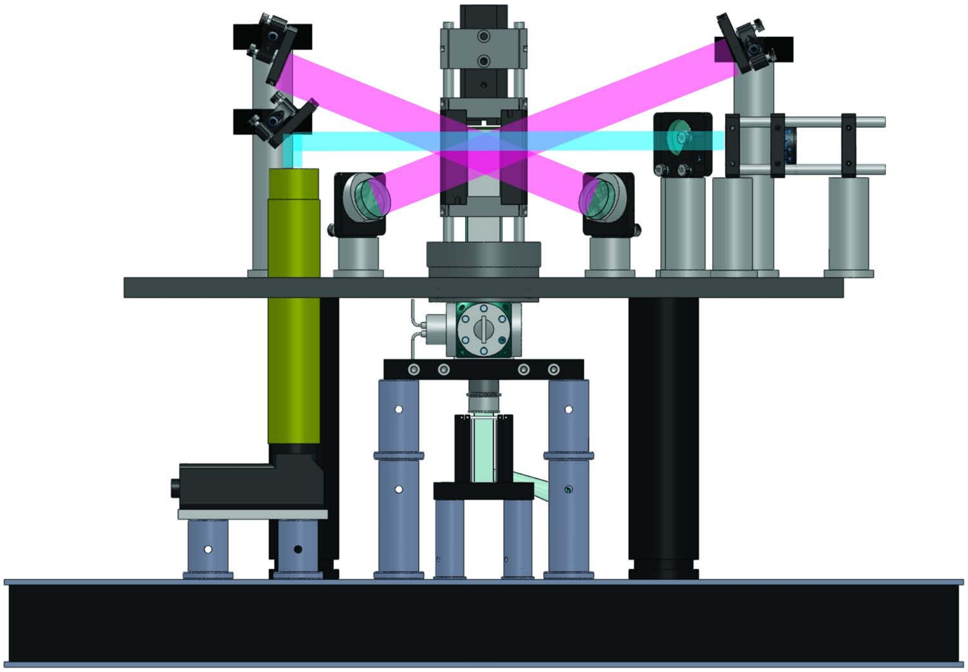

Figure 7.13: (Color). Side view of apparatus showing imaging system. Steering and retromirrors for angled 3D-MOT beams are also shown. This figure illustrates the difficulty of increasing the NA of the imaging system without clipping the angled beams. MOT light is shown in magenta, probe light in cyan, and the imaging lens in yellow.

running a real-time operating system. Both the FPGA and embedded computer are installed in (and communicate through the bus of) a PXI chassis.

The user sets the timing table before a run by interacting with a control interface, which is hosted on a computer running Microsoft Windows XP. The user's instructions are downloaded to the embedded computer via Ethernet, and then are executed independently of further interaction with the nondeterministic timing environment of Windows. The user interface, embedded controller, and FPGA all run software written in LabVIEW.

Many of the experiment's systems are controlled by analog voltages. These voltages are produced by a set of digital-to-analog converters (DACs, National Instruments 9263) that are controlled by the FPGA's digital outputs. The DAC modules each contain four output channels. Pre-packaged LabVIEW code modules provided by National Instruments handle the details of using a block of 40 of the FPGA digital outputs to control up to four DAC modules (16 analog outputs per block). The modules controlled by a block of FPGA outputs are housed outside of the PXI system in an expansion chassis. We have six DAC modules in the current configuration of the control system, occupying only two of the FPGA's 40 channel digital output blocks. The system is therefore easily expandable to include more analog outputs (and also analog inputs) should the need arise in the future.

Each DAC module has a floating, common signal ground that is isolated from that of the other modules. The isolated DAC grounds greatly ease the difficulty of eliminating ground loops from our electronics. We group together related analog-controlled devices on each module, and then ensure that the group's signal ground is tied to earth ground at exactly one location. As an example, consider the power supplies for the MOT and bias coils, which are controlled by a single module (DAC 1 in Fig. 7.14). The chassis of just one of these supplies is tied directly to earth ground, and the only connection between the common signal ground of all four supplies and earth is made there. We ensure that the chassis of the other three supplies are tied to earth only through the chassis of the primary supply. This is done by wiring the chassis together with heavy gauge Cu wire, and then installing electrical plug adapters to cut their independent

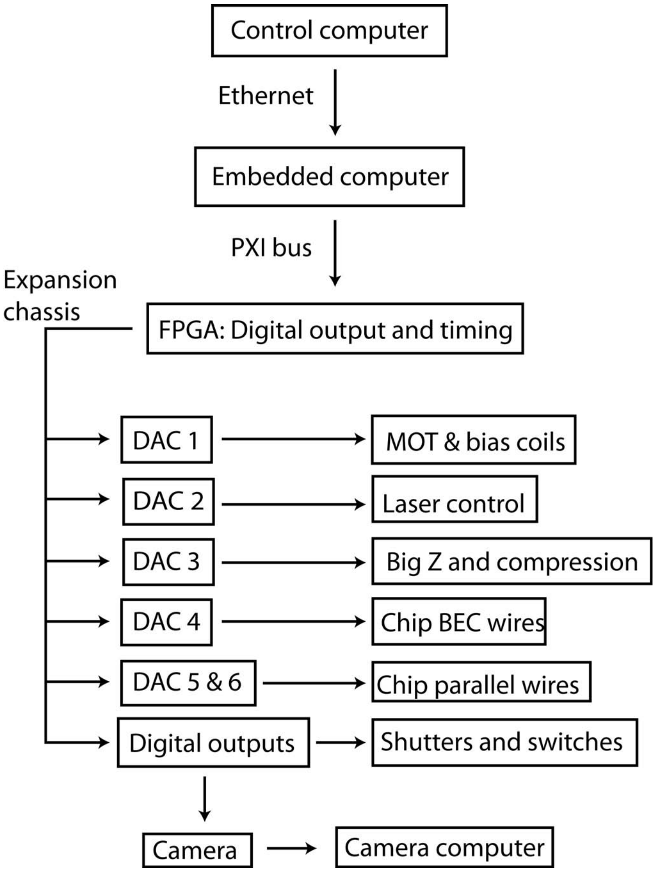

Figure 7.14: Diagram of control system. “Chip BEC wires” refers to the current supplies driving those chip wires needed for initial trapping and BEC production: the main, T, and H wires. “Chip parallel wires” refers to the supplies driving the array of parallel wires for translating waveguide interferometry.

connections to earth ground. Figure 7.15(a) shows a schematic of the wiring scheme. Careful control of grounding leads to significant decreases in electrical noise in our system. Figure 7.15(b) shows the results of a noise measurement comparing the case of proper grounding (black trace) to the case in which both chassis connect to earth independently (red trace). We show the voltage noise measured by an AC coupled dynamic signal analyzer across a 1 Ω test resistor driven with 1 A of current by the grounded supply. Similar single-reference grounding schemes are used for the instruments controlled by the other DAC modules.

The other task required of our control system is image acquisition. A digital control output is used to trigger image acquisition through the camera's external control input. The images are downloaded to a second Windows computer through a FireWire 800 interface. Software written in LabVIEW displays the images, carries out preliminary analysis, and optionally saves the images for further study. The use of a separate imaging computer is not necessary in our system, as the critical timing tasks are carried out by the FPGA. The control system interface and imaging acquisition tasks will likely be combined in a single computer in a future upgrade.

7.8 Current progress and future work

We have successfully loaded a 3D-MOT while slowly rotating the apparatus on the air bearing. We have also, in the stationary mode, carried BEC production as far as the transfer of atoms into the initial chip trap. Progress was delayed for a time by unexpected challenges in the fabrication of the high-density via pattern of the atom chip. A new fabrication process developed by our collaborators at Teledyne Scientific seems to have overcome these issues.

A vacuum system using the new chips has now been installed in the gyro apparatus. We should soon be loading the initial chip trap with atoms. Evaporative cooling to BEC should soon follow. BEC has been achieved in similar systems after a radio frequency (RF) evaporation cycle lasting only a few seconds. The RF radiation will be coupled to the atoms by a single loop coil fixed to the big Z assembly (see Fig. 7.10). Typical BECs are expected to contain on the

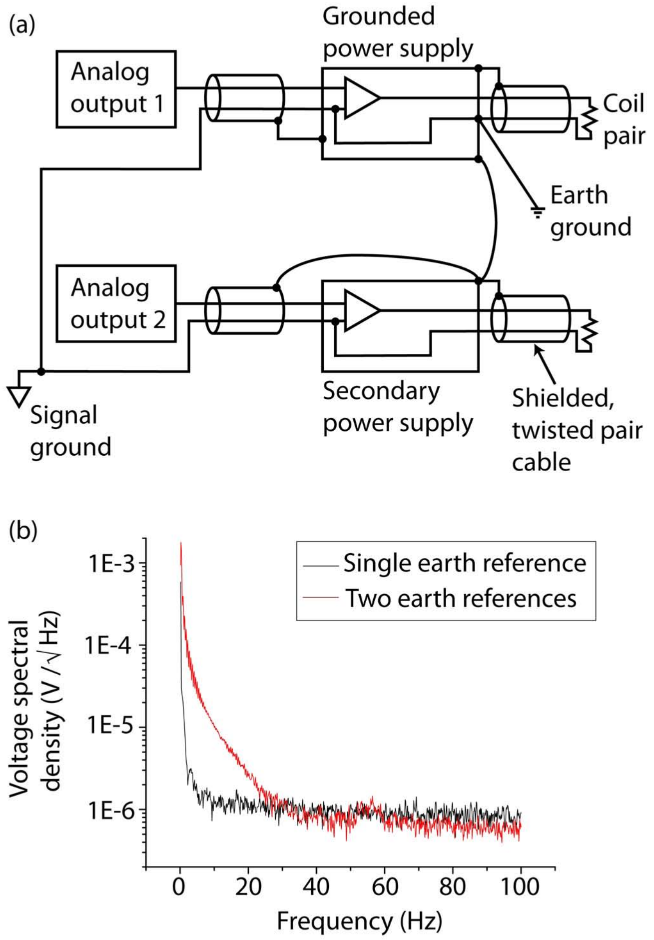

Figure 7.15: (Color). Grounding scheme for MOT and bias coil power supplies. (a) Schematic of ground connections. The chassis of only one power supply is tied directly to earth ground; the connection between signal and earth ground is made at that chassis. Other supplies are connected to earth ground via the grounded supply's chassis. (b) Measurement of noise spectrum of grounded supply when wired as shown in (a) (black trace), and when second power supply chassis is allowed to connect to earth ground independently (red trace).

order of 2×10^4 atoms [53]; total BEC production time will be on the order of 5–10 s.

After BEC is achieved, interferometry experiments will begin. We have already completed preliminary design work on the optical system that will be used to create the standing wave for beamsplitting. An array of parallel traces aligned perpendicular to the primary wires on the vacuum side of the chip provides a reflection grating that we will use to align the beam to the axis of the waveguide, regardless of the tilt angle induced by the axial confinement (see Fig. 7.11).

We have also built an 8-channel battery-driven current supply to provide the current we will run through the parallel "moving waveguide" wires. A custom-designed printed circuit board will be used to connect every eighth wire in series. Calculations show that a traveling wave of current amplitude < 0.5 A can create waveguides with the $\omega_\rho = 2\pi \times 80$ Hz transverse confinement that we modeled in Chap. 6. Axial confinement will be provided by a pair of H-wires attached to the big Z mount (approximate location indicated in Fig. 7.10). The spacing of these wires is set keep the anharmonicity parameter given in Eq. (2.27) small.

This dissertation has presented the initial steps leading from past work with BEC Michelson interferometry in a stationary waveguide towards the demonstration of a BEC Sagnac gyroscope based on a traveling waveguide. Much work remains to be done to complete the testing of the new apparatus and the proposed method for moving the guide. We should note that the small size of the BECs that will likely be available in our first experiments may cause shot noise to be a limiting performance factor (see Sec. 1.1.3). Fortunately, the flexibility of the apparatus will allow the easy replacement of the currently installed vacuum system with an updated design capable of improved performance. It is exciting to consider that if the proof-of-concept experiment proposed here is a success, then recent rapid progress towards the miniaturization of lasers, power supplies, and control systems [53] could soon lead to the construction of a field-deployable BEC gyroscope.

Bibliography

[1] D. H. Titterton and J. L. Weston, Strapdown Inertial Navigation Technology (Institution of Electrical Engineers, Stevenage UK, 2004).

[2] D. Budker, D. F. Kimball, and D. P. DeMille, Atomic Physics: An Exploration Through Problems and Solutions (Oxford University Press, Oxford, 2004).

[3] S. F. Jacobs and R. Zanoni, Am. J. Phys. **50**, 659 (1982).

[4] H. Lefèvre, The Fiber-Optic Gyroscopope (Artech House, Boston, 1993).

[5] G. A. Pavlath, Northrop Grumman, Fiber-optic gyros: The vision realized, Report No. 24235 (`http://www.es.northropgrumman.com/by_division/navigationsystems/whitepapers/assets/Fiber-Optic_Gyros.pdf`).

[6] Northrop Grumman, LN-251 Embedded INS/GPS System, Report No. 22940/02-06/2000/Crawford (`http://www.es.northropgrumman.com/solutions/ln251/assets/LN-251_Embedded_INS-GPS_System.pdf`).

[7] L-3 Space & Navigation, Strategic Grade Fiber Optic Gyro, `http://www.l-3com.com/spacenav/space_and_nav/space_products/pdfs/SellSheet_SG_FOG_Feb08.pdf`, March 2008.

[8] T. L. Gustavson, P. Bouyer, and M. A. Kasevich, Phys. Rev. Lett. **78**, 2046 (1997).

[9] T. L. Gustavson, A. Landragin, and M. A. Kasevich, Classical Quantum Gravity **17**, 2385 (2000).

[10] D. S. Durfee, Y. K. Shaham, and M. A. Kasevich, Phys. Rev. Lett. **97**, 240801 (2006).

[11] A. D. Cronin, J. Schmiedmayer, and D. E. Pritchard, Rev. Mod. Phys. **81**, 1051 (2009).

[12] J. Fortágh and C. Zimmermann, Rev. Mod. Phys. **79**, 235 (2007).

[13] J. Reichel, Appl. Phys. B: Lasers Opt. **74**, 469 (2002).

[14] M. Horikoshi, Ph.D. thesis, University of Electro-Communications, 2007.

[15] H. Ott, J. Fortágh, and C. Zimmermann, J. Phys. B **36**, 2817 (2003).

[16] P. D. D. Schwindt, Ph.D. thesis, University of Colorado, 2003.

[17] S. Groth, P. Krüger, S. Wildermuth, R. Folman, T. Fernholz, J. Schmiedmayer, D. Mahalu, and I. Bar-Joseph, Appl. Phys. Lett. **85**, 2980 (2004).

[18] M. B. Squires, Ph.D. thesis, University of Colorado, 2008.

[19] Y.-J. Wang, D. Z. Anderson, V. M. Bright, E. A. Cornell, Q. Diot, T. Kishimoto, M. Prentiss, R. A. Saravanan, S. R. Segal, and S. Wu, Phys. Rev. Lett. **94**, 090405 (2005).

[20] S. Wu, Y.-J. Wang, Q. Diot, and M. Prentiss, Phys. Rev. A **71**, 043602 (2005).

[21] K. J. Hughes, B. Deissler, J. H. T. Burke, and C. A. Sackett, Phys. Rev. A **76**, 035601 (2007).

[22] H. Müller, S. Chiow, and S. Chu, Phys. Rev. A **77**, 023609 (2008).

[23] H. Müller, S. Chiow, Q. Long, S. Herrmann, and S. Chu, Phys. Rev. Lett. **100**, 180405 (2008).

[24] Y.-J. Wang, Ph.D. thesis, University of Colorado, 2005.

[25] Q. Diot, Ph.D. thesis, University of Colorado, 2008.

[26] P. D. D. Schwindt, E. A. Cornell, T. Kishimoto, Y.-J. Wang, and D. Z. Anderson, Phys. Rev. A **72**, 023612 (2005).

[27] S. R. Segal, Q. Diot, E. A. Cornell, A. A. Zozulya, and D. Z. Anderson, Phys. Rev. A (to be published), eprint arXiv:0905.1979v2.

[28] H. J. Lewandowski, D. M. Harber, D. L. Whitaker, and E. A. Cornell, J. Low Temp. Phys. **132**, 309 (2003).

[29] K. I. Lee, J. A. Kim, H. R. Noh, and W. Jhe, Opt. Lett. **21**, 1177 (1996).

[30] W. Ketterle, D. S. Durfee, and D. M. Stamper-Kurn, in Bose-Einstein Condensation in Atomic Gases: Proceedings of the International School of Physics "Enrico Fermi", Varenna on Lake Como, Villa Monastero, 7–17 July 1998, edited by M. Inguscio, S. Stringari, and C. E. Wieman (IOS Press, Amsterdam, 1999), p. 67.

[31] M. S. Bartlett, J. R. Movellan, and T. J. Sejnowski, IEEE Trans. on Neural Networks **13**, 1450 (2002).

[32] K. J. Friston, C. D. Frith, P. F. Liddle, and R. S. J. Frackowiak, J. Cereb. Blood Flow Metab. **13**, 5 (1993).

[33] A. M. Aguilera, F. A. Ocana, and M. J. Valderrama, Appl. Stoch. Models Bus. Ind. **15**, 227 (1999).

[34] O. Lahav, A. Naim, L. Sodre, and M. C. Storrie-Lombardi, Mon. Not. R. Astron. Soc. **283**, 207 (1996).

[35] C. J. Pethick and H. Smith, Bose-Einstein Condensation in Dilute Gases (Cambridge, Cambridge, 2002).

[36] M. Horikoshi and K. Nakagawa, Phys. Rev. A **74**, 031602(R) (2006).

[37] D. C. Lay, Linear Algebra and its Applications (Addison-Wesley, Reading MA, 2000).

[38] I. T. Jolliffe, Principal Component Analysis (Springer-Verlag, New York, 2002).

[39] A. Hyvärinen, J. Karhunen, and E. Oja, Independent Component Analysis (John Wiley, New York, 2001).

[40] H. Gävert, J. Hurri, J. Särelä, and A. Hyvärinen, computer code FASTICA, Laboratory of Computer and Information Science, Helsinki University of Technology (2005).

[41] A. Papoulis, Probability, Random Variables, and Stochastic Processes (McGraw-Hill, New York, 1965).

[42] J. L. Devore, Probability and Statistics for Engineering and the Sciences (Brooks/Cole, Pacific Grove CA, 1991).

[43] D. B. Owen, Handbook of Statistical Tables (Addison-Wesley, Reading MA, 1962).

[44] W. H. Press, B. P. Flannery, S. A. Teukolsky, and W. T. Vetterling, Numerical Recipes in C: The Art of Scientific Computing (Cambridge University, Cambridge, 1988).

[45] E. Kreyszig, Advanced Engineering Mathematics (John Wiley & Sons, New York, 1999).

[46] J. Javanainen and M. Wilkens, Phys. Rev. Lett. **78**, 4675 (1997).

[47] A. Luis and L. L. Sánchez-Soto, Phys. Rev. A **48**, 4702 (1993).

[48] S. Wu, E. Su, and M. Prentiss, Phys. Rev. Lett. **99**, 173201 (2007).

[49] G. B. Arfken and H. J. Weber, Mathematical Methods for Physicists (Harcourt Academic, San Diego, 2001).

[50] L. D. Landau and E. M. Lifshitz, Mechanics (Pergamom, Oxford, 1969).

[51] Y. Castin and R. Dum, Phys. Rev. Lett. **77**, 5315 (1996).

[52] S. Du, Ph.D. thesis, University of Colorado, 2005.

[53] D. M. Farkas, K. M. Hudek, E. A. Salim, S. R. Segal, M. B. Squires, and D. Z. Anderson, Appl. Phys. Lett. **96**, 093102 (2010).

[54] S. B. Papp, Ph.D. thesis, University of Colorado, 2007.

[55] V. M. Bright, C. R. Stoldt, D. J. Monk, M. Chapman, and A. Salian, in Enabling Technology for MEMS and Nanodevices, edited by H. Baltes, O. Brand, G. K. Fedder, C. Hierold, J. G. Korvink, and O. Tabata (Wiley-VCH, Weinheim, Germany, 2004).

[56] G. Humpston and S. J. Baker, Gold Bull. (London, U.K.) **31**, 131 (1998).

[57] Vacseal high vacuum leak sealant, SPI Supplies website, `http://www.2spi.com/catalog/vac/vacleak.shtml`, accessed 15 March 2010.

[58] R. K. E. Weebe, in Conference on tube techniques (IEEE, New York, 1968), p. 113.

[59] J. Markus, Electronic Circuit Manual (McGraw-Hill, New York, 1971).

[60] P. T. Vianco, in ASM Handbook, vol. 6.

[61] Class for Physics of the Royal Swedish Academy of Sciences, Two Revolutionary Optical Technologies, `http://nobelprize.org/nobel_prizes/physics/laureates/2009/sciback_phy_09.pdf` (2009).

[62] W. Setiawan, B.S. thesis, Massachusetts Institute of Technology, 2007.

Appendix

Table of mathematical symbols used in text

Vectors are denoted by boldface type, while unit vectors have a hat placed atop the bold symbol. Magnitudes of vectors are denoted by the italic form of the symbol, except where noted. Dots indicate derivatives with respect to time. In some cases, a prime denotes a derivative with respect to a spatial coordinate.

α_n	Dimensionless wire width parameter
β	Second dimensionless wire width parameter [see Eq. (6.34)]
γ	Trap aspect ratio
γ_2	Normalized kurtosis excess
δ	Detuning from resonance
$\delta\lambda_i$	Small shift in dimensionless BEC size scaling parameter along axis i
$\Delta\phi$	Differential phase shift
$\Delta\phi_{\text{laser}}$	Phase shift induced by vibration
$\lvert\Delta\phi_{\check{p}}\rangle$	Eigenstate of phase-difference operator
$\delta_D(x)$	Dirac delta function
ΔP	Path length shift

Δp	Separation in momentum
ΔU	Perturbation to potential
Δx	Wire width
Δz	Separation between BECs along waveguide axis
δ(variable)	Uncertainty in (variable)
ϵ	$e^{-2\pi y_0/L}$, smallness parameter for perturbations
η	Amplitude of trap frequency modulation
$\Theta(x)$	Unit step function
θ	Tilt angle of waveguide with respect to main wire
κ	Amplitude of deviations from trap center during guide translation
λ	Wavelength
λ_{dB}	deBroglie wavelength
λ_i	Dimensionless BEC scaling parameter along axis i
μ_i	Chemical potential of BEC i
μ_{B}	Bohr magneton
μ_0	Magnetic constant
μ_4	Fourth statistical moment
ξ	Deviation in energy of two-BEC system from equilibrium
(ρ, ϕ, z)	Cylindrical coordinates
ρ_0	Harmonic oscillator length of radial waveguide

σ	Standard deviation
$\hat{\sigma}$	MLE of standard deviation of normally distributed noise
$\sigma_{\Delta\phi}$	Standard deviation of phase distribution
τ	$\omega_\rho t$, dimensionless time coordinate
τ_i	Duration of event i
ϕ_D	Normally distributed phase noise due to phase diffusion
ϕ_v	Initial phase of vibration
$\chi_{i,j}$	Unit-normalized wavefunction for i atoms in state 1 and j atoms in state 2
Ψ	Many-body wavefunction
ψ	Single-atom wavefunction
$\boldsymbol{\Omega}$	Angular velocity
ω	Angular frequency
$\bar{\omega}$	Geometric mean trapping frequency
Ω_E	Effective two-photon Rabi frequency
ω_i	Angular trap frequency along axis i
$\hbar\omega_{N_T/2}$	Energy of two BECs containing equal number of atoms
$\boldsymbol{\Omega}_\mathrm{R}$	Rabi vector (Bloch sphere representation)
Ω_R	Rabi frequency
ω_r	Recoil frequency
ω_v	Frequency of vibration

ω_1	Frequency fit parameter for simulated phase diffusion data
$\hat{\Omega}$	$2\omega_z$, frequency of transverse acceleration profile
$\tilde{\Omega}$	$N\tilde{\omega}/\omega_\rho$, Dimensionless perturbation frequency
$\tilde{\omega}$	$2\pi v_c/L$, perturbation driving frequency
$\mathbf{A}$	Area
A	Amplitude of interference signal in PC or IC representation
$\hat{A}$	MLE of amplitude of interference signal
a	Acceleration
a_c	Acceleration of waveguide center
A_i	Constants
$a_{\text{mode name}}$	Amplitude of named collective mode
a_s	Scattering length
a_1	Amplitude fit parameter for simulated phase diffusion data
$\bar{a}$	Geometric mean oscillator length
$\hat{a}$	Non-negative integer
$\mathbf{B}$	Magnetic induction (referred to as magnetic field)
b	Integer
$\mathbf{B}_{\text{c}}$	Magnetic field of crossing wire at waveguide height
b_i	Polynomial coefficient i
$\mathbf{B}_n$	Magnetic field of harmonic n

$\mathbf{B}_\mathrm{T}$	Field of T wire at waveguide height
B_w	Magnetic field amplitude of parallel wire array
$\mathbf{B}_0$	Bias magnetic field
C	Capacitance
c	Speed of light
C_i	State amplitude of momentum state i
c_i	Trap perturbation minimizing parameters
D	Sample covariance matrix of PC basis
d	Displacement of trapping wires away from chip surface
D_g	Diffraction grating period
$\mathbf{E}$	Electric field
E	Energy
$\mathbf{F}$	Total atomic angular momentum
f	Focal length
$f_L(\mathbf{z}, \boldsymbol{\theta}_p)$	Likelihood of parameters $\boldsymbol{\theta}_p$ for observation set $\mathbf{z}$
$f_x(x)$	Probability density of random variable x
g	Strength of interatomic contact interaction
$g(x)$	An integrable function of x
g_F	Landé g factor of total angular momentum
h	Planck constant

$h(x)$	An integrable function of x
$\mathbf{I}$	Electrical current
i	$\sqrt{-1}$ or an integer
I_{H}	Magnitude of current flowing through H wires
I_m	Magnitude of current flowing through wire m
$\mathbf{J}$	Current density
j	Integer
$\mathbf{K}$	Surface current density
$\mathbf{k}$	Wavevector of interfering wave
k	Wavenumber of interfering wave or an integer (distinguished by context)
K_a	Transverse acceleration amplitude
$K_n^{(c)}$	Fourier cosine coefficient n of K
$K_n^{(s)}$	Fourier sine coefficient n of K
$\mathbf{k}_0$	Wavevector of laser used in diffraction beamsplitter
L	Spatial period of traveling wave of current. In Ch. 7, inductance
$\mathbf{l}$	Displacement along curve of integration
L_{H}	Distance separating H wires
$\mathbf{M}$	Mean image of a data set
M	Mass
m	Integer

m_F	Quantum number of projection of total angular momentum along an axis
N	Number of wires per spatial period of traveling wave of current
n	Integer
$N_{\tau/2}$	Number of axial half-periods in interferometry experiment
N_I	Number of images in a data set
N_i	Number of particles observed by detector i or in interferometer arm i
N_p	Highest momentum order significantly populated by beamsplitter
N_T	Total number of interfering particles
$\mathbf{p}$	Translational momentum
$P(x)$	Probability of x
$p_c(r_d/s)$	Circular coverage function
$P^{(I)}$	Matrix of ICs
$P^{(P)}$	Matrix of PCs
$\mathbf{p}_0$	Initial momentum of separating BEC wavefunctions in experiment
$\hat{p}$	Number of pixels
q	Number of PCs retained
R	Rate of quantum phase diffusion
$\mathbf{r}$	Position with respect to origin
R_c	Fraction of atoms in zero momentum state after interferometry
$R_\mathrm{component}$	Resistance of component

r_d	Radius of integration of circular coverage function
R_i	Frequency-dependent parts of collective mode amplitude along axis i [see Eq. (6.49)]
$\mathbf{r}_s$	State vector (Bloch sphere representation)
S	Sample covariance matrix of pixel basis
s	Standard deviation of Gaussian in circular coverage function
T	Duration of interferometry experiment
t	Time
$\check{T}$	Time spent driving on resonance
$\hat{T}$	Period of transverse acceleration profile
U	Potential energy
$\mathbf{u}$	A basis vector of either the PC or IC basis
$\mathbf{u}^{(I)}$	A basis vector in the IC basis
$\mathbf{u}^{(P)}$	A basis vector in the PC basis
V	Visibility of interference pattern
$\mathbf{v}$	Velocity
v_c	Speed of transverse waveguide motion
$\mathbf{v}_0$	Initial velocity of separating BEC wavefunctions in interferometry experiment
w	Real number
$\mathbf{X}$	Vector representation of an image in pixel basis
$\hat{\mathbf{X}}$	Vector representation of an image in pixel basis, in mean-deviation form

$\hat{X}$	Matrix of images in pixel basis, in mean-deviation form
(x, y, z)	Cartesian coordinates (exceptions noted in following items)
(x', y', z')	Secondary Cartesian coordinate system
x	Normally distributed detection noise (in Sec. 4.5)
$x^{(m)}$	Position of BEC during mth half of transverse motion
$\hat{x}_m$	Position of left edge of wire m
$\mathbf{x}_0$	Position of waveguide minimum
$\bar{\mathbf{x}}$	Deviation from minimum of traveling waveguide
Y	Coefficient matrix of either the PC or IC basis
$Y^{(I)}$	Coefficient matrix of IC basis
$Y^{(P)}$	Coefficient matrix of PC basis
y	PC/IC coefficient related to interference signal (in Sec. 4.5)
y_0	Distance between microtrap minimum and generating wire
Z	Complex impedance
$\mathbf{z}$	Vector of observed interference signals, sum of signal and noise (in Sec. 4.5)
z_0	Classical turning point along waveguide axis